Osaka University Knowledge Archive

Title	NMR/NQR STUDIES OF MAGNETISM AND SUPERCONDUCTIVITY IN IRON PNICTIDES
Author(s)	木内, 宏彰
Citation	大阪大学, 2014, 博士論文
Version Type	VoR
URL	https://doi.org/10.18910/34505
rights	
Note	

Osaka University Knowledge Archive : OUKA

https://ir.library.osaka-u.ac.jp/

Osaka University

NMR / NQR STUDIES OF MAGNETISM AND SUPERCONDUCTIVITY IN IRON PNICTIDES

A dissertation submitted to
THE GRADUATE SCHOOL OF ENGINEERING SCIENCE
OSAKA UNIVERSITY
in partial fulfillment of the requirements for the degree of
DOCTOR OF PHILOSOPHY IN SCIENCE

BY

HIROAKI KINOUCHI

MARCH 2014

Abstract

A new family of superconductors containing tetrahedral iron-pnictide layers has attracted considerable interest because of their high transition temperature (T_c), some of which exceeds 50 K, and because of similarities with the high-T_c copper-oxide superconductors. Superconductivity emerges in close proximity to a magnetic ground state, just like the copper oxides. This suggests that magnetic interaction is relevant to superconductivity also in the iron pnictides. However, the microscopic origin is not yet fully understood despite of intensive investigations. One reason for this is that the iron pnictides are intrinsically multi-orbital, inducing significant variation in their physical properties, such as T_c, superconducting gap, and magnetic ordered moments. In order to get an insight into the multi-orbital nature of the iron pnictides, we have carried out systematic nuclear quadrupole resonance (NQR) and nuclear magnetic resonance (NMR) experiments on a new series of the iron-pnictide superconductors $(Ca_4Al_2O_6)Fe_2(As_{1-x}P_x)_2$ with an isovalent substitution of P for As. Such chemical substitution primarily tunes some structural parameters due to the different ionic size but does not add any carriers. This fact provides us with the good opportunity to study the correlations of superconductivity, magnetism and local structure around Fe atom.

In chapter 5, I focus on the As-end member compound $(Ca_4Al_2O_6)Fe_2As_2$, which shows superconductivity at $T_c \sim 27$ K. Measurement of nuclear-spin-relaxation rate $1/T_1$ reveals a significant development of two-dimensional antiferromagnetic spin fluctuations down to T_c, and points to unconventional nodeless superconductivity.

Moreover, I compare physical properties of the P-end member compound $(Ca_4Al_2O_6)Fe_2P_2$, which superconducts at $T_c \sim 17$ K, with those of $(Ca_4Al_2O_6)$ Fe_2As_2 in chapter 6. Our ^{31}P NMR data suggest that in the P-end member compound, nodal superconductivity is established under the background of the development of antiferromagnetic spin fluctuations. The expected superconducting gap structure makes a contrast to nodeless superconducting gap at the As-end member compound.

Chapter 7 deals with systematic ^{31}P- and ^{75}As- NMR studies on $(Ca_4Al_2O_6)$ $Fe_2(As_{1-x}P_x)_2$, which unravel that the nodeless superconducting state ($0 \leq x < 0.5$) evolves into an antiferromagnetic state ($0.5 \leq x \leq 0.95$), and eventually into the nodal superconducting state ($x \sim 1$) through an isovarent substitution of P

for As. To understand the evolution of different types of electronic ordering, the ground state of the iron pnictides with nominal Fe^{2+} state in the iron-pnictide layer are plotted in a two-dimensional plane of structural parameter. The map shows that the antiferromagnetic order taking place when the pnictogen height above the Fe plane h_{Pn} is in the range of 1.32Å$\leq h_{Pn} \leq$1.42Å, intervenes between nodeless and nodal superconductivity, and this event is universal irrespective of the materials. I believe that these findings bring a breakthrough to the solid understanding of iron-pnictide superconductors.

Contents

Abstract **ii**

1 Introduction **1**
1.1 Superconductivity 1
1.2 High-temperature (high-T_c) Cuprates 1
1.3 Iron Pnictides and Chalcogenides 3

2 Background **5**
2.1 Crystal Structure 5
2.2 Physical Properties 6
2.2.1 Phase Diagram 6
2.2.2 Magnetic Structure 9
2.2.3 Pairing Symmetry and Gap Structure 10
2.3 Band Structure and Fermi Surface 11
2.4 Factors Affecting T_c 12
2.5 Pairing Mechanism 13
2.6 Similarities and Differences with Cuprates 14

3 Experimental Methods and Principles **15**
3.1 Nuclear Magnetic Resonance (NMR) 15
3.1.1 Nuclear magnetic resonance phenomena 15
3.1.2 Nuclear spin Hamiltonian 15
3.1.3 Knight shift 17
3.1.4 Antiferromagnetic powder pattern in NMR under external fields 18
3.2 Nuclear Quadrupole Resonance (NQR) 19
3.3 Nuclear spin-lattice relaxation rate $1/T_1$ 20

4 Sample Description **24**

5 Experimental Results **30**
5.1 Unconventional Superconductivity and Spin Fluctuations in $(Ca_4Al_2O_6)Fe_2As_2$ 30
5.1.1 Motivation 30

5.1.2 Results and Discussion 30
5.2 Possible Nodal Gap Superconductivity in $(Ca_4Al_2O_6)Fe_2P_2$ 39
5.2.1 Results and Discussion 39
5.3 Phase Diagtram of $Ca_4Al_2O_6Fe_2(As_{1-x}P_x)_2$ 44
5.3.1 Motivation 44
5.3.2 Results and Discussion 44

6 Summary **52**

Bibliography **63**

List of Publications **65**

Acknowledgments **66**

List of Figures

1.1 T_c for various materials which showed the highest T_c at the times, including metals, alloys, copper-oxides, and pnictides. 2
1.2 Crystal structure of (a) $La_{2-x}Sr_xCuO_4$ and (b) $YBa_2C_3O_{6+x}$[8]. (c) AFM ordering in the CuO_2 plane. (d)Schematic phase diagram of the cuprates[9]. 3
1.3 Crystal structures of six majour families: iron pnictides (a) $(Ae_4M_2O_6)Fe_2Pn_2$, (b) RFePnO, (c) AeFe$_2Pn_2$, and (d) AFePn, and iron chalcogenides (e) $Ae_2Fe_4Ch_5$ and (f) FeCh. 4

2.1 (a) Tetrahedral layer of FeX (X=As, P, Te, Se, S). Inset shows top view of the layer. (b) Magnetic ordering and structural distortion in the FeX layer. Image is taken from a reference [19]. 5
2.2 Phase diagrams for 1111 family: (a) $LaFeAsO_{1-x}F_x$[23] and (b) Ce $FeAsO_{1-x}F_x$[24]. 7
2.3 Phase diagrams for 122 family: (a) electoron doped $Ba(Fe_{1-x}Co_x)_2As_2$[27], (b) hole doped $(Ba_{1-x}K_x)Fe_2As_2$[28] and (c) isovalent doped $BaFe_2(As_{1-x}P_x)_2$[29]. 8
2.4 Phase diagrams for (a) $Na(Fe_{1-x}Co_x)As$[30] and (b) $Fe(Te_{1-x}Se_x)$[40]. 9
2.5 (a) Three-dimenssional plot of the superconducting-gap size (Δ) of $(Ba_{0.6}K_{0.4})Fe_2As_2$ measured at 15 K by ARPES tequnics[52]. (b) The spin component of ^{57}Fe Knight Shift deduced by subtracting its orbital component, revealing a spin-singlet SC state.[19]. 10
2.6 The band structure of the five-band model of LaFeAsO. The Fermi Surface at $k_z = 0$ is shown on the middle[63]. 11
2.7 T_c vs (a) Pn-Fe-Pn bond angle[67] and (b) pnictogen height above the Fe plane[69] for various iron-pnictide superconductors. 12
2.8 The fully gapped (a) $s\pm$ wave and (b) $s++$ wave gap are schematically shown. The solid red (blue) curves represent positive (negative) sign of the gap. 13

3.1 Energy diagram of the nuclear spin system with $I = 3/2$ at the external field. The degeneracy of the nuclear spin levels is solved by the Zeeman interaction $\mathcal{H}_{\text{Zeeman}}$. 16

3.2 Energy diagrams of nuclear spin system with $I = 3/2$. (a) The degeneracy of the nuclear spin levels is solved by the electric quadrupole interaction $\mathcal{H}_{\mathrm{Q}}$ at zero field. Here, $h\nu_{\mathrm{Q}} = 3e^2qQ/2I(2I-1)$. (b) $\mathcal{H}_{\mathrm{Zeeman}}$ dominated spin levels are modified by $\mathcal{H}_{\mathrm{Q}}$. Δ represents $h\nu_{\mathrm{Q}}\left(3\cos^2\theta - 1\right)/4$ where θ is the angle between the principle axis of EFG and external field. 17
3.3 (a) Schematic image of distribution of nuclei. θ is the angle between the direction of the external magnetic field $\boldsymbol{H}$ and that of the internal magnetic field $\boldsymbol{H}_{\mathrm{int}}$. (b) The simulated NMR linehape in normal (black) and AFM state (blue) for the powder sample. . 19
3.4 SC gap functions $\Delta(\phi, \theta)$ in k-space for (a) isotropic full gap , (b) line-node gap, and (c) point-node gap model. Color indicates sign of $\Delta(\phi, \theta)$ (red: + and blue: −). 21
3.5 Energy dependences of DOS for quasiparticles in the SC state $N_{\mathrm{s}}(E)$ which is normalized by the DOS at the Fermi level in the normal state N_0 for various SC models. $\Delta(T)$ represents $\Delta_0 \tanh\{1.82[1.018(T_{\mathrm{c}}/T-1)]^{0.51}\}$.[82, 83] 23
3.6 T dependences of $1/T_1$ normalized by that at T_{c} for various SC models. The peak just below T_{c} for isotropic full-gap model is called the Hebel-Slichter coherence peak[84]. 23

4.1 (a) Crystal structure of $(Ca_4Al_2O_6)Fe_2(As_{1-x}P_x)_2$. (b) a-axis and (c) c-axis (top) views of FePn layer. Structural parameters of the nearest-neighbour Fe-Fe distance $a_{\mathrm{Fe-Fe}}$, the pnictogen height measured from the Fe plane h_{Pn}, and the Pn-Fe-Pn bond angle are displayed. 24
4.2 Powder XRD patterns of $(Ca_4Al_2O_6)Fe_2(As_{1-x}P_x)_2$ with (a)x=0.5 and (b)x=0.75 observed at 297K. 27
4.3 (a)x dependence of a-axis and c-axis length in $(Ca_4Al_2O_6)Fe_2$ $(As_{1-x}P_x)_2$. (b) Plots of pnictogen height (h_{Pn}) from the Fe plane versus x. The h_{Pn} are determined from powder x-ray(circles) and neutron(squares) diffraction measurements at room temperature. 28
4.4 (a) Temperature dependence of the magnetic susceptibility of $(Ca_4Al_2O_6)Fe_2(As_{1-x}P_x)_2$. Black arrows indicat the onset of superconducting transitions. (b) Temperature dependence of the resistivity of $(Ca_4Al_2O_6)$ $Fe_2(As_{1-x}P_x)_2$. Resistivity anomalies (kink) are indicated by black arrows. 29

5.1 ^{75}As-NQR spectra of CaAl42622 (As). The inset shows T dependence of $^{75}\nu_{\mathrm{Q}}$ of CaAl42622 (As), indicating that neither structural phase transition nor no magnetic order takes place in CaAl42622 (As). 31
5.2 Recovery curves of ^{75}As nuclear magnetization $m(t)$ at (a) 50 K and (b) 20 K. (c) T dependence of $1/T_1T$ for CaAl42622(As). The solid curve is a simulation fitted to a relation $1/T_1T \sim a/(T+\theta)+b$ with parameters $a = 37$, $\theta = -20$ K, and $b = 0.023$. 32

5.3 (a) Plots of ^{75}As-NQR $T_1(T_c)/T_1$ normalized at T_c against T/T_c for CaAl42622(As), along with the results of BaK122(OPT) with T_c=38 K[47], La1111(OPT) with T_c=28 K [90], and La1111(HOVD) with T_c=5 K[102]. Note that T dependences of T_{1S} and T_{1L} normalized at T_c for CaAl42622(As) are almost the same below T_c. The solid curves are simulations in terms of the $s_\pm$-wave model with multiple SC gaps (see text). (b) T dependence of ^{75}As-$(1/T_1T)$s normalized at T=250 K. 34
5.4 (a) Plots of ^{75}As-NQR $T_1(T_c)/T_1$ normalized at T_c against T/T_c for CaAl42622(As) and BaK122(OPT) with T_c=38 K[47]. The curves are simulations in terms of the $s_\pm$-wave model with two isotropic gaps with various values of $r_S \equiv N_s^S/(N_s^L + N_s^S)$. Here N_L and N_S represent the respective DOSs with large and small SC gaps. The experimental result for CaAl42622(As) was reproduced with r_S ~0.1, which is smaller than r_S ~0.3 for BaK122(OPT) [47]. (b) Similar plots for CaAl42622(As), La1111(OPT) with T_c=28 K[90] and La1111(HOVD) with T_c=5 K[102]. The experiment for CaAl42622(As) can be also reproduced by assuming a *negative value* of $\alpha_c \sim -0.86$, which contrasts with $\alpha_c \sim 0.33$ in La1111(HOVD) and $\alpha_c \sim 0$ in La1111(OPT). 36
5.5 The energy dependences of the density of states used above simulations. 37
5.6 T dependence of ^{31}P NMR spectrum for CaAl42622(P). Knight shift decreases below T_c(= 17 K). 40
5.7 T dependence of the ^{31}P-NMR- $1/T_1T$ and Knight shift K for CaAl42622(P). 41
5.8 (b) Plots of ^{31}NMR - $T_1(T_c)/T_1$ and (c) $(T_1T)^{-1}/(T_1T)^{-1}_{T_c}$ versus T/T_c in the SC state at x=1 along with that at x=0 [15]. The T-linear dependence in $1/T_1$ well below T_c at x=1 indicates the presence of the residual DOS at E_F in association with the nodal SC in contrast with the nodeless SC at x= 0 [15]. 42
5.9 (a) T dependence of ^{31}P $(T_1(T_c)/T_1)$ normalized T_c for $Ca_4Al_2O_6Fe_2P_2$, along with the results reported for $Ca_4Al_2O_6Fe_2As_2$. The multiple fully gapped $s_\pm$-wave model allows us to deduced the energy dependences of the density of states (c) through the fitting of the experimental $1/T_1$. (b) T dependence of $(T_1T)^{-1}$ normalized at $T \sim 250K$ for $Ca_4Al_2O_6Fe_2P_2$ and $Ca_4Al_2O_6Fe_2As_2$. 43
5.10 T dependence of (a) ^{31}P-NMR and (b) ^{75}As-NMR spectrum at x=0.75, pointing to the onset of AFM order below 60 K. The red solid line in (b) shows a successful simulation of the ^{75}As NMR powder-type spectrum. 45
5.11 x dependence of ^{31}P-NMR spectrum at 10 K along with a simulation. 46

5.12 x dependence of respective internal fields $^{31}H_{\rm int}$ and $^{75}H_{\rm int}$ at ^{31}P and ^{75}As. 46
5.13 T dependence of ^{31}P-NMR $^{31}(1/T_1T)$ in 0.2≤ x ≤1 along with ^{75}As-NQR $^{75}(1/T_1T)$ at x=0 at the normal state. Note that the $^{31}(1/T_1T)$s for $0.5 \leq x \leq 0.95$ diverge toward T_N, below which the ^{31}P-NMR spectrum exhibits a rectangular-like shape in association with the onset of an AFM order (see Fig. 1(b)). 47
5.14 (a) Phase diagram against x in $(Ca_4Al_2O_6)Fe_2(As_{1-x}P_x)_2$. The commensurate AFM order occurs in 0.5≤ $x \leq 0.95$, which intervenes between the nodeless SC in 0≤ $x \leq 0.4$ and the nodal SC at x=1. Each empty symbol near the phase boundary between the nodeless SC phase and the AFM ordered phase means that each sample contains a tiny fraction of minority domain exhibiting either AFM order or nodeless SC due to a possible spatial distribution of As/P content. 49
5.15 Map of the AFM ordered phase (filled symbols) and the SC phase (empty symbols) for $(Ca_4Al_2O_6)Fe_2(As_{1-x}P_x)_2$ plotted in the two-dimensional plane of structural parameters of the Fe-Fe distance $a_{\rm Fe-Fe}$ and h_{Pn}. Here, the emergent phases for various Fe-based compounds with the Fe^{2+} state in $(FePn)^-$ layer through the isovalent substitution at pnictogen (Pn) sites are presented with respect to Fe(Se,Te)[73, 131], LiFe(As,P)[123, 109], $BaFe_2(As,P)_2$[124, 114, 125, 126, 127], LaFe(Sb,As,P)O[20, 130, 108, 107], NdFeAsO[112], and $(Sr_4M_2O_6)Fe_2(As,P)_2$ (M=$Mg_{0.5}Ti_{0.5}$[115, 116], Sc[117, 110]). The symbol (+) denotes the compounds which are not superconductive. The AFM order taking place universally in the range of 1.32 Å≤ $h_{Pn} \leq$ 1.42Å intervenes between the nodeless SC in h_{Pn} > 1.42Å and the nodal SC in h_{Pn} < 1.32Å. Dotted line is a linear relation of h_{Pn} versus $a_{\rm Fe-Fe}$ at each value of α. 50

6.1 Summary of NMR / NQR studies on an isovalent system $(Ca_4Al_2O_6)Fe_2(As_{1-x}P_x)_2$. 53

Chapter 1

Introduction

Some historical events concerning superconductivity are recalled, and some key properties and theories of superconductivity are briefly described in this chapter.

1.1 Superconductivity

Superconductivity is a phenomenon in which the electrical resistance of a substance suddenly drops to zero at a particular temperature (T_c). Since the first observation in mercury by Heike Kamerlingh Onnes in 1911[1], hundreds of superconducting materials have been discovered by the continuous efforts of many physicists and material scientists as shown in Fig. 1.1. The microscopic description of superconductivity was produced by John Bardeen, Leon Neil Cooper, and John Robert Schrieffer (BCS) in 1957[2]. A key conceptual element in the BCS theory is the formation of electron pairs (known as Cooper pairs) through the interaction with lattice vibration (phonon). It is generally agreeable that superconductivity in metals and intermetallic compounds can be explained by the BCS theory. Such superconductivity is known to be incompatible with magnetism. For example, Alexey A. Abrikosov and Lev P. Gor′kov showed that magnetic impurities disrupt superconductivity[3].

1.2 High-temperature (high-T_c) Cuprates

In 1986 Johannes Georg Bednorz and Karl Alexander Müller reported a discovery of superconductivity in Ba-La-Cu-O ceramics with T_c higher than 30K[4]. The following year, the liquid nitrogen temperature (77 K) barrier was broken with the discovery of a related compound $YBa_2Cu_3O_{7-x}$, which is superconducting at ~90K[5]. Soon after that, the T_c of copper-oxide superconductors (so-called "cuprates") reached 134K at ambient pressure[6] and ~ 150K under high pressure[7], as shown in Fig. 1.1. These discoveries surprised a lot of

physicists who had believed that the maximum T_c would be about 30K, and opened a new field of material science.

All high-T_c cuprate superconductors share the common structural feature, containing the cupper-oxide (CuO_2) plane separated by "block layers", as shown in Fig. 1.2 (a) and (b). The block layers play a significant role as a charge reservoir, and the electric conduction occurs in the CuO_2 plane. Figure 1.2 (d) shows a schematic phase diagram of high-T_c cuprates. The undoped parent compounds are antiferromagnetic Mott insulators where a single electron is localized on the copper site due to the strong on-site Coulomb repulsion. Spins of nearest neighbours are aligned antiparallel to each other. High-T_c superconductivity emerges after introducing mobile holes or electrons into the CuO_2 plane which suppress the static antiferromagnetic order. This implies that there is an intimate relationship between superconductivity and magnetism. The magnetic spin-spin interaction between electrons are often thought to be important for the formation of Cooper pairs, although a consensus on the mechanism causing the high T_c in these materials has not been reached yet.

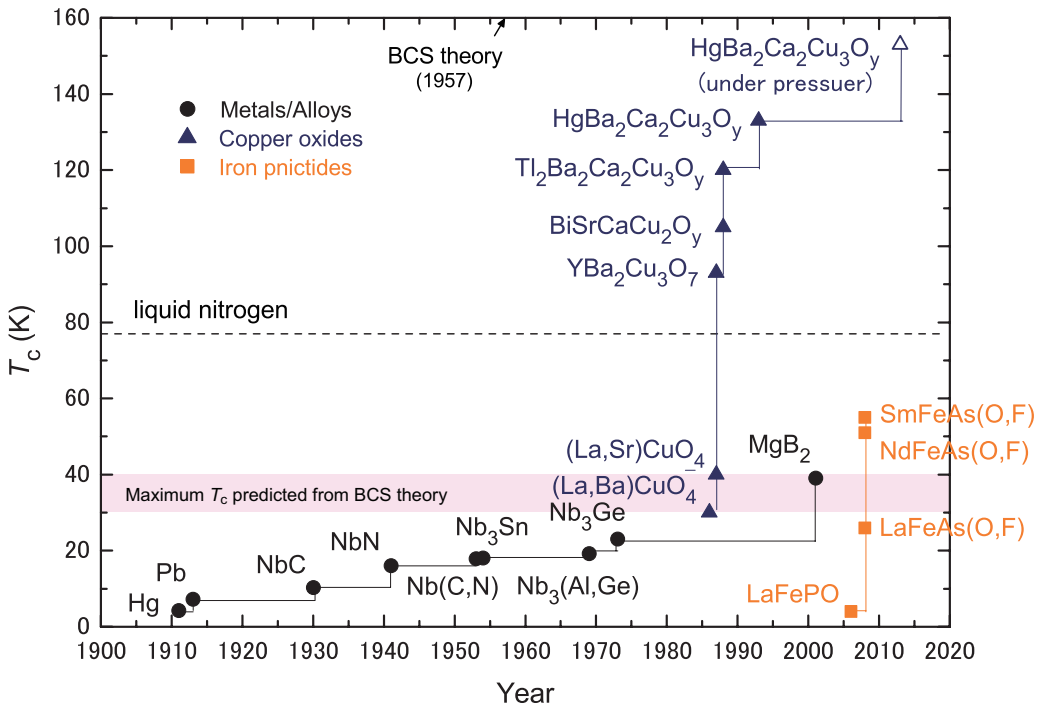

Figure 1.1: T_c for various materials which showed the highest T_c at the times, including metals, alloys, copper-oxides, and pnictides.

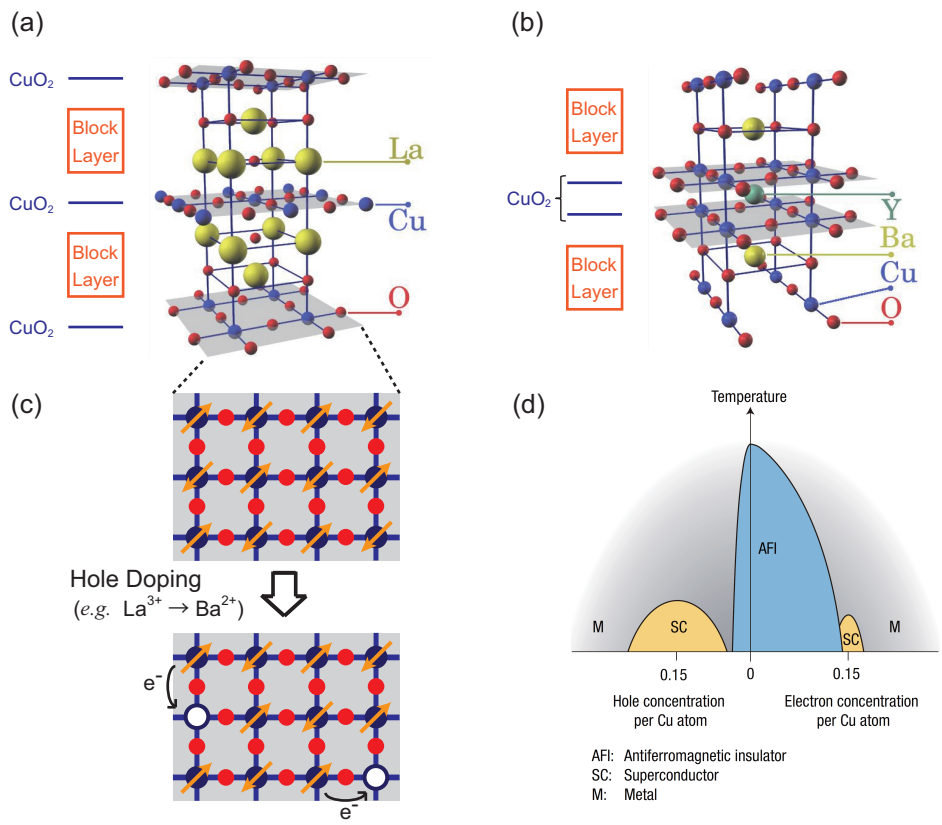

Figure 1.2: Crystal stracture of (a) $La_{2-x}Sr_xCuO_4$ and (b) $YBa_2C_3O_{6+x}$[8]. (c) AFM ordering in the CuO_2 plane. (d)Schematic phase diagram of the cuprates[9].

1.3 Iron Pnictides and Chalcogenides

The newly discovered iron (Fe)-based superconductors undermine the uniqueness of the cuprates and have prompted the community to rethink what is important and what is not for the appearance of high-T_c superconductivity.

The first Fe-pnictide superconductor LaFePO was discovered by Hosono's group at the Tokyo Institue of Technology in 2006[10]. The T_c is only $\sim$ 4K. A breakthrough came with the fluorine (F)-doped LaFeAsO that shows $T_c \sim$ 26K[11] which rise to $\sim$ 43K under pressure[12]. Reports on even higher T_c's of up to $\sim$ 55K, achieved by replacing lanthanum by rare earth ions with smaller ionic radii, followed quickly[13, 14]. This temperature exceeds the T_c of MgB_2 (39K) and is next to the cuprates. Meanwhile, a large number of layered compounds containing the antifluorite-like Fe*Pn* (*Pn*=pnictogen) or Fe*Ch* (*Ch*=chalcogen) in each structure have been proved to become superconducting. They are classified into four groups of iron pnictides and two groups of iron chalcogenides according to their chemical formula, as shown in Fig. 1.3. We

have focused on a new series of iron pnictides, which contain perovskite-type thick block layer. These compouds give us a good opportunity to investigate the difference between the iron pnictides and the cuprates due to similar two-dimentional structure.

In this thesis, I present systematic nuclear quadrupole resonance (NQR) and nuclear magnetic resonance (NMR) experiments, which demonstrate that an Fe-based new superconductor ($Ca_4Al_2O_6$) $Fe_2(As_{1-x}P_x)_2$ possesses a peculiar electronic phase diagram. We will also discuss the ground state of undoped iron pnictides with Fe^{2+} oxidation state in $(FePn)^-$ layer from a structural point of view. The results presented in this thesis have been published in several references[15, 16]. Additional related measurements performed by collaborators on crystal grown as part of this thesis have also been published[17, 18]

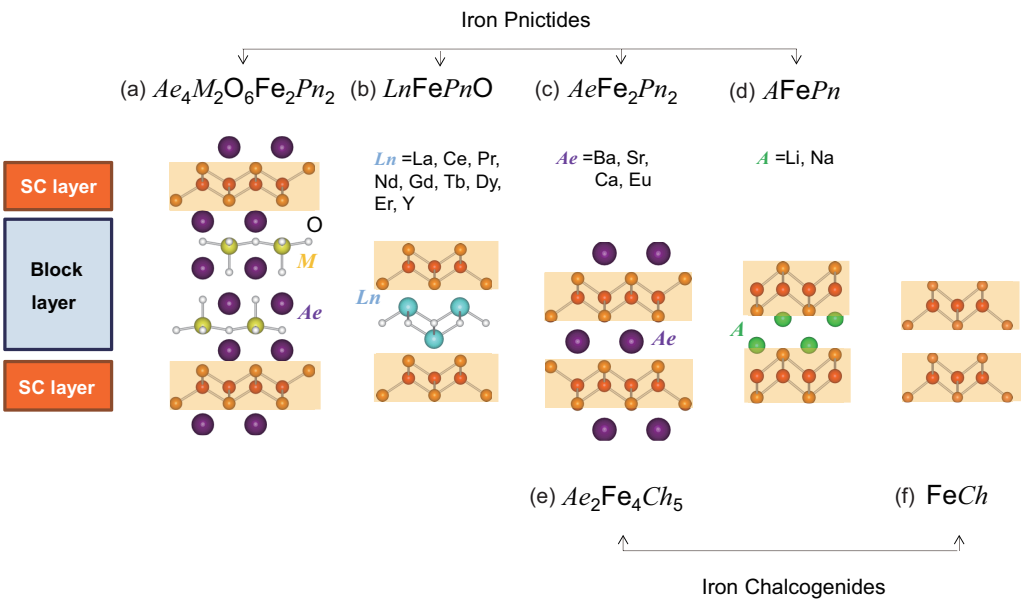

Figure 1.3: Crystal structures of six majour families: iron pnictides (a) $(Ae_4M_2O_6)Fe_2Pn_2$, (b) $RFePnO$, (c) $AeFe_2Pn_2$, and (d) $AFePn$, and iron chalcogenides (e) $Ae_2Fe_4Ch_5$ and (f) $FeCh$.

Chapter 2

Background

I introduce the current research situation of the iron-based superconductors in this chapter.

2.1 Crystal Structure

All Fe-based superconductors have a common structural feature consisting of a tetrahedral Fe*Pn* (*Pn*=As, P) or Fe*Ch* (*Ch*=Te, Se, S) layer in which Fe atoms form a square lattice perpendicular with *Pn* or *Ch* anions residing alternatively above and below the plane as shown in Fig. 2.1. These tetrahedral layers are separated by "block layer" such as rare-earth atoms (*R*) and oxygen, alkaline-earth atoms (*Ae*), and alkali atoms (*A*). The interlayer distance between the Fe planes enlarges in the order of FeSe, *A*FeAs, $AeFe_2As_2$, $Ae_2Fe_4Se_5$, *R*FeAsO, $(Ae_4M_2O_6)Fe_2As_2$.

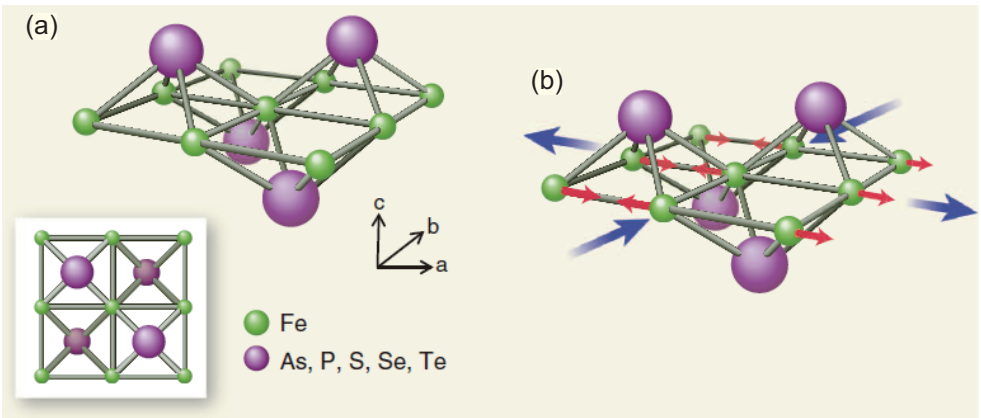

Figure 2.1: (a) Tetrahedral layer of Fe*X* (*X*=As, P, Te, Se, S). Inset shows top view of the layer. (b) Magnetic ordering and structural distortion in the Fe*X* layer. Image is taken from a reference [19].

2.2 Physical Properties

2.2.1 Phase Diagram

Figure 2.2-2.4 summarizes several available phase diagrams reported in *R*Fe *Pn*O, *Ae*Fe_2*Pn*$_2$, *A*Fe*Pn*, and Fe*Ch*.

- *R*Fe*Pn*O (abbreviated as 1111 for its 1:1:1:1 ratio of the four elements)
  The stoichiometric parent arsenides undergo a tetragonal to orthorhombic (T-O) structural transition at T_S and then form a stripe-type AFM ordering at a slightly lower temperature T_N, 10-20K below[20, 21, 22]. Chemical substitutions decrease both T_S and T_N in a similar fasion, and induce superconductivity where the static AFM order is destroyed. On the other hand, a phosphide LaFePO exhibits superconductivity without any carrier doping[10].

- *Ae*Fe_2*Pn*$_2$ (122)
  In contrast with the "1111" family, the AFM transition is coincident with the T-O structural distortion[25, 26]. The AFM phase overlap with a domelike SC phase and the maximum T_c is realized at the phase boundary.

- *A*Fe*Pn* (111)
  For NaFeAs series, the parent compound lies just within a SC dome that can be traverced by the addition of 0.1 electrons per Fe atom, and shows coexistence of antiferromagnetism and superconductivity over a region less than 0.025 electrons per Fe wide. In addition, A T-O structural transition precedes the AFM ordering like the "1111" family[30].
  On the other hand, LiFeAs[31, 32] and LiFeP[33, 34] were shown to be bulk superconductors in its undoped, stoichiometric form.

- Fe*Ch* (11)
  Like the "122" series, the structural and AFM transitions occur simultaneously in FeTe [35]. When the long-range static AFM order is suppressed by isoelectronic substitution of Te with Se, superconductivity appears and the incommensurate AFM order with the in-plane propagation wave-vector ($\delta\pi$, $\delta\pi$) direction (along the diagonal direction of the Fe-Fe square) becomes short-range spin fluctuations[36].
  FeSe undergoes the T-O structural transition near 70K[37], and superconduct at $T_c \sim 8$K[38], which increases to 27 K at 1.48 GPa[39].

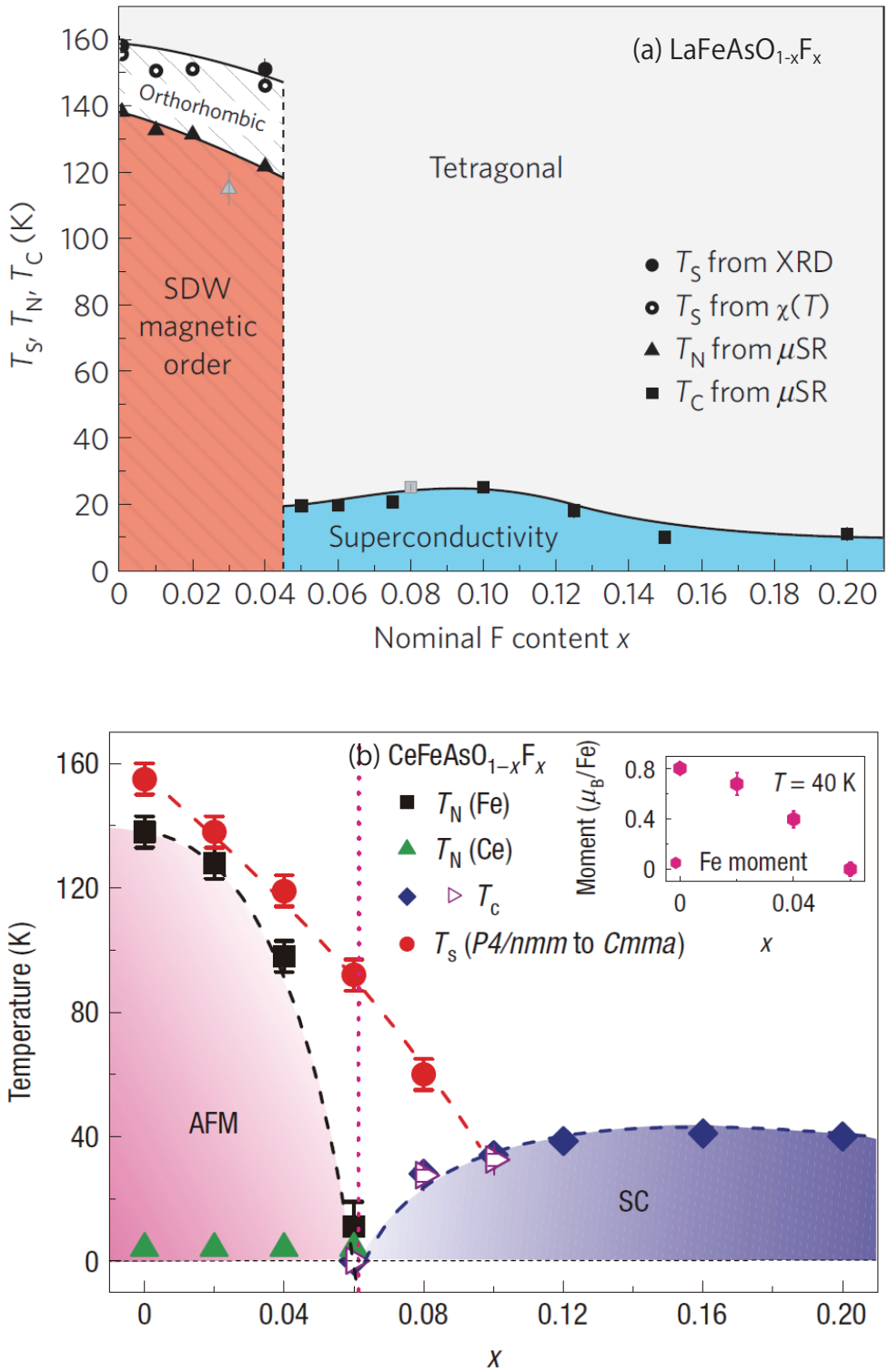

Figure 2.2: Phase diagrams for 1111 family: (a) $LaFeAsO_{1-x}F_x$[23] and (b) Ce $FeAsO_{1-x}F_x$[24].

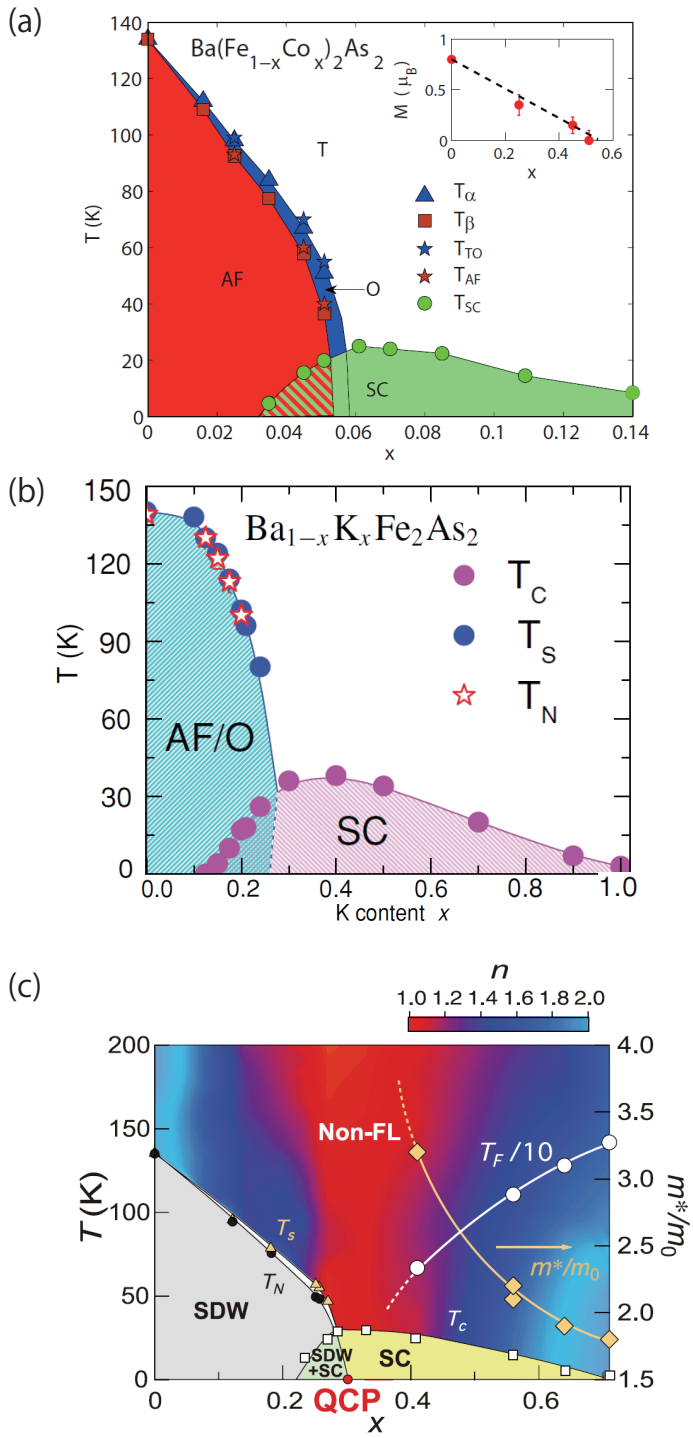

Figure 2.3: Phase diagrams for 122 family: (a) electoron doped $Ba(Fe_{1-x}Co_x)_2As_2$[27], (b) hole doped $(Ba_{1-x}K_x)Fe_2As_2$[28] and (c) isovalent doped $BaFe_2(As_{1-x}P_x)_2$[29].

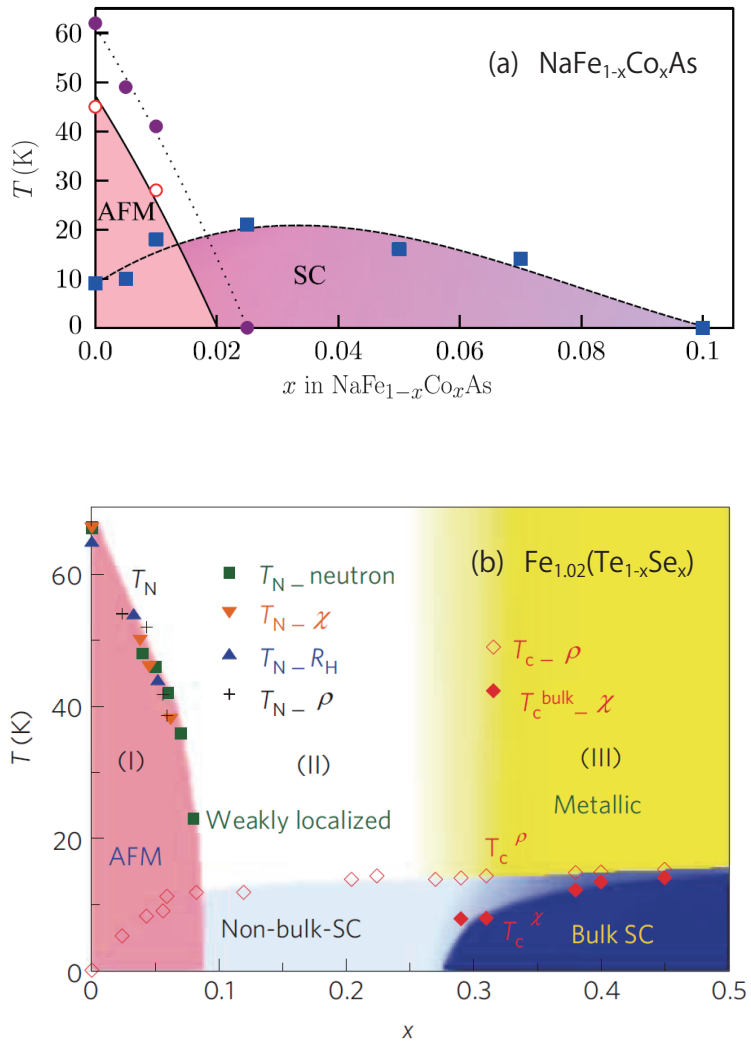

Figure 2.4: Phase diagrams for (a) $Na(Fe_{1-x}Co_x)As$[30] and (b) $Fe(Te_{1-x}Se_x)$[40].

2.2.2 Magnetic Structure

As mentioned above, superconductivity in most of the Fe-based superrconductors emerges in close proximity to a magnetic ground state. Investigation of the magnetism is thus a first step toward understanding the mechanism that causes high-T_c superconductivity. So far, neutron scattering experiments have resolved the magnetic structure in some parent compounds of the Fe-based superconductors. As illustrated in Fig. 2.1 (b), most parent compounds, except for FeTe[36], share a magnetic order which is antiferromagnetic in one direction and ferromagnetic in the other within *ab* plane. This magnetic structure has been explained from both itinerant- [41, 42] and localized- [43] electron point of view.

2.2.3 Pairing Symmetry and Gap Structure

Knight shift is proportional to spin susceptibility and thus provides direct measure of the symmetry of the Cooper pair. Knight-shift measurements revealed that the Cooper pairs are in the spin-singlet state, implying an even order paramater (OP) symmetry (that is, *s*-wave, *d*-wave symmetry and so on) [44, 45, 46, 47, 48, 49]. So far, this experiment has been done on main members of the four families, including samples of the 1111- [44, 45], 122- [46, 47], 111- [48], and 11-systems[49], and therefore, it is reasonable to assume that superconductivity in the Fe-based compounds is universally spin singlet. However, it is much complex to determine the nature of the OP in momentum space, particularly the presence or absence of nodes. For instance, NMR spin-lattice relaxation rate ($1/T_1$) measurements show no Hebel-Slichter (HS) coherence peak just below T_c and power-low decay far below T_c, excluding the possibility of conventional *s*-wave state[44, 45, 46, 47, 49]. On the other hand, it has been established from penetration depth measurement[50, 51] and angle-resolved photoemission spectroscopy (ARPES)[52, 53, 54, 55, 56, 58, 57, 59, 60] that the *s*-wave SC state is realized in usual Fe-based superconductors. These conflicting results have been explained by the theoretically proposed "$s_{\pm}$-wave" state (please see section 2.5).

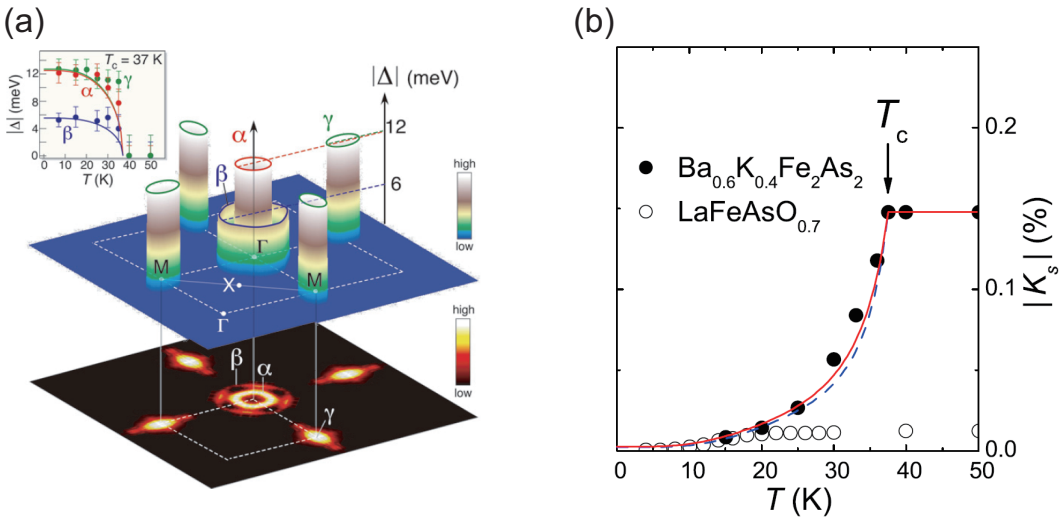

Figure 2.5: (a) Three-dimenssional plot of the superconducting-gap size (Δ) of $(Ba_{0.6}K_{0.4})Fe_2As_2$ measured at 15 K by ARPES tequnics[52]. (b) The spin component of ^{57}Fe Knight Shift deduced by subtracting its orbital component, revealing a spin-singlet SC state.[19].

2.3 Band Structure and Fermi Surface

The electronic structure of the Fe-based superconductors has been intensively studied both theoretically and experimentally. These main results are summarized as follows. (i) All the compounds possess a similar electronic structure. (ii) The stoichiometric parent compounds are semimetal with equal number of negative and positive charge carriers, and the dominant contribution to the density of states at Fermi level (E_F) derives from the five Fe 3*d* orbitals lightly mixed with *Pn* (or *Ch*) *p* orbitals. (iii) The Fermi surfaces (FSs) comprise disconnected quasicylindrical sheets with two hole pockets (α_1, α_2) at the center of the Brillouin zone (Γ point) and two electron pockets (β_1, β_2) centered its corner (*M* point) as shown in Fig. 2-4. An additional hole pockets sit around the Γ point [or the wave vector ($\pm\pi$, $\pm\pi$) in the *unfolded* Brillouin zone], and its presence is very sensitive to structural details. (iv) When extra electrons are injected, the electron pockets expand and the hole pockets contract. Conversely, hole doping makes the hole pockets larger and the electron pockets smaller. One important feature is that the hole and eletron pockets can be fairly well nested by a wave vector of (π, π) [or (π, 0) and (0, π)]. And this FS nesting can induce a collinear AFM order, which is consistent with the observed. However, the observed magnetic moment per Fe atom is much smaller than expected from first-principles calculations[61]. In addition, first-principles calculations have expected that the electronic structure becomes two-dimentional according as the interlayer distance between the Fe planes enlarges[62].

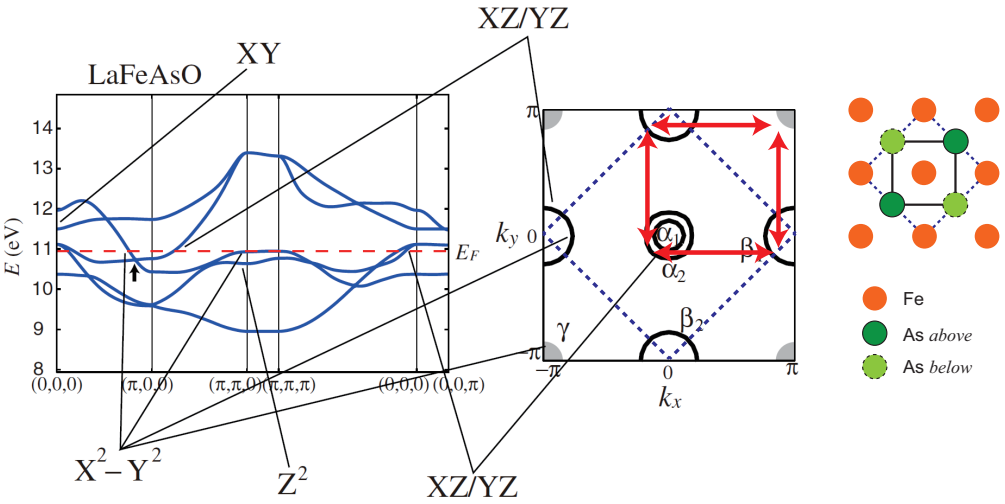

Figure 2.6: The band structure of the five-band model of LaFeAsO. The Fermi Surface at $k_z = 0$ is shown on the middle[63].

2.4 Factors Affecting T_c

- Spin dynamics
  NMR experiments revealed that in $Ba(Fe_{1-x}Co_x)_2As_2$[64] and $BaFe_2(As_{1-x}P_x)_2$[65] T_c is optimized near an AFM quantum-critical point (QCP). And superconductivity vanishes in the heavily overdoped compounds, where low-energy AFM spin fluctuations are absent. This strongly suggests that there is an intimate relationship between superconductivity and antiferromagnetism. Moreover, for these optimally doped compounds T_c appears to be scaled to spin-fluctuations temperatures[66].

- Structural parametar
  The T_c in Fe-based superconductors intimately related with parameters characterizing local structure around Fe atoms. In particular, Lee *et al.* shows that the highest T_c is obtained when *Pn* (or *Ch*)-Fe-*Pn* (or *Ch*) bond angle α forms a regular tetrahedron ($\alpha \sim 109.5°$)[67]. The importance of bond angle has also been pointed out by Zhao *et al*[68]. On the other hand, it has been shown by Mizuguchi *et al.* that T_c systematically varies with the distance between the pnictogen and Fe plane (h_{Pn}), and reaches its maximum around 1.38Å[69].

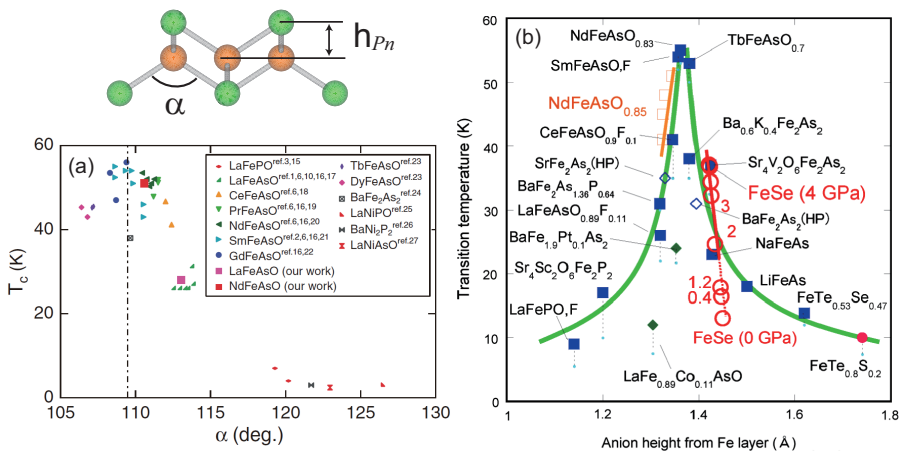

Figure 2.7: T_c vs (a) *Pn*-Fe-*Pn* bond angle[67] and (b) pnictogen height above the Fe plane[69] for various iron-pnictide superconductors.

2.5 Pairing Mechanism

Because of the close proximity of AFM order and superconductivity in the phase diagram, the possibility of magnetically mediated superconductivity has been extensively studied. Two different approaches, based on the itinerant spin fluctuations promoted by FS nesting[70, 71] and the local AFM exchange couplings[72], predict s-wave state with sign reversal of the SC-gap function between electron- and hole- FSs (the $s_{\pm}$-wave state). This scenario is supported by scanning tunneling microscopy on Fe(Te, Se)[73] and inelastic neutron scattering on (Ba,K)Fe_2As_2[74]. Moreover, it has been theoretically pointed out that the sign reversal of the gap function on the well-nested FSs lead to the suppression of HS peak and low-temperature power-law behavior in $1/T_1$ as if *nodeless* SC gaps (magnitude of order parameter, $|\Delta|$) open on all FSs[75, 76, 77].

Conversely, the orbital-fluctuation-mediated s-wave state without sign reversal (the s_{++}-wave state) has also been proposed[78]. This idea is based on the multiorbital nature of the iron pnictides, and can naturally explain an orbital polarization of d_{xz} and d_{yz} Fe states in the orthorhombic phase (x, y, and z represent ortthorhombic axes)[79] as well as softening of the lattice characterized by the shear modulus C_{66} above T_S[80]. Recently, a laser-ARPES study on $BaFe_2(As_{0.65}P_{0.35})_2$ and $Ba_{0.6}K_{0.4}Fe_2As_2$ reported that the SC gap is almost identical among the observed three holelike FSs, and the importance of orbital fluctuations in the pairing mechanism was claimed[81]. However, many other ARPES results on $BaFe_2As_2$[52, 53, 54, 55, 56], LiFeAs[57], and $FeTe_{1-x}Se_x$[60] have shown FS-dependent SC gaps.

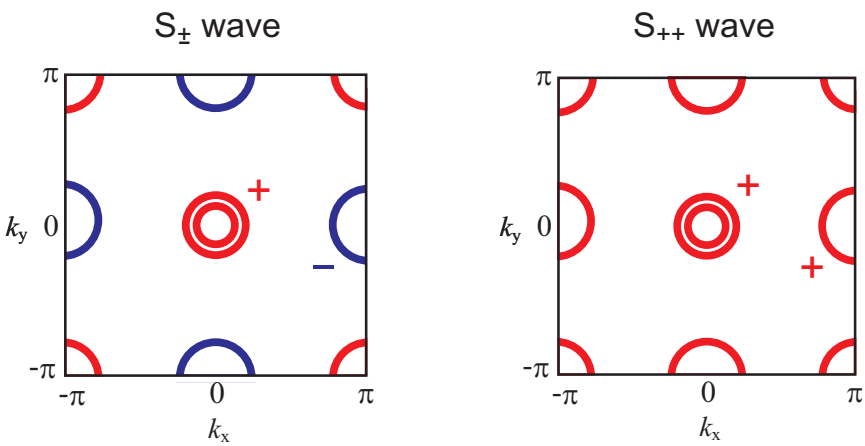

Figure 2.8: The fully gapped (a) $s\pm$ wave and (b) $s{+}{+}$ wave gap are schematically shown. The solid red (blue) curves represent positive (negative) sign of the gap.

2.6 Similarities and Differences with Cuprates

These Fe-based compounds share many similarities with the cuprates despite the marked differences in the chemical compositions as follows:

1. Both contain stacked square lattice layers of transition metals, and d electrons are responsible for physical properties.

2. Their electronic properties are two-dimensional.

3. Superconductivity emerges in close proximity to a magnetic ground state, and magnetic correlations has been suggested to be crusial for the superconductivity.

On the other hands, in following respects Fe-based supperconductors are different from cuprates.

1. The parent compounds of Fe-based superconductors are bad metals, while those of cuprate superconductors are insulating.

2. In iron pnictides, all five Fe d-bands are partially occupied and cross the Fermi level. However, the cuprates are single-band systems.

3. In most iron pnictides and chalcogenides, AFM order is always accompanied by a tetragonal-to-orthorhombic lattice distortion. SC pairing through orbital (or structural) fluctuations is also proposed.

4. Superconductivity can be induced not only by charge doping but also by applying external pressure or by isoelectronic doping, whereas in cuprates application of pressure only ehances already existing T_c.

Chapter 3

Experimental Methods and Principles

3.1 Nuclear Magnetic Resonance (NMR)

NMR is a local, real-space probe where the behavior of nuclear spins can be monitored on site-to-site basis. Since nuclei are coupled to the surrounding electrons via hyperfine interactions, NMR is widely used in solid-state studies. Its advantage is that not only static properties but also dynamics can be detected through a spin-lattice relaxation rate $1/T_1$, which relates to a dynamical susceptibility $\chi(\boldsymbol{q}, \omega)$. Furthermore, it is well known that NMR is a powerful tool to reveal the SC state. For example, the shift of a resonance peak called Kight shift sensitively depend on the spin state of Cooper pairs.

3.1.1 Nuclear magnetic resonance phenomena

Under an external magnetic field $\boldsymbol{H}_{\mathrm{ext}}$, the interaction Hamiltonian for a nuclear spin moment $\boldsymbol{\mu}_{\mathbf{N}} = \gamma_{\mathrm{N}}\hbar\boldsymbol{I}$ is given by

$$\mathcal{H}_{\mathrm{Z}} = -\boldsymbol{\mu}_{\mathbf{N}} \cdot \boldsymbol{H}_{\mathrm{ext}}, \tag{3.1}$$

which produces the split of the energy levels with $2I + 1$. When a ac-magnetic field $\boldsymbol{H}_1$ with $\omega_0 = \gamma_{\mathrm{N}} H_{\mathrm{ext}}$ is set perpendicular to the direction of $\boldsymbol{H}_{\mathrm{ext}}$, energy absorption and emission are obseved between the neighboring spin levels. Figure 3.1 shows the energy diagram of the nuslear spin system with $I = 3/2$ at the external field.

3.1.2 Nuclear spin Hamiltonian

In addition to the above Zeeman interaction, the nuclei interact with electrons by following magnetic and electric interactions in a substance: the former attributes to the Knight shift, and the latter is the origin of nuclear quadrupole

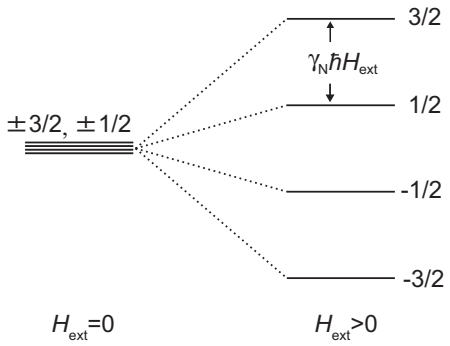

Figure 3.1: Energy diagram of the nuclear spin system with $I = 3/2$ at the external field. The degeneracy of the nuclear spin levels is solved by the Zeeman interaction $\mathcal{H}_{\mathrm{Zeeman}}$.

resonance (NQR).
A nuclear spin $\boldsymbol{I}$ with a quadrupole moment Q is represented following by Hamilton under magnetic field $\boldsymbol{H}_{\mathrm{ext}}$,

$$\mathcal{H} = \mathcal{H}_{\mathrm{Z}} + \mathcal{H}_{\mathrm{HF}} + \mathcal{H}_{\mathrm{Q}}, \tag{3.2}$$

The second term in eq. 3.2 is induced, since the quadrupole moment interacts with electronic field gradient (EFG) by surrounding electronic field, described as

$$\mathcal{H}_{\mathrm{Q}} = \frac{e^2 qQ}{4I(2I-1)}\left[3I_z^2 - I(I+1) + \eta(I_x^2 + I_y^2)\right]. \tag{3.3}$$

Here, q is defined as $eq \equiv V_{zz}$ using potential V. $V_{\alpha\beta}$ $(\alpha, \beta = x, y, z)$ shows the value of $V_{\alpha\beta} \equiv \partial^2 V/\partial\alpha\partial\beta$ at the origin. eq gives the gradient of z direction. $\eta \equiv (V_{xx} - V_{yy})/V_{zz}$ is the asymmetry factor. The last term in eq. 3.2 is magnetic interaction though hyperfine coupling,

$$\mathcal{H}_{\mathrm{HF}} = \gamma_{\mathrm{N}}\gamma_{\mathrm{e}}\hbar^2\left[\frac{8\pi}{3}\delta(\boldsymbol{r})\boldsymbol{I}\cdot\boldsymbol{S} - \left(\frac{\boldsymbol{I}\cdot\boldsymbol{S}}{r^3} - \frac{3(\boldsymbol{I}\cdot\boldsymbol{r})(\boldsymbol{S}\cdot\boldsymbol{r})}{r^5}\right) + \frac{\boldsymbol{I}\cdot\boldsymbol{l}}{r^3}\right] \tag{3.4}$$

where γ_e is an electronic gyromagnetic ratio. The first term of this expression is called Fermi contact interaction, showing the contribution from s electrons with finite probability at nuclear positions as shown in $\delta(\boldsymbol{r})$. The second and last terms represent a classical dipole-dipole interaction and interactions between nuclear spins and electronic orbital angular momentum, respectively, which are contributed from non-s electrons.

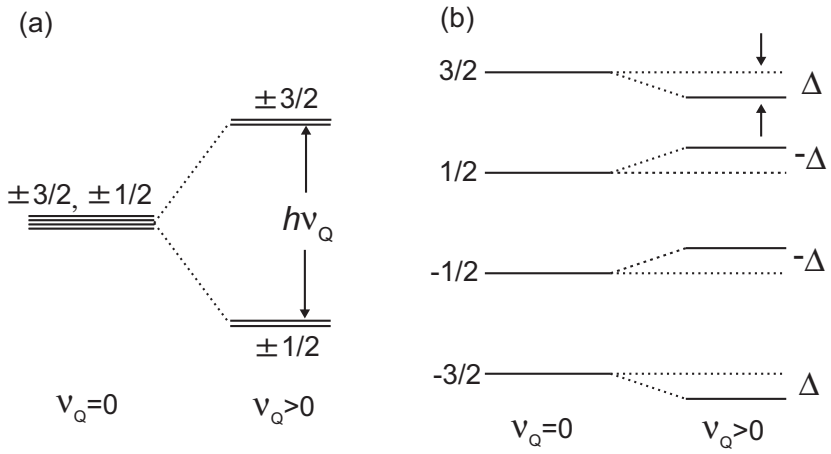

Figure 3.2: Energy diagrams of nuclear spin system with $I = 3/2$. (a) The degeneracy of the nuclear spin levels is solved by the electric quadrupole interaction $\mathcal{H}_{\mathrm{Q}}$ at zero field. Here, $h\nu_{\mathrm{Q}} = 3e^2qQ/2I(2I-1)$. (b) $\mathcal{H}_{\mathrm{Zeeman}}$ dominated spin levels are modified by $\mathcal{H}_{\mathrm{Q}}$. Δ represents $h\nu_{\mathrm{Q}}\left(3\cos^2\theta - 1\right)/4$ where θ is the angle between the principle axis of EFG and external field.

3.1.3 Knight shift

The magnetic interaction between a nuclear spin and surrounding electrons is represented by $\mathcal{H}_{\mathrm{HF}}$. Defining the internal magnetic field at nuclear position induced by electrons as $\boldsymbol{H}_{\mathrm{loc}}$,

$$\mathcal{H}_{\mathrm{HF}} = -\gamma_{\mathrm{N}}\hbar \boldsymbol{I} \cdot \boldsymbol{H}_{\mathrm{loc}} \tag{3.5}$$

$$\boldsymbol{H}_{\mathrm{loc}} = -\gamma_{\mathrm{e}}\hbar\left[\frac{8\pi}{3}\delta(\boldsymbol{r})\boldsymbol{S} - \left(\frac{\boldsymbol{S}}{r^3} - \frac{3(\boldsymbol{S}\cdot\boldsymbol{r})\boldsymbol{r}}{r^5}\right) + \frac{\boldsymbol{l}}{r^3}\right] \tag{3.6}$$

is shown. This time-dependent $\boldsymbol{H}_{\mathrm{loc}}$ is shown as follows,

$$\boldsymbol{H}_{\mathrm{loc}}(t) = \langle \boldsymbol{H}_{\mathrm{loc}} \rangle + \delta\boldsymbol{H}_{\mathrm{loc}}(t). \tag{3.7}$$

The averaged value $\langle \boldsymbol{H}_{\mathrm{loc}} \rangle$ makes the extra field, giving rise to NMR line shift. Therefore, an effective field that nuclear spin receive is expressed as,

$$\boldsymbol{H}_{\mathrm{eff}} = \boldsymbol{H}_{\mathrm{ext}} + \langle \boldsymbol{H}_{\mathrm{loc}} \rangle \tag{3.8}$$

$$= (1 + K)\boldsymbol{H}_{\mathrm{ext}}, \tag{3.9}$$

$$K \equiv \frac{\langle \boldsymbol{H}_{\mathrm{loc}} \rangle}{\boldsymbol{H}_{\mathrm{ext}}}. \tag{3.10}$$

The K, called Knight shift, is composed of temperature (T)-dependent spin part and T-independent orbital part,

$$K(T) = K_s(T) + K_{orb}, \tag{3.11}$$

$$K_s(T) = \frac{A_s}{N_A \mu_B} \chi_s(T),$$

$$K_{orb} = \frac{A_{orb}}{N_A \mu_B} \chi_{orb}. \tag{3.12}$$

Here, A_s (A_{orb}), χ_s (χ_{orb}), N_A, and μ_B are a spin (orbital) part of hyperfine coupling constant, a spin (orbital) susceptibility, the Avogadro's number, and the Bohr magneton, respectively. When electron correlations are disregarded, χ_s corresponds the Pauli paramagnetic susceptibility, $\chi_{Pauli} = 2\mu_B^2 N(E_F)$. The spin part of the Knight shift $K_s(T)$ is the efficient probe to reveal the Cooper pairing state. For spin singlet pairs, an absolute value of $K_s(T)$ is decreasing upon cooling below T_c since χ_s comes close to zero due to offsetting spin momentum. By contrast, for spin triplet pairs which have finite spin momentum, $K_s(T)$ hardly changes upon cooling below T_c.

3.1.4 Antiferromagnetic powder pattern in NMR under external fields

If an AFM ordering occurs in powder sample, NMR spectrum undergoes an appreciable broadning by the internal magnetic field as shown in Fig. 3.3. In powders, the angle (θ) between the direction of the external magnetic field $\boldsymbol{H}$ and that of the internal magnetic field $\boldsymbol{H}_{int}$ is randomly distributed. As a result, the distribution of nuclei that experiences the resonant magnetic field $\boldsymbol{H}_0$ with $H_0 = \omega_0/\gamma_N$ in the external magnetic field between H and $H + dH$ is described as

$$P(H)dH = \frac{2\pi r sin\theta}{4\pi r^2} r d\theta = \frac{1}{2} sin\theta d\theta \tag{3.13}$$

$$= \frac{1}{2} d(cos\theta). \tag{3.14}$$

Since $H = H_0 + H_{int}\, cos\theta$, in the AFM ordered state, it can be expressed as

$$P(H) = \frac{1}{2}\frac{d(cos\theta)}{dH} = \frac{1}{2H_{int}} \tag{3.15}$$

for the range of $H_0 - H_{int} < H < H_0 + H_{int}$. Here, ω_0 is the NMR frequency and γ_N is the nuclear gyromagnetic ratio. This equation gives a rectangle powder pattern of full width $2H_{int}$.

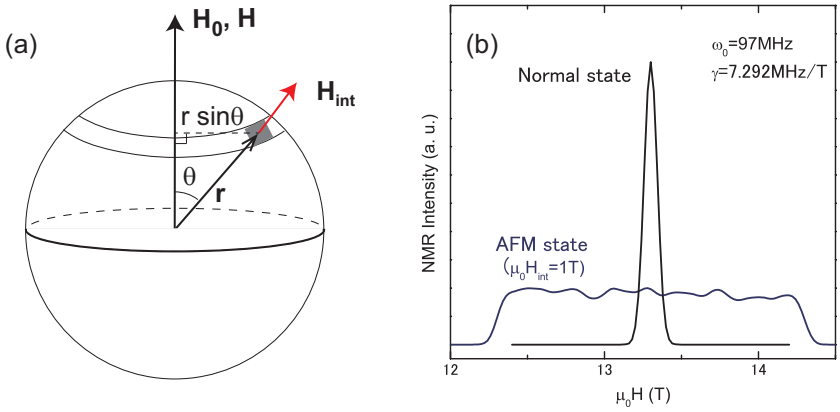

Figure 3.3: (a) Schematic image of distribution of nuclei. θ is the angle between the direction of the external magnetic field $\boldsymbol{H}$ and that of the internal magnetic field $\boldsymbol{H}_{\mathrm{int}}$. (b) The simulated NMR linehape in normal (black) and AFM state (blue) for the powder sample.

3.2 Nuclear Quadrupole Resonance (NQR)

If $I \geq 1$, the nuclei have unique sized nuclear electric quadrupole moments which are reflected in an asymmetric charge distribution of nuclei,

$$eQ = e \int_V \left(3z^2 - r^2\right) dv, \tag{3.16}$$

where z is the spin quantization axis. When the nuclei are located in lower symmetry than cubic, the degeneracy of the nuclear spin levels is solved by the electric quadrupole interaction $\mathcal{H}_{\mathrm{Q}}$ although at zero field as indicated in Fig 3.2. If the split is large enough, namely in the MHz range, the NQR spectroscopy is feasible. The resonance frequency is given by

$$\nu_m = \frac{E_m - E_{m-1}}{h} = \frac{(2m-1)\nu_Q}{2}, \tag{3.17}$$

where $h\nu_{\mathrm{Q}} = 3e^2qQ/2I(2I-1)$. Since the frequency sensitively depend on the crystal symmetry and the charge distribution around the observed nuclei, NQR is poweful tool to detect phase transition, such as structural transition and charge order, in strongly correlated electron systems.

3.3 Nuclear spin-lattice relaxation rate $1/T_1$

A nuclear spin is relaxed by the fluctuating component of internal magnetic field, $\delta \boldsymbol{H}_{\mathrm{loc}}(t)$. The nuclear spin-lattice relaxation rate, $1/T_1$ is represent as follows.

$$\begin{aligned}\frac{1}{T_1} &= \frac{\gamma_{\mathrm{N}}^2}{4}\int_{-\infty}^{+\infty}\left\langle \delta H_{\mathrm{loc}}^{+}(t)\delta H_{\mathrm{loc}}^{-}(0)e^{i\omega_{\mathrm{N}}t}\right\rangle + \left\langle \delta H_{\mathrm{loc}}^{-}(t)\delta H_{\mathrm{loc}}^{+}(0)e^{-i\omega_{\mathrm{N}}t}\right\rangle dt \\ &= \frac{\gamma_{\mathrm{N}}^2}{4}\sum_{q} A_q A_{-q}\int_{-\infty}^{+\infty}\left\langle S_q^{+}(t)S_{-q}^{-}(0)e^{i\omega_{\mathrm{N}}t}\right\rangle + \left\langle S_{-q}^{-}(t)S_q^{+}(0)e^{i\omega_{\mathrm{N}}t}\right\rangle dt\end{aligned}$$

Here, note that the $\mathcal{H}_{\mathrm{e}}$ and the S_q are electronic Hamiltonian and Fourier component of the electronic spin S, respectively, and

$$A(t) = e^{\mathcal{H}_{\mathrm{e}}t/\hbar}Ae^{-\mathcal{H}_{\mathrm{e}}t/\hbar}, \quad \langle A\rangle = \frac{\mathrm{Tr}\left[Ae^{-\mathcal{H}_{\mathrm{e}}/k_{\mathrm{B}}T}\right]}{\mathrm{Tr}\left[e^{-\mathcal{H}_{\mathrm{e}}/k_{\mathrm{B}}T}\right]}. \tag{3.18}$$

We derive following expression by using the fluctuation-dissipation theorem,

$$\frac{1}{T_1} = \frac{2\gamma_{\mathrm{N}}^2 k_{\mathrm{B}}T}{\mu_{\mathrm{B}}^2}\sum_{\boldsymbol{q}} A_{\boldsymbol{q}}A_{-\boldsymbol{q}}\frac{\mathrm{Im}\chi_{\perp}(\boldsymbol{q},\omega_0)}{\omega_0}. \tag{3.19}$$

In the case of that electron correlation is small enough to disregard it, the imaginary part of susceptibility is written as follows,

$$\mathrm{Im}\chi(\boldsymbol{q},\omega) = 4\pi\mu_{\mathrm{B}}^2\sum_{\boldsymbol{k}}\left[f(E_{\boldsymbol{k}+\boldsymbol{q}}) - f(E_{\boldsymbol{k}})\right]\delta(E_{\boldsymbol{k}} - E_{\boldsymbol{k}+\boldsymbol{q}} - \hbar\omega) \tag{3.20}$$

If we assume that $A_{\boldsymbol{q}}$ does not depend on $\boldsymbol{q}$, then we derive following relation,

$$\begin{aligned}\frac{1}{T_1} &\cong \frac{\pi}{\hbar}A^2\int_0^{\infty}\int_0^{\infty} N(E)N(E')f(E)\left[1-f(E')\right]\delta(E-E')\,dE\,dE' \\ &= \frac{\pi}{\hbar}A^2 N(E_{\mathrm{F}})^2 k_{\mathrm{B}}T.\end{aligned} \tag{3.21}$$

This expression and Knight shift gives so-called Korringa relation:

$$\frac{1}{T_1 T K_{\mathrm{s}}^2} = \frac{4\pi k_{\mathrm{B}}}{\hbar}\left(\frac{\gamma_{\mathrm{N}}}{\gamma_{\mathrm{e}}}\right)^2, \tag{3.22}$$

where γ_{e} is a electric gyromagnetic ratio.

From Eq. 3.21, $1/T_1$ in the SC state which is normalized by that at T_{c} is generally given by

$$\frac{T_1(T_{\mathrm{c}})}{T_1} = \frac{2}{k_{\mathrm{B}}T_{\mathrm{c}}}\int_0^{\infty}\frac{N_{\mathrm{s}}(E)^2 + M_{\mathrm{s}}(E)^2}{N_0^2}f(E)\left[1-f(E)\right]dE \tag{3.23}$$

where

$$N_s(E) = \frac{N_0}{4\pi}\int_0^{2\pi}\int_0^{\pi}\frac{E}{\sqrt{E^2-|\Delta(\phi,\theta,T)|^2}}\sin\theta d\theta d\phi, \tag{3.24}$$

$$M_s(E) = \frac{N_0}{4\pi}\int_0^{2\pi}\int_0^{\pi}\frac{\Delta(\phi,\theta,T)}{\sqrt{E^2-|\Delta(\phi,\theta,T)|^2}}\sin\theta d\theta d\phi, \tag{3.25}$$

and N_0 are the density of states (DOS) for quasiparticles in the SC state, the anomalous DOS originating from the coherence effect of the transition probability, and the DOS at the Fermi level in the normal state, respectively. Here, the T dependence of the SC gap function is expressed by $\Delta(\phi,\theta,T) = \Delta(T)\Delta(\phi,\theta)$ where $\Delta(T)$ represents $\Delta_0 \tanh\{1.82[1.018(T_c/T-1)]^{0.51}\}$[82, 83]. Measurements of T_1 below T_c give valuable information about the structure of SC gap.

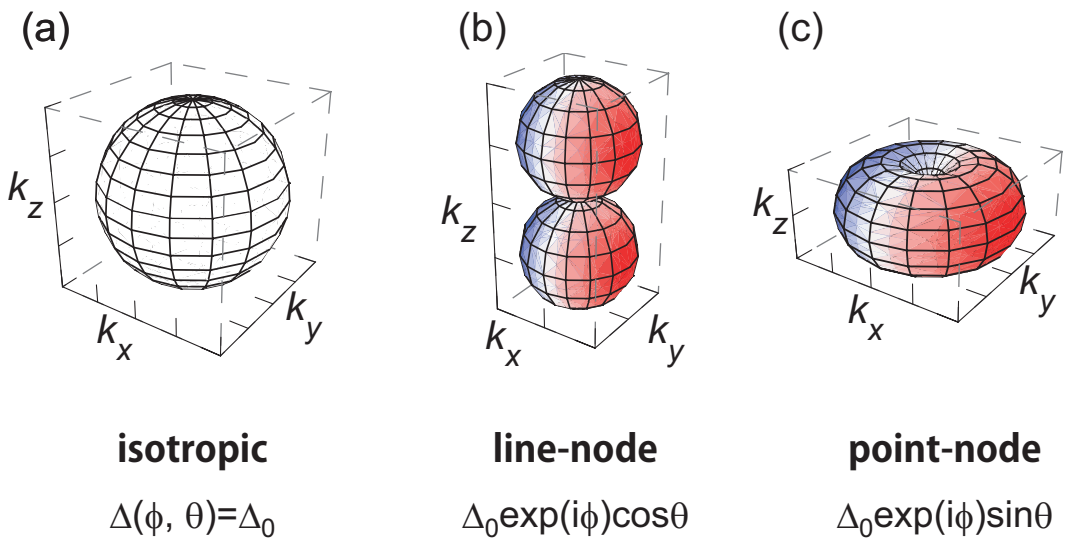

Figure 3.4: SC gap functions $\Delta(\phi,\theta)$ in k-space for (a) isotropic full gap , (b) line-node gap, and (c) point-node gap model. Color indicates sign of $\Delta(\phi,\theta)$ (red: + and blue: −).

- **isotropic full gap**

Figure 3.4(a) shows the gap function in k-space, $\Delta(\phi, \theta) = \Delta_0$ for an isotropic s-wave gap model. As a result of angular integration in Eqs. 3.24 and 3.25, $N_s(E)$ and $M_s(E)$ are given as follows:

$$N_s(E) = \begin{cases} 0 & (|E| < \Delta(T)) \\ \frac{N_0 E}{\sqrt{E^2 - |\Delta(T)|^2}} & (|E| \geq \Delta(T)) \end{cases} \tag{3.26}$$

$$M_s(E) = \begin{cases} 0 & (|E| < \Delta(T)) \\ \frac{N_0 \Delta(T)}{\sqrt{E^2 - |\Delta(T)|^2}} & (|E| \geq \Delta(T)) \,. \end{cases} \tag{3.27}$$

The energy dependence of $N_s(E)$ and T dependence of $T_1(T_c)/T_1$ for this model are shown in Figs. 3.5 and 3.6, respectively. $N_s(E)$ and $M_s(E)$ are diverged at $E \cong \Delta(T)$, which cause the peak in $T_1(T_c)/T_1$ just below T_c called the Hebel-Slichter coherence peak[84]. At low-T, $1/T_1$ is proportional to $\exp(-\Delta_0/k_B T)$. The SC gap size Δ_0 can be estimated by using this relation.

- **line-node gap**

Figure 3.4(b) shows the gap function in k-space, $\Delta(\phi, \theta) = \Delta_0 e^{i\phi} \cos\theta$ for line-node gap model. $N_s(E)$ and $M_s(E)$ are represented by

$$N_s(E) = \begin{cases} \frac{\pi}{2} \frac{N_0 E}{\Delta(T)} & (|E| < \Delta(T)) \\ \frac{N_0 E}{\Delta(T)} \arcsin \frac{\Delta(T)}{E} & (|E| \geq \Delta(T)) \,, \end{cases} \tag{3.28}$$

$$M_s(E) = 0. \tag{3.29}$$

The energy dependence of $N_s(E)$ and T dependence of $T_1(T_c)/T_1$ for this model are shown in Figs. 3.5 and 3.6, respectively. $1/T_1$ in low-T region is proportional to T^3 which is reflected in $N_s(E) \propto E$ in the $E - E_F \ll \Delta(T)$ region.

- **point-node gap**

Figure 3.4(c) shows the gap function in k-space, $\Delta(\phi, \theta) = \Delta_0 e^{i\phi} \sin\theta$ for point-node gap model. $N_s(E)$ and $M_s(E)$ are represented by

$$N_s(E) = \frac{N_0 E}{2\Delta(T)} \ln \left| \frac{E + \Delta(T)}{E - \Delta(T)} \right|, \tag{3.30}$$

$$M_s(E) = 0. \tag{3.31}$$

The energy dependence of $N_s(E)$ and T dependence of $T_1(T_c)/T_1$ for this model are shown in Figs. 3.5 and 3.6, respectively. $1/T_1$ in low-T region is proportional to T^5 which is reflected in $N_s(E) \propto E^2$ in the $E - E_F \ll \Delta(T)$ region.

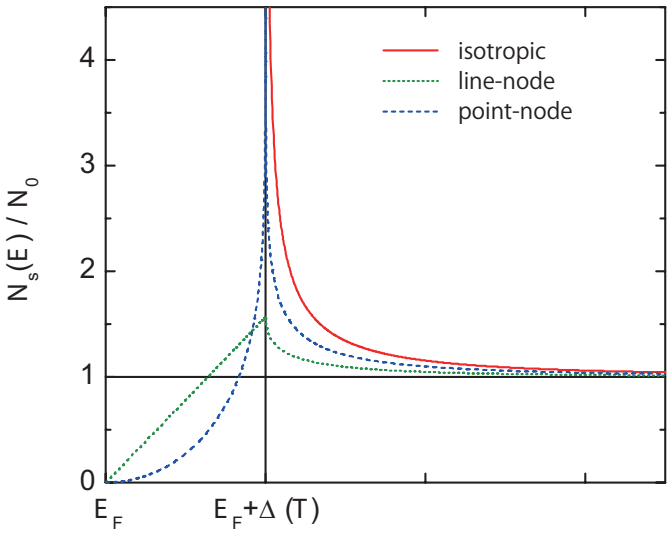

Figure 3.5: Energy dependences of DOS for quasiparticles in the SC state $N_s(E)$ which is normalized by the DOS at the Fermi level in the normal state N_0 for various SC models. $\Delta(T)$ represents $\Delta_0 \tanh\{1.82[1.018(T_c/T-1)]^{0.51}\}$.[82, 83]

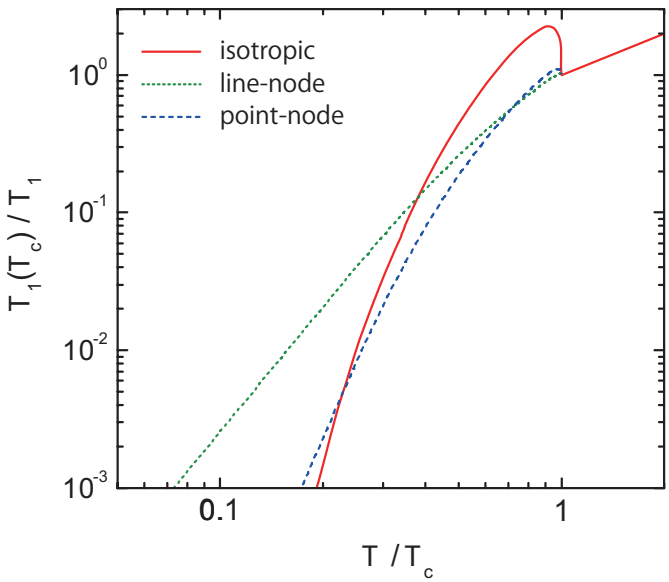

Figure 3.6: T dependences of $1/T_1$ normalized by that at T_c for various SC models. The peak just below T_c for isotropic full-gap model is called the Hebel-Slichter coherence peak[84].

Chapter 4

Sample Description

Polycrystalline samples of $(Ca_4Al_2O_{6-\delta})Fe_2(As_{1-x}P_x)_2$ with a nominal content of $0 \leq x \leq 1$ were synthesized by the solid-state reaction method using the high-pressure synthesis technique described elsewhere [17, 18]. Due to the oxidization of the starting materials, a nominal value of δ in the prepared samples may be empirically nearly zero, even though $\delta \sim 0.20$. Powder X-ray diffraction (XRD) measurements with Cu K_α radiation at room temperature, indicate that these samples are almost entirely composed of a single phase, and the lattice parameters such as the lengths along a-axis and c-axis decrease monotonously with increasing x, ensuring a homogeneous chemical substitution of P for As.

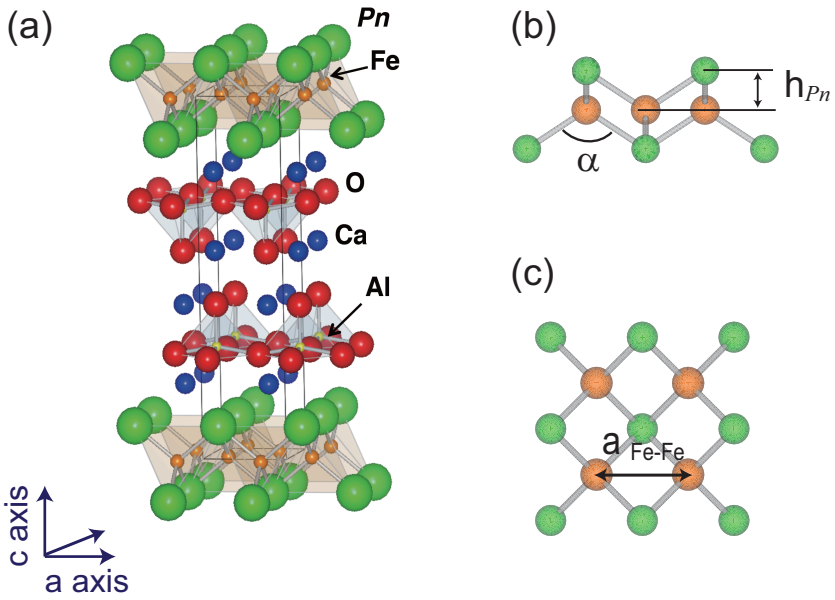

Figure 4.1: (a) Crystal structure of $(Ca_4Al_2O_6)Fe_2(As_{1-x}P_x)_2$. (b) a-axis and (c) c-axis (top) views of FePn layer. Structural parameters of the nearest-neighbour Fe-Fe distance $a_{\mathrm{Fe-Fe}}$, the pnictogen height measured from the Fe plane h_{Pn}, and the Pn-Fe-Pn bond angle are displayed.

To examine the further detailed structural parameters (atomic positions), neutron powder diffraction (NPD) measurement have been also performed on $(Ca_4Al_2O_6)Fe_2As_2$ and $(Ca_4Al_2O_6)Fe_2P_2$ by the high-resolution powder diffractometer HERMES of the Institute for Materials Research, Tohoku University, installed at the JRR-3 reactor of JAEA in Japan. Incident neutron wavelength was fixed at 1.8484Å using a Ge monochromator. The data were analyzed by the Rietveld method using the *RIETAN* program. Table 4.1 shows the atomic positions of the x=0 and x=1 compounds determined by Rietveld refinements of NPD data. The estimated Fe-As (P)-Fe bond angle α = 102.1° (109.4°) is narrowest among all the iron- arsenide (phosphide) supercpnductors. As for the intermediate compounds between x=0 and 1.0, we have not yet performed NPD measurement. Thus, the atomic position of x=0.5 and 0.75 were tentatively deduced by the analysis of powder XRD patterns through Rietveld refinements as presented in Fig. 4.2. The XRD patterns were collected by a MoKα radiation (λ=0.7107Å) with an imaging plate detector. Rietveld refinements were performed with the software Materials Studio Reflex of Accelrys, Inc. The result is shown in Table 4.2. The z coordinates of oxygen atoms of O(1) and O(2) were fixed to pre-optimized positions by the DFT calculations using the CASTEP code[85]. The x dependence of the pnictogen height (h_{Pn}) is shown in Fig. 4.3, along with the lattice parameters (a and c-axis lengths). The monotonous variation was also seen in h_{Pn} as seen in a and c-axis lengths, but the h_{Pn} data by XRD are slightly larger than the interpolation of the NPD data of the end members. This probably arises from the difference in method: (i) the reliability factor of the Rietveld refinement obtained from NPD data ($R_{wp} \sim 5\%$) is smaller than that obtained from powder XRD data ($R_{wp} \sim 7\%$). (ii) some of the parameters must be fixed in Rietveld refinements in XRD. Then, we naturally suppose that linear variation of h_{Pn} will be observed in the intermediate compounds if we perform NPD measurement in the future, because the linear variation of a and c-axis lengths suggests that the lattice parameters in the intermediate compounds follow Vegards law. Then, in the Fig. 4 of cpahter 5, we deduced h_{Pn} in the intermediate x region from a linear interpolation from x=0 to x=1.0, which is based on more reliable NPD data.

Table 4.1: Structure parameters of $(Ca_4Al_2O_6)Fe_2(As_{1-x}P_x)_2$ with $x = 0$ and 1 (space group $P4/nmm$) determined by a Rietveld refinement of NPD data at room temperature. B is the isotropic atomic displacement parameter.

(a)x=0					
lattice parameters: a = 3.7133(1)Å, c = 15.4035(6)Å					
reliability factor: R_{wp} = 5.261%					
Fe-As: 2.387Å, Fe-As-Fe: 102.1°					
Atom	Site	x	y	z	B(Å^2)
Fe	2a	3/4	1/4	0.0	0.47(5)
As	2c	1/4	1/4	0.0974(2)	0.66(8)
Ca(1)	2c	1/4	1/4	0.7997(3)	0.18(9)
Ca(2)	2c	1/4	1/4	0.5819(3)	0.33(11)
Al	2c	1/4	1/4	0.3181(4)	0.50(14)
O(1)	4f	3/4	1/4	0.2969(2)	0.50(6)
O(2)	2c	1/4	1/4	0.4340(3)	0.69(9)
(b)x=1					
lattice parameters: a = 3.69277(9)Å, c = 14.9270(5)Å					
reliability factor: R_{wp} = 4.779%					
Fe-P: 2.262(3)Å, Fe-P-Fe: 109.4(2)°					
Atom	Site	x	y	z	B(Å^2)
Fe	2a	3/4	1/4	0.0	0.40(5)
P	2c	1/4	1/4	0.0875(3)	0.06(9)
Ca(1)	2c	1/4	1/4	0.8113(3)	0.30(9)
Ca(2)	2c	1/4	1/4	0.5822(4)	0.65(14)
Al	2c	1/4	1/4	0.3109(5)	0.60(14)
O(1)	4f	3/4	1/4	0.2910(2)	0.90(6)
O(2)	2c	1/4	1/4	0.4304(3)	0.81(9)

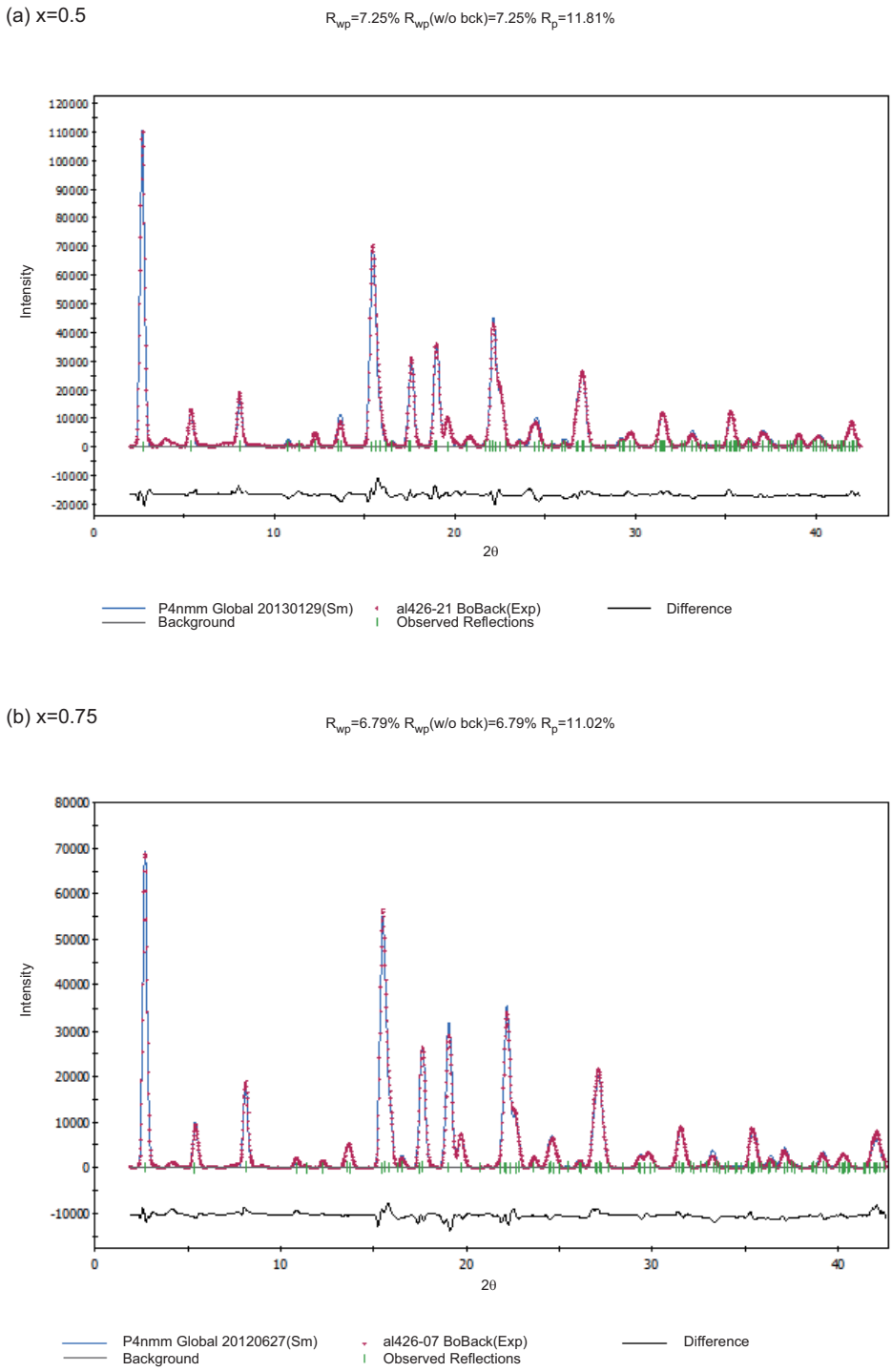

Figure 4.2: Powder XRD patterns of $(Ca_4Al_2O_6)Fe_2(As_{1-x}P_x)_2$ with (a)x=0.5 and (b)x=0.75 observed at 297K.

Table 4.2: Structure parameters of $(Ca_4Al_2O_6)Fe_2(As_{1-x}P_x)_2$ with $x = 0.5$ and 0.75 determined by a Rietveld refinement of powder XRD data at 297K. A Pseudo-Voigt function was used in this refinement.

P content	x=0.5	x=0.75
Space group	$P4/nmm$	$P4/nmm$
Lattice parameters/Å	$a = 3.705 \pm 0.001$	$a = 3.698 \pm 0.001$
	$c = 15.152 \pm 0.007$	$c = 15.057 \pm 0.007$
Cell volume/Å^3	$V = 208.0$	$V = 205.9$
Reliability factors	$R_{wp} = 7.25\%$	$R_{wp} = 6.79\%$
	$R_p = 11.81\%$	$R_p = 11.02\%$
Global isotropic	U= 0.012 ± 0.001	U= 0.015 ± 0.001
temperature factor/Å^2	($B = 1.0$)	($B = 1.2$)
Atomic parameters:		
Fe	$2a(3/4, 1/4, 0)$	$2a(3/4, 1/4, 0)$
As/P	$2c(1/4, 1/4, 0.095 \pm 0.001)$	$2c(1/4, 1/4, 0.092 \pm 0.001)$
Ca(1)	$2c(3/4, 3/4, 0.201 \pm 0.002)$	$2c(3/4, 3/4, 0.193 \pm 0.002)$
Ca(2)	$2c(3/4, 3/4, 0.421 \pm 0.002)$	$2c(3/4, 3/4, 0.419 \pm 0.002)$
Al	$2c(1/4, 1/4, 0.319 \pm 0.002)$	$2c(1/4, 1/4, 0.316 \pm 0.002)$
O(1)	$4f(3/4, 1/4, 0.289$ [fixed])	$4f(3/4, 1/4, 0.294$ [fixed])
O(2)	$2c(1/4, 1/4, 0.432$ [fixed])	$2c(1/4, 1/4, 0.430$ [fixed])

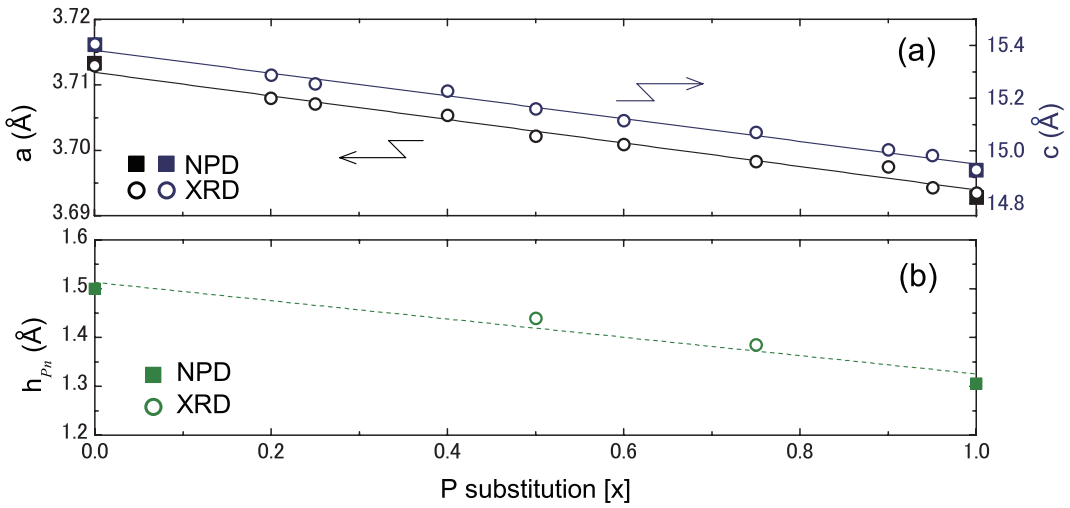

Figure 4.3: (a)x dependence of a-axis and c-axis length in $(Ca_4Al_2O_6)Fe_2(As_{1-x}P_x)_2$. (b) Plots of pnictogen height (h_{Pn}) from the Fe plane versus x. The h_{Pn} are determined from powder x-ray(circles) and neutron(squares) diffraction measurements at room temperature.

Bulk T_cs for $0 \leq x \leq 0.4$ and x=1.0 were determined from an onset of SC diamagnetism in the susceptibility measurement, whereas no SC transition was identified in $0.5 \leq x \leq 0.95$. Notably, the solid solutions in the non-superconducting range exhibit resistivity anomalies at temperatures of 50-100K as shown in Fig 4.4 (b). The behavior is reminiscent of the resistivity kink commonly observed in various non-superconducting parent compounds that signals the onset of orthorhombic distortion and/or AFM long-range order.

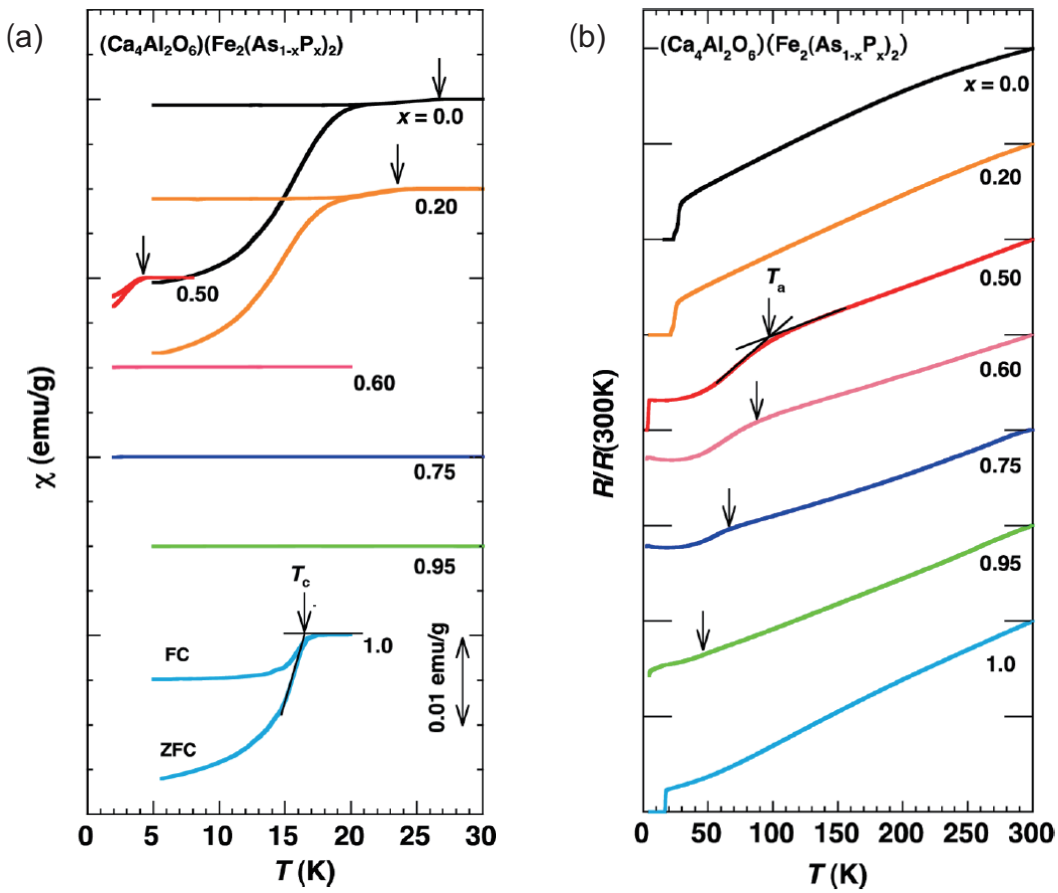

Figure 4.4: (a) Temperature dependence of the magnetic susceptibility of $(Ca_4Al_2O_6)Fe_2(As_{1-x}P_x)_2$. Black arrows indicat the onset of superconducting transitions. (b) Temperature dependence of the resistivity of $(Ca_4Al_2O_6)$ $Fe_2(As_{1-x}P_x)_2$. Resistivity anomalies (kink) are indicated by black arrows.

Chapter 5

Experimental Results

5.1 Unconventional Superconductivity and Spin Fluctuations in $(Ca_4Al_2O_6)Fe_2As_2$

5.1.1 Motivation

Relatively high SC transition has been reported in iron pnictides with a thick perovskite-type block layer, in which the interlayer distance between Fe*Pn* layers is more than ~ 13 Å [17, 86, 87, 88]. For example, T_c is ~ 47 K for $[Ca_4(Mg_{0.25}Ti_{0.75})_3O_y](Fe_2As_2)$[87], and ~ 37 K for $(Sr_4V_2O_6)(Fe_2As_2)$[88], which rises up to 46 K by the application of pressure[89]. In these series of Fe-based compounds, neither structural transition nor magnetic order has been reported so far, differentiating them from other Fe-based superconductors which exhibits superconductivity when an AFM long-range order coupled with a structural distortion is suppressed by either chemical substitution or application of pressure. On the one hand, T_c of the Fe-based superconductors is intimately related with local structural parameters such as a *Pn*-Fe-*Pn* bond angle of FePn_4 tetrahedron (*Lee's plot*)[67] and/or a height of pnictgen from Fe-plane[69]. In this context, systematic investigations on Fe-based superconductors with a thick block layer are required in order to get insight into some correlation between T_c and structural parameters and/or AFM spin fluctuations.

In this section, the results of ^{75}As-NQR studies on $(Ca_4Al_2O_6)Fe_2As_2$ with T_c = 27 K (denoted as CaAl42622(As) hereafter) is described. Measurement of nuclear-spin-relaxation rate $1/T_1$ unravel the development of significant AFM spin fluctuations and point to unconventional nodeless superconductivity.

5.1.2 Results and Discussion

^{75}As-NQR measurements have been performed on a coarse powder sample at zero external field. Figure 5.1(a) shows ^{75}As-NQR spectrum of CaAl42622(As)

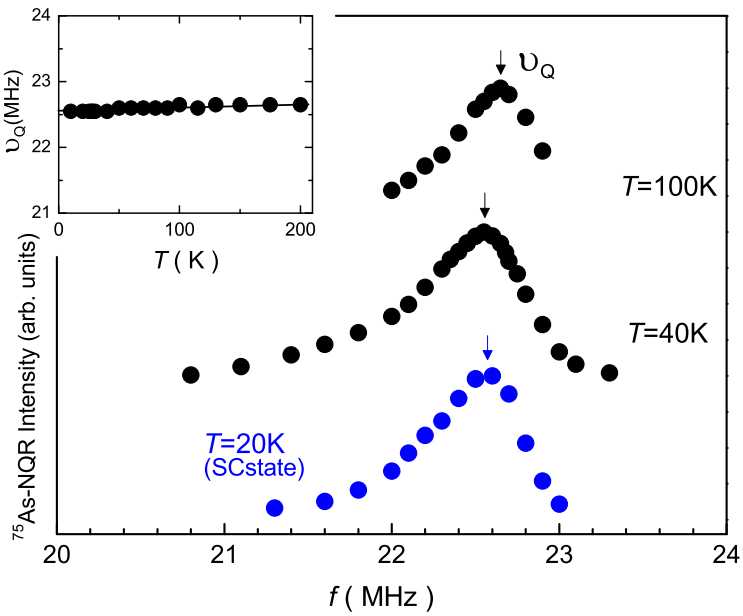

Figure 5.1: ^{75}As-NQR spectra of CaAl42622 (As). The inset shows T dependence of $^{75}\nu_Q$ of CaAl42622 (As), indicating that neither structural phase transition nor no magnetic order takes place in CaAl42622 (As).

at 20, 40, and 100K. ^{75}As-NQR frequency ($^{75}\nu_Q$) is ~ 22.6 MHz, which is the largest among Fe-based superconductors so far. In RFeAsO$_y$ (denoted as R1111 hereafter), note that $^{75}\nu_Q$ becomes large when an a-axis length decreases[90, 91]. Since $^{75}\nu_Q$ is proportional to an electric field gradient at ^{75}As nuclear site yielded by local distributions of on-site electron density and lattice ions around an ^{75}As nucleus. In this context, the fact that $^{75}\nu_Q$ in CaAl42622(As) is the largest among other Fe-based compounds may be because its a-axis length is the shortest. The ^{75}As-NQR spectrum is almost temperature (T) independent in a range of 10 K and 200 K, as shown in the inset of Fig. 5.1, demonstrating that neither structural phase transition nor magnetic order takes place in CaAl42622(As). An asymmetric shape of the ^{75}As-NQR spectra in CaAl42622(As) is probably caused by some distribution of oxygen deficiency δ.
^{75}As-NQR $1/T_1$ is obtained by fitting a recovery curve of ^{75}As nuclear magnetization to a single exponential function for I=3/2,

$$m(t) \equiv \frac{M_0 - M(t)}{M_0} = \exp\left(-3t/T_1\right). \tag{5.1}$$

Here M_0 and $M(t)$ are the respective nuclear magnetizations for a thermal equilibrium condition and at time t after a saturation pulse. In CaAl42622(As), $m(t)$ was reproduced by a single component of $1/T_1$ above 40 K, but not below ~ 40 K, as shown in Figs. 5.2(a) and 5.2(b), respectively. Since the short component $1/T_{1S}$ and the long one $1/T_{1L}$ below ~ 40 K exhibit almost the same T dependence

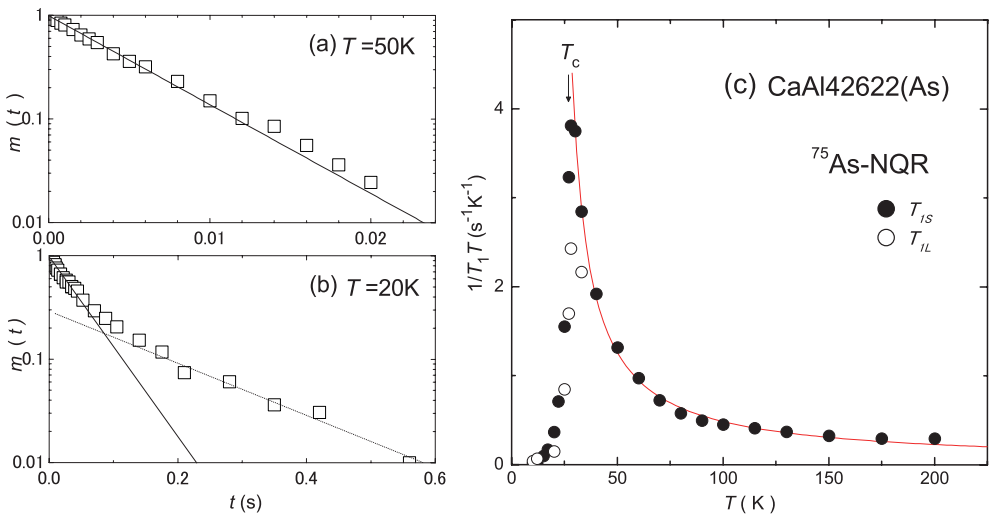

Figure 5.2: Recovery curves of ^{75}As nuclear magnetization $m(t)$ at (a) 50 K and (b) 20 K. (c) T dependence of $1/T_1T$ for CaAl42622(As). The solid curve is a simulation fitted to a relation $1/T_1T \sim a/(T+\theta)+b$ with parameters $a = 37$, $\theta = -20$ K, and $b = 0.023$.

when normalized at T_c (see Fig. 5.3(a)), we focus on the T dependence of $1/T_{1S}$ which is a dominant component below 40 K. Figure 5.2(c) shows the T dependence of the spin-lattice relaxation rate of ^{75}As nuclei divided by temperature, $1/T_1T$ for CaAl42622(As). The $1/T_1T$ in the normal state increases significantly upon cooling down to T_c. The AFM spin fluctuations in Fe-based superconductors are enhanced by the nesting of hole and electron Fermi surfaces (FSs). In general, $1/T_1T$ is described as

$$\frac{1}{T_1T} \propto \sum_{\boldsymbol{q}} |A_{\boldsymbol{q}}|^2 \frac{\chi''(\boldsymbol{q},\omega_0)}{\omega_0}, \tag{5.2}$$

where $A_{\boldsymbol{q}}$ is a wave-vector ($\boldsymbol{q}$)-dependent hyperfine-coupling constant, $\chi(\boldsymbol{q},\omega)$ a dynamical spin susceptibility, and ω_0 an NQR frequency. When a system is close to an AFM QCP, two-dimensional (2D) AFM spin-fluctuation model predicts a relation of $1/T_1T \propto \chi_Q(T) \propto 1/(T+\theta)$ [92]. Here, staggered susceptibility $\chi_Q(T)$ with an AFM propagation vector $\boldsymbol{q}$=$\boldsymbol{Q}$ follows a Curie-Weiss law. Since $1/T_1T$ diverges towards $T \to 0$ when $\theta = 0$, θ is a measure of how close a system is to an AFM QCP. Actually, as shown by the solid line in Fig. 5.2(c), the $1/T_{1S}T$ in CaAl42622(As) can be fitted by assuming $1/T_1T \sim a/(T+\theta)+b$ with parameters $a = 37$, $\theta = -20$K, and $b = 0.023$. It is unexpected that θ is negative, meaning that the staggered susceptibility would diverge toward 20K, and hence an AFM order would be anticipated below $\sim$ 20 K. As a matter of fact, in the case of $Ba(Fe_{1-x}Co_x)_2As_2$ and $BaFe_2(As_{1-x}P_x)_2$, the AFM order sets in when θ becomes negative[64, 65]. However, SC occurs below T_c=27 K in CaAl42622(As), instead of an AFM order. This is because a thick blocking layer between the FeAs layers

makes an interlayer magnetic coupling weak, suppressing an onset of AFM order. Besides, the structure consisting of perovskite blocks bonded by strong covalent bonding prevents a structural phase transition into an orthorhombic phase. These might be the main reasons why an AFM order of Fe*Pn* layers is absent in the Fe-pnictides family with the thick block layers.

The band calculation for CaAl42622(As) reported by Miyake *et al.* revealed that an additional hole FS around Γ′ $(\pm\pi, \pm\pi)$ in the *unfolded* FS regime appears explicitly as a result of the small $\alpha \sim 102°$, whereas one of two-hole FSs at Γ $(0, 0)$ is missing[93]. Eventually, it is concluded that the well nested FS topology between hole FSs at Γ and Γ′, and electron FSs at $M((0, \pi)$ and $(\pi, 0))$ enhances a Stoner factor of antiferromagnetism in CaAl42622(As) [94]. This event leads to the development of AFM spin fluctuations and hence is consistent with the experiment presented here.

Next, we address SC characteristics emerging under the background of AFM spin fluctuations. Figure 5.3(a) shows a plot of $T_1(T_c)/T_1$ normalized at T_c against T/T_c, exhibiting a steep decrease upon cooling without the coherence peak just below T_c. The T dependence of $1/T_1$ seems to follow a $\sim T^7$ dependence down to $\sim 0.3T_c$, which is quite unique as compared with the T^3 in optimally-doped La1111(OPT) with T_c=28 K [90, 95] and the T^5 in optimally-doped $Ba_{0.6}K_{0.4}Fe_2As_2$ (BaK122(OPT)) with T_c=38 K[47]. Notably, Fig. 5.3(b) shows the T dependence of $1/T_1T$ normalized at T=250 K in these compounds. We remark that as AFM spin fluctuations are more significantly enhanced, a power-law reduction in $1/T_1$ below T_c becomes steeper from $\sim T^3$ to $\sim T^7$.

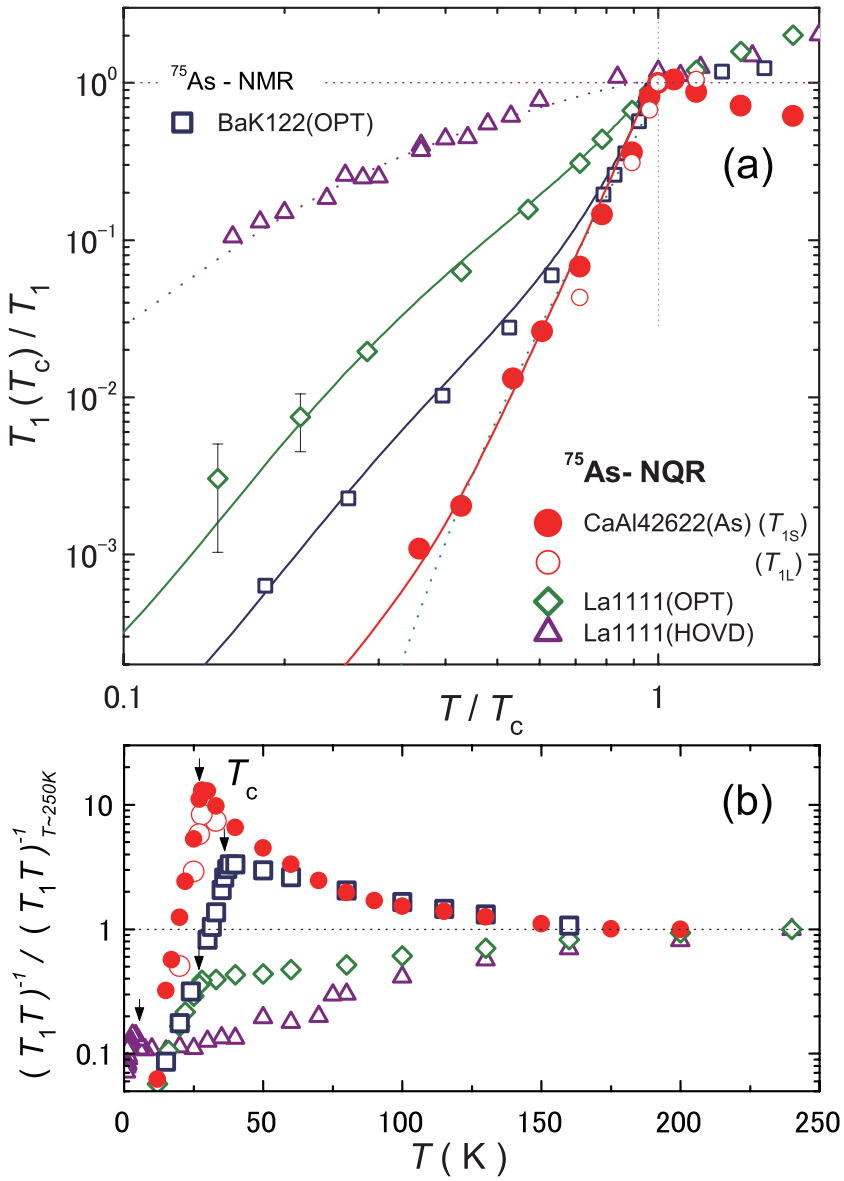

Figure 5.3: (a) Plots of ^{75}As-NQR $T_1(T_c)/T_1$ normalized at T_c against T/T_c for CaAl42622(As), along with the results of BaK122(OPT) with T_c=38 K[47], La1111(OPT) with T_c=28 K [90], and La1111(HOVD) with T_c=5 K[102]. Note that T dependences of T_{1S} and T_{1L} normalized at T_c for CaAl42622(As) are almost the same below T_c. The solid curves are simulations in terms of the $s_{\pm}$-wave model with multiple SC gaps (see text). (b) T dependence of ^{75}As-$(1/T_1T)$s normalized at T=250 K.

In previous studies[47, 96], the non-universal T-dependence in $1/T_1$ was consistently accounted for by a multigap nodeless $s_\pm$-wave pairing model[97, 98, 99, 100, 101]. In the $s_\pm$-wave model with two isotropic gaps, an initial decrease of $1/T_1$ without the coherence peak just below T_c is due to the opening of a large SC gap with $2\Delta_0^L/k_BT_c$[96]. As seen in Fig. 5.4(a), the initial decrease in $1/T_1$ just below T_c in CaAl42622(As) is similar to that in BaK122(OPT). This means that the large SC gap is comparable in these compounds. On the other hand, the $1/T_1$ for CaAl42622(As) decreases more steeply than in BaK122(OPT) as temperature falls well below T_c. This is primarily because the fraction of the density of states (DOS) at the Fermi level for FSs with a small SC gap, $r_S \equiv N_s^S/(N_s^L + N_s^S)$ is smaller for CaAl42622(As) than for BaK122(OPT). Here N_L and N_S represent the respective DOSs with large and small SC gaps. Actually, the result was well reproduced, assuming that r_S ~0.1 for CaAl42622(As) is smaller than r_S ~0.3 for BaK122(OPT)[47]. It is deduced that N_s^S is significantly smaller in CaAl42622(As) than in BaK122(OPT). Note that in the simulation, a gap ratio Δ_0^S/Δ_0^L=0.35, a smearing factor η=0.14Δ_0^L, and a coefficient of coherence factor $\alpha_c \sim 0$ (see ref. [102]) were used in BaK122 (OPT) [47] for simplicity. Even when N_s^S=0 or r_S=0 is assumed, the experiment can be also reproduced with η ~0.3Δ_0^L larger than η=0.14Δ_0^L for r_S ~0.1, as shown by the broken line in Fig. 5.4(a).

Next, we present an attempt to simulate a relaxation behavior below T_c for various Fe-based superconductors by changing the coefficient of coherence factor α_c. In this simulation, $\alpha_c = 1$ is assumed for sign-conserving *intraband* scattering and $\alpha_c = -1$ for sign-nonconserving *interband* scattering. The value varies in the range $-1 \leq \alpha_c \leq 1$ dependent on the weight of their contribution in the nuclear relaxation process. In the previous studies on the heavily-overdoped $LaFeAsO_{1-x}F_x$(La1111(HOVD)) with T_c=5 K[102] and optimally-doped La1111 (OPT) with T_c=28 K[90], the experiments were reproduced with $\alpha_c \sim 0.33$ for La1111(HOVD) and $\alpha_c \sim 0$ for La1111(OPT), as shown in Fig. 5.4(b), which is attributed to the fact that the nesting condition of FSs becomes significantly worse in heavily overdoped regime. On the other hands, in CaAl42622(As), AFM spin fluctuations develop significantly due to more dominant interband scattering than in the others. Relevant to this event, the experiment can be also reproduced by assuming a *negative value* of $\alpha_c \sim -0.86$, as indicated in Fig. 5.4(b), which contrasts with the previous studies. Here, $r_S \leq 0.1$ and $2\Delta/k_BT_c = 6.1$ were used along with other parameters used in La1111(OPT) with $T_c = 28$ K[47, 102]. It should be noted that the overall T dependence of $1/T_1$ below T_c in Fe-based superconductors is consistently accounted for by the $s_\pm$-wave model with isotropic multiple gaps mainly through changing the coefficient of coherence factor α_c. We highlight the fact that the dominant *interband* scattering due to the nesting of hole and electron FSs is responsible for the marked enhancement of 2D AFM spin fluctuations and the sign-nonconserving *interband* scattering is responsible for the T^7-like reduction behavior in $1/T_1$ without the coherence

peak below T_c.

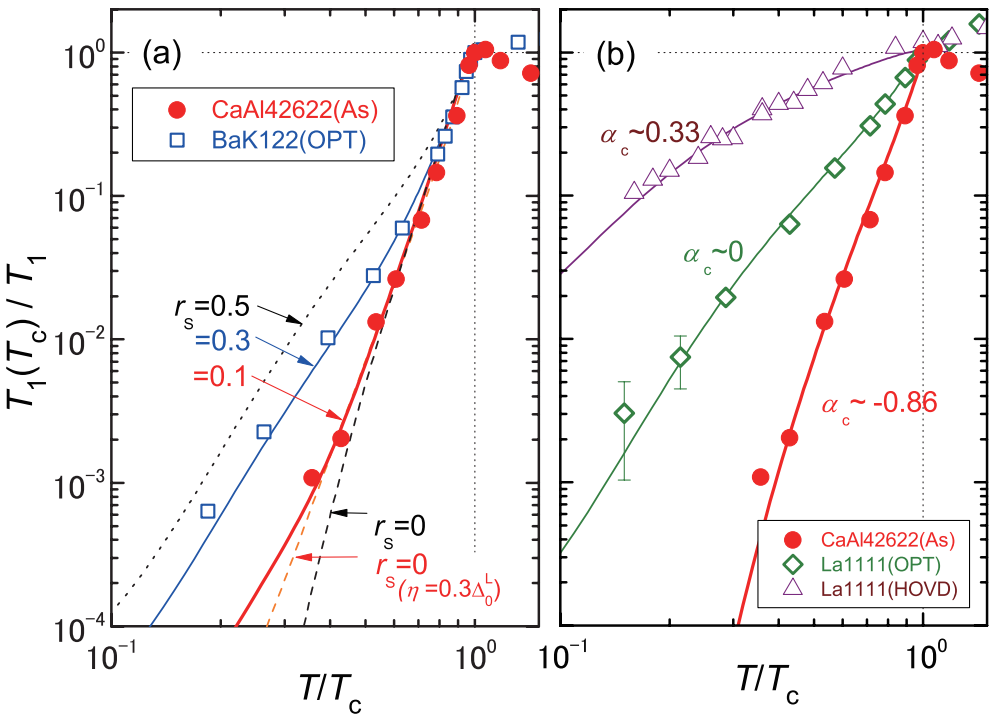

Figure 5.4: (a) Plots of ^{75}As-NQR $T_1(T_c)/T_1$ normalized at T_c against T/T_c for CaAl42622(As) and BaK122(OPT) with T_c=38 K[47]. The curves are simulations in terms of the $s_\pm$-wave model with two isotropic gaps with various values of $r_S \equiv N_s^S/(N_s^L + N_s^S)$. Here N_L and N_S represent the respective DOSs with large and small SC gaps. The experimental result for CaAl42622(As) was reproduced with r_S ~0.1, which is smaller than r_S ~0.3 for BaK122(OPT) [47]. (b) Similar plots for CaAl42622(As), La1111(OPT) with T_c=28 K[90] and La1111(HOVD) with T_c=5 K[102]. The experiment for CaAl42622(As) can be also reproduced by assuming a *negative value* of $\alpha_c \sim -0.86$, which contrasts with $\alpha_c \sim 0.33$ in La1111(HOVD) and $\alpha_c \sim 0$ in La1111(OPT).

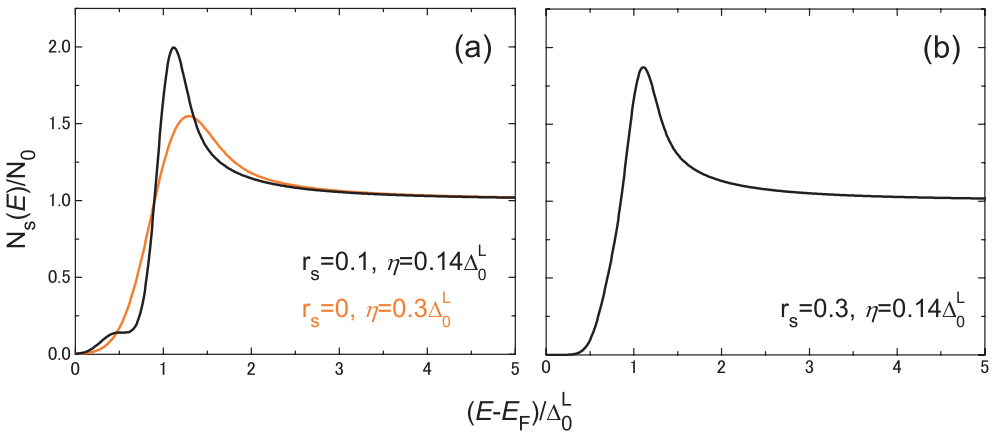

Figure 5.5: The energy dependences of the density of states used above simulations.

We have shown two possible simulations to reproduce the characteristic T dependence of $1/T_1$ in the SC state of CaAl42622(As). It is notable that, in either case, the assumption of r_S ≤0.1 and $\alpha_c \leq 0$ were necessary, implying that the SC gaps on hole and electron FSs are nodeless with comparable sizes and the opposite signs. This event may be related to the band-calculation result that one of the hole FSs around Γ(0,0) disappears[93]. Nevertheless, AFM spin fluctuations are more significant in CaAl42622(As) with T_c=27 K than in La1111(OPT) with T_c=28 K, but T_c is comparable for both. This result reveals that AFM spin fluctuations are not a unique factor for enhancing T_c. Theoretically, within a spin-fluctuation mediated pairing theory on a five-orbital model, Usui *et al.* have claimed that the reduction of multiplicity of FSs in CaAl42622(As) is a main reason why the T_c of CaAl42622(As) is not so high even when AFM spin fluctuations are more remarkable than in existing Fe-based superconductors[94]. Since the FS topology is tuned by varying structural parameters such as pnictgen height and As-Fe-As bond angle α, further systematic experiments are desired on a same series of Fe-based compounds.

Finally, we comment on an s_{++}-wave model within orbital-fluctuation mediated pairing theory[78]. In general, the suppression of the coherence peak takes place in the strong-coupling regime of s-wave SC with relatively high T_c since strong-coupling effect causes T_c not only to increase, but also causes the lifetime of quasiparticles to shorten due to some damping effect[103, 104]. For example, in a strong-coupling s-wave superconductor $TlMo_6Se_{7.5}$ with T_c=12.2 K, the coherence peak is suppressed due to the phonon damping effect more significantly than in a weak-coupling one $Sn_{1.1}Mo_6Se_{7.5}$ with T_c=4.2 K[103]. A similar behavior was also observed for MgB_2 (T_c ~40 K) and NbB_2 (T_c=5 K)[104]. In Fe-based superconductors, the marked decrease of $1/T_1$ just below T_c is most significant in CaAl42622(As) with T_c=27 K among existing Fe-based supercon-

ductors, despite the fact that T_c is not so high relatively. It seems unlikely that the suppression of the coherence peak observed universally in most Fe-based superconductors can be systematically accounted for in terms of an s_{++}-wave model. Moreover, a non-magnetic impurity effect in La1111 compounds is not compatible with the s_{++}-wave state at all; While the crystal structure and electronic state are not modified by non-magnetic Zn substitution, the SC with T_c = 24 K disappears by 3% Zn substitution [105, 106].

5.2 Possible Nodal Gap Superconductivity in $(Ca_4Al_2O_6)Fe_2P_2$

In spite of the tremendous studies on the FeAs-based superconductors, the SC mechanism of Fe-pnictides still remains controversial. In most of the FeAs-based compounds, the AFM spin fluctuations associated with nesting between multiple FSs are widely observed in association with the occurrence of superconductivity; the FSs are fully gapped in the SC state. On the other hand, the FeP-based compounds possess quite different magnetic and SC nature from their arsenide counterparts though both share a similar FS topology. Furthermore, the superconductivity of the FeP-based compounds mostly exhibits without chemical doping at ambient pressure, and their SC states has been suggested to possess nodes in the gap function by the penetration depth measurements on LaFePO[107, 108] and LiFeP[109] and by point-contact Andreev-reflection spectroscopy measurement on $(Sr_4Sc_2O_6)Fe_2P_2$[110]. Additionally, neither structural nor magnetic phase transition has been reported so far in these systems. Early NMR experiments on $(La_{0.87}Ca_{0.13})FePO$ showed moderate ferromagnetic spin fluctuations in the normal state. These experimental facts are in contrast with those of the usual FeAs-based superconductors[111]. We believe that the superconductivity of the FeP-based and FeAs-based compounds may originate from the same framework of pairing mechanism.

In this section, we describe the results of ^{31}P NMR studies on $(Ca_4Al_2O_6)Fe_2P_2$, which exhibits the highest $T_c \sim 17$ K among the FeP-based superconductors. The experimental results have revealed the unconventional superconductivity emerging under the presence of AFM spin fluctuations, which is the first report among all FeP-based superconductors. This allows us to deal with FeP-based compounds as well as in FeAs-based ones, when the pnictogen height (h_{Pn}) is as high as that of FeAs-based ones.

5.2.1 Results and Discussion

A powder sample of CaAl42622(P) was used for the NMR measurements of ^{31}P nucleus ($I = 1/2$, $^{31}\gamma/2\pi = 17.237$MHz/T). Figure 5.6 shows ^{31}P NMR spectra obtained by Fourier transformation of the spin-echo signals in a fixed magnetic field of 1 T. The NMR spectrum consists of a single and isotropic line as expected for $I = 1/2$ nuclei. Thus, we determined the ^{31}P Knight shift ^{31}K from a peak position of the spectrum. Note that $^{31}K = 0$ was determined with using H_3PO_4 as a reference. As indicated in Fig. 5.7, the ^{31}K is nearly T invariant in the normal state, but decrease below $T_c \sim 17$K.

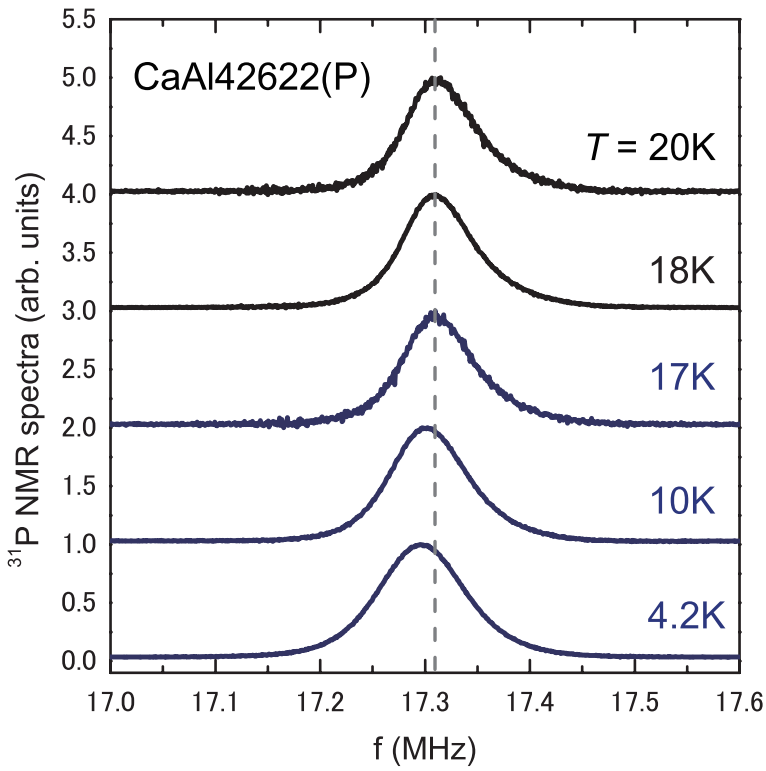

Figure 5.6: T dependence of ^{31}P NMR spectrum for CaAl42622(P). Knight shift decreases below T_c(= 17 K).

Nuclear spin-lattice relaxation rate $1/T_1$ was obtained from the recovery of nuclear magnetization by fitting with a theoretical curve of $m(t) \equiv [M_0 - M(t)]/M_0 = exp(-t/T_1)$, where M_0 and $M(t)$ are the respective nuclear magnetization of ^{31}P for the thermal equilibrium condition and a time after the saturation pulse. Figure 5.7 shows T dependence of $1/T_1T$, which increases upon cooling down to T_c like CaAl42622(As). Since the ^{31}K does not change in the normal state, this $1/T_1T$ result indicates that the spin fluctuations at $\boldsymbol{q} \neq \mathbf{0}$ develop toward T_c. Actually, as shown by the red curve in Fig. 5.7, the T dependence of $1/T_1T$ for CaAl42622(P) can be fitted by assuming $1/T_1T = a/(T + \theta) + b$ with parameters $a = 1.81$, $\theta = 39.4$ K, and $b = 0.027$. This indicates that the strong AFM spin fluctuations induce high-T_c superconductivity in the $(Ca_4Al_2O_6)Fe_2(As_{1-x}P_x)_2$ series. The similar trend appears in 122 superconductors; the enhancement of $1/T_1T$ above T_c becomes distinct in going from optimally doped $SrFe_2(As_{1-x}P_x)_2$ with $T_c \sim 26$ K, $BaFe_2(As_{1-x}P_x)_2$ with $T_c \sim 30$ K, to $(Ba_{1-x}K_x)Fe_2As_2$ with $T_c \sim 38$ K.

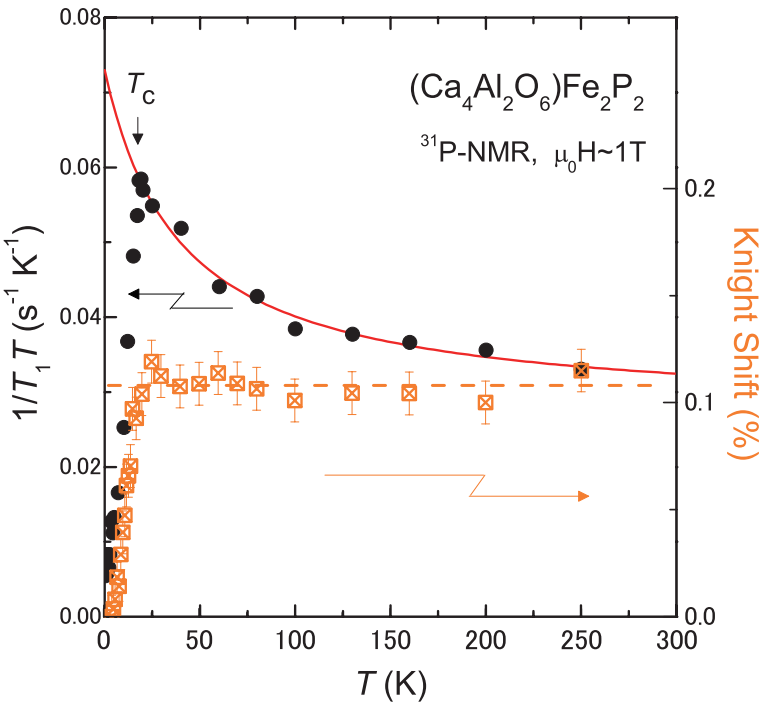

Figure 5.7: T dependence of the ^{31}P-NMR- $1/T_1T$ and Knight shift K for CaAl42622(P).

Next, we address the SC characteristics in CaAl42622(P) with $T_c \sim 17$ K. Figure 5.8(a) presents the T dependence of $T_1(T_c)/T_1$ of ^{31}P-NMR in the SC state at CaAl42622(P), which decreases markedly without any trace of a coherence peak below T_c, followed by a T-linear dependence well below T_c. This T_1T=const. behavior at low-T probes the presence of residual density of states (RDOS) at the Fermi level at an external field H = 1T, pointing to the SC realized with nodal gap. This nodal SC at x=1 is in contrast with the nodeless SC at CaAl42622(As). For CaAl42622(As), the $1/T_1T$ decreases steeply without any coherence peak down to zero toward $T \rightarrow 0$ K as presented in Fig. 5.8(b) [15].
Generally, the RDOS at E_F is induced for the nodal SC state by either applying H or the presence of some impurity scattering. Since $1/T_1T$ is related to the square of RDOS at E_F ($N^2_{\rm res}$), the ratio of RDOS to a normal-state DOS (N_0) is given by

$$\frac{N_{\rm res}}{N_0} = \sqrt{\frac{(T_1T)^{-1}_{T\rightarrow 0}}{(T_1T)^{-1}_{T=T_c}}}. \tag{5.3}$$

This relationship enables us to deduce $N_{\rm res}/N_0 \sim 0.33$ for CaAl42622(P) and $N_{\rm res}/N_0 \sim 0$ for CaAl42622(As). The solid line for CaAl42622(P) in Fig. 5.8(b) is a tentative simulation based on the multiple-gap $s_{\pm}$-wave model. In this model, the nodal gap is on one of the multiple bands that is responsible for the RDOS and a larger gap with $2\Delta_L/k_BT_c = 3.7$ is on other bands that are mainly responsible for SC [128].

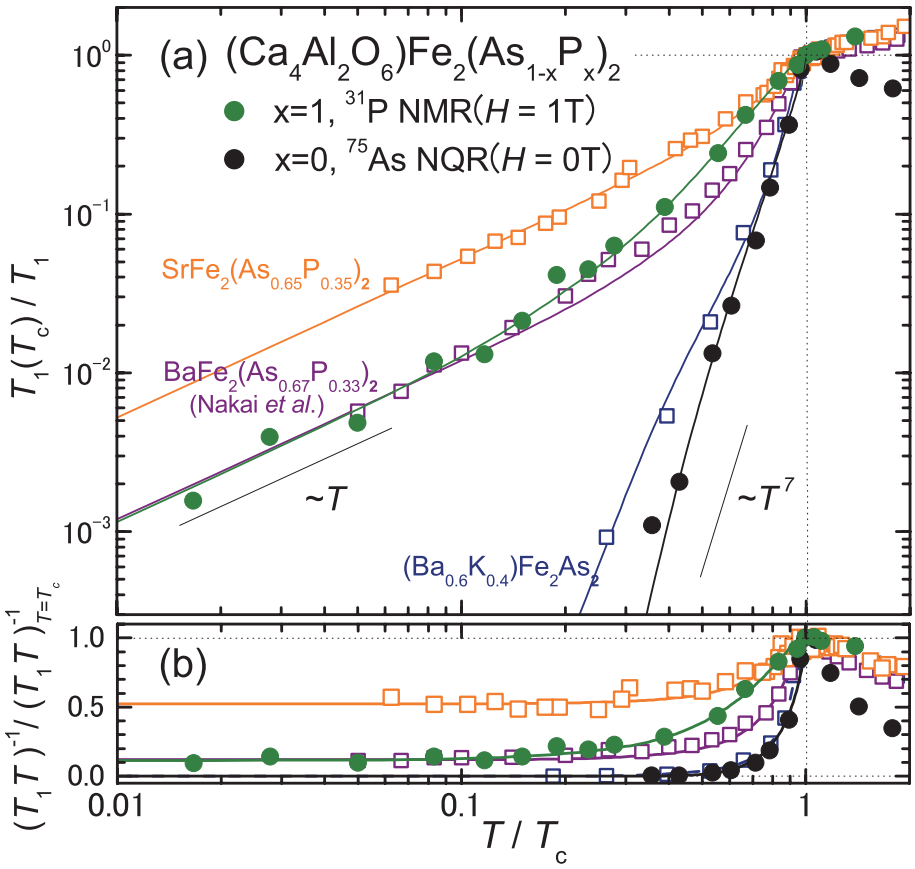

Figure 5.8: (b) Plots of ^{31}NMR - $T_1(T_c)/T_1$ and (c) $(T_1T)^{-1}/(T_1T)^{-1}_{T_c}$ versus T/T_c in the SC state at x=1 along with that at x=0 [15]. The T-linear dependence in $1/T_1$ well below T_c at x=1 indicates the presence of the residual DOS at E_F in association with the nodal SC in contrast with the nodeless SC at x= 0 [15].

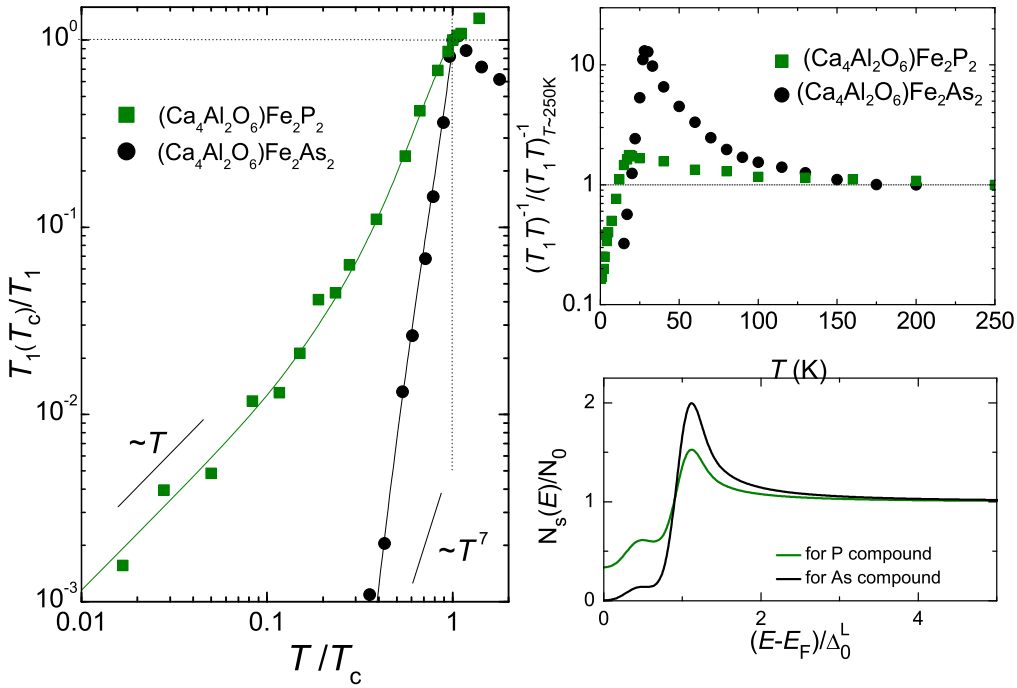

Figure 5.9: (a) T dependence of ^{31}P ($T_1(T_c)/T_1$) normalized T_c for $Ca_4Al_2O_6Fe_2P_2$, along with the results reported for $Ca_4Al_2O_6Fe_2As_2$. The multiple fully gapped $s_{\pm}$-wave model allows us to deduced the energy dependences of the density of states (c) through the fitting of the experimental $1/T_1$. (b) T dependence of $(T_1T)^{-1}$ normalized at $T \sim 250K$ for $Ca_4Al_2O_6Fe_2P_2$ and $Ca_4Al_2O_6Fe_2As_2$.

5.3 Phase Diagtram of $Ca_4Al_2O_6Fe_2(As_{1-x}P_x)_2$

5.3.1 Motivation

The parent compounds of Fe-based superconductors are AFM semimetal characterized by an average iron valence Fe^{2+} in $(FePn)^-$ layer separated by various block layers. These compounds are *R*FeAsO ("1111") (*R*=rare earth)[11, 20, 112], *Ae*Fe_2As_2 ("122") (*Ae*=Alkaline earth)[113, 114], and $(Ae_4M_2O_6)Fe_2As_2$ ("42622") (*M*=Sc, V, Al, etc.)[115, 116, 117]. By contrast, the onset of AFM order has not yet been reported in Fe-phosphide parent compounds with the Fe^{2+} in $(FeP)^-$ layer. For *A*Fe*Pn* ("111") family, the parent compound NaFeAs exhibits an AFM order like other undoped iron arsenides [118, 119, 120], whereas a fully gapped or nodeless SC emerges in LiFeAs without any carrier doping [121, 122, 123, 109]. Meanwhile, the isovalent substitution of P for As in $BaFe_2(As_{1-x}P_x)_2$ (hereafter denoted as Ba122(As,P)) brings about the SC with nodal gap [124, 125, 126, 127]. Thus, the compounds with the Fe^{2+} state in $(FePn)^-$ layers undertake an intimate evolution into either the nodeless SC in LiFeAs and $(Ca_4Al_2O_6)Fe_2As_2$[15] or the nodal SC in Ba122(As,P) without any change in the valence condition of the Fe^{2+} in the $(FePn)^-$ layer. To gain further insight into a novel phase evolution when the Fe^{2+} state is kept in the $(FePn)^-$ layer, we have dealt with $(Ca_4Al_2O_6)Fe_2(As_{1-x}P_x)_2$ (hereafter denoted as CaAl42622(As,P)) in which the Fe^{2+} state is expected irrespective of the P-substitution for As in the $(FePn)^-$ layer separated by a thick perovskite-type block[15, 17]. Here, note that a highly two-dimensional electronic structure in these compounds is in contrast with the three-dimensional one observed in *Ae*122(As,P)(*Ae*=Ba,Sr) [124, 127, 128].

In this section, we present a peculiar phase diagram for CaAl42622(As,P) with the isovalent chemical substitution of P for As and hence without any carrier doping. ^{31}P- and ^{75}As-NMR studies have revealed that a commensurate AFM order taking place in $0.5 \leq x \leq 0.95$ intervenes between a nodeless SC in $0 \leq x \leq 0.4$ and a nodal one around x=1. We highlight that as the substitution of P for As decreases a pnictogen height measured from the Fe plane (h_{Pn}), the nodeless SC state evolves into an AFM-order state and subsequently into a nodal SC state, while keeping the Fe^{2+} state due to the isovalent substitution of P for As. We remark that this finding points to the importance of the electron correlation effect for the emergence of SC as well as AFM order in iron pnictides in general.

5.3.2 Results and Discussion

Figure 5.10 (a) shows temperature (T) dependence of the ^{31}P-NMR spectrum at x=0.75 at a fixed frequency f_0=97 MHz. At temperatures higher than 70 K, the ^{31}P-NMR spectrum is composed of a single sharp peak. The spectrum becomes significantly broader upon cooling below 60 K and finally exhibits a

rectangular-like spectral shape at ~10 K. This characteristic NMR shape is a powder pattern expected for the case where the ^{31}P nucleus experiences a uniform off-diagonal internal hyperfine field $H_{\rm int}$ associated with a commensurate stripe-type AFM order of Fe-3d electron spins [129](see subsection 3.1.4). From this, the $^{31}H_{\rm int}$ ≃0.19 T at ^{31}P is estimated at 10 K for x=0.75. The $^{75}H_{\rm int}$ ≃0.58 T at ^{75}As is evaluated from fitting ^{75}As-NMR spectrum as shown in Fig 5.10 (b). Here, note that $^{75}H_{\rm int}$ is larger than $^{31}H_{\rm int}$ because of the hyperfine-coupling constant $^{75}A_{\rm hf}$ being larger than $^{31}A_{\rm hf}$. Using the relationship of $^{75}H_{\rm int}$=$^{75}A_{\rm hf}M_{\rm AFM}$, a Fe-AFM moment $M_{\rm AFM} \sim 0.23\mu_B$ is estimated assuming $^{75}A_{\rm hf} \sim 2.5T/\mu_B$ which is cited from previous reports [129, 44].

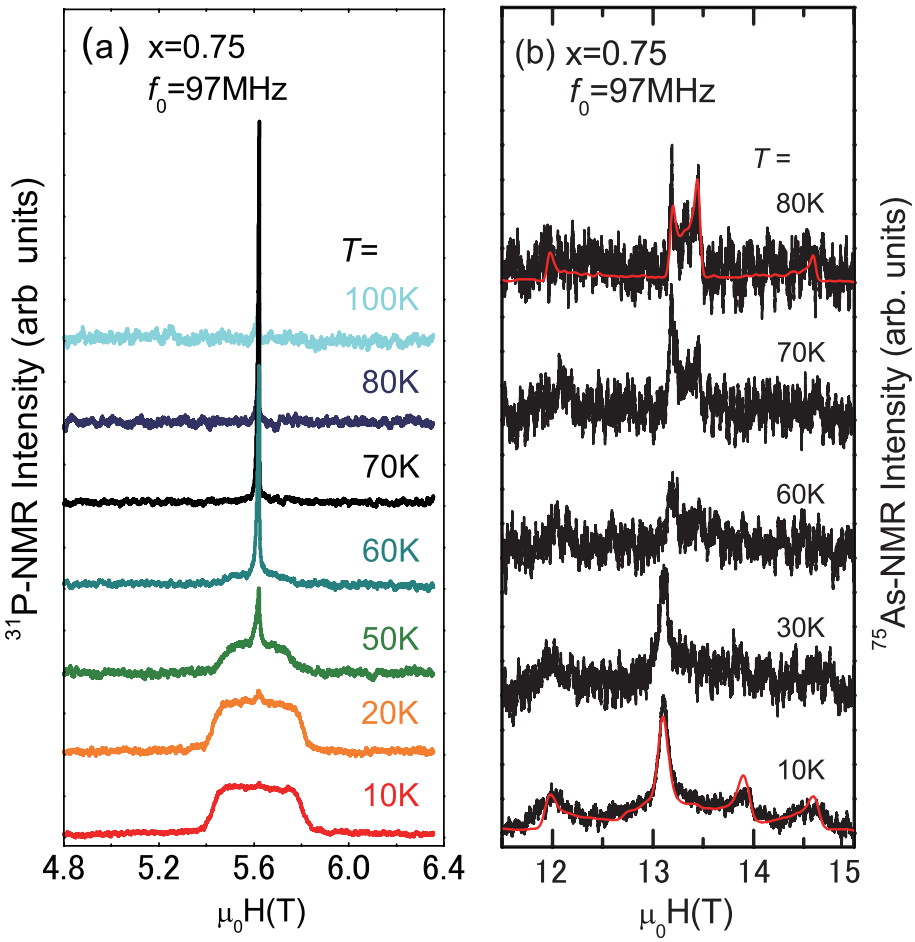

Figure 5.10: T dependence of (a) ^{31}P-NMR and (b) ^{75}As-NMR spectrum at x=0.75, pointing to the onset of AFM order below 60 K. The red solid line in (b) shows a successful simulation of the ^{75}As NMR powder-type spectrum.

In order to present a systematic evolution of the low-T phase as a function of P-substitution, the respective figures 5.11 and 5.12 indicate the x-dependences of ^{31}P-NMR spectrum and the internal fields of $^{31}H_{\rm int}$ and $^{75}H_{\rm int}$ at 10 K. The $M_{\rm AFM}$ increases from $0.16\mu_B$ at x=0.95 to $0.28\mu_B$ at x=0.5, and becomes zero at $0 \leq x \leq 0.4$ and x=1. Note that the $M_{\rm AFM}$s in these compounds were smaller than in another parent *42622* compound $[Sr_4(MgTi)O_6]Fe_2As_2$[116], but larger than in $(Sr_4Sc_2O_6)Fe_2As_2$ [117].

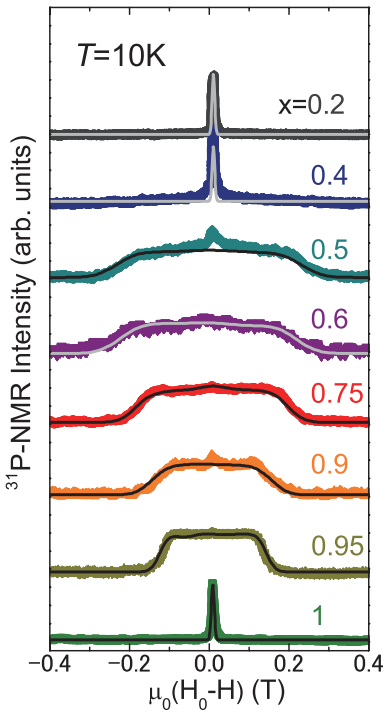

Figure 5.11: x dependence of ^{31}P-NMR spectrum at 10 K along with a simulation.

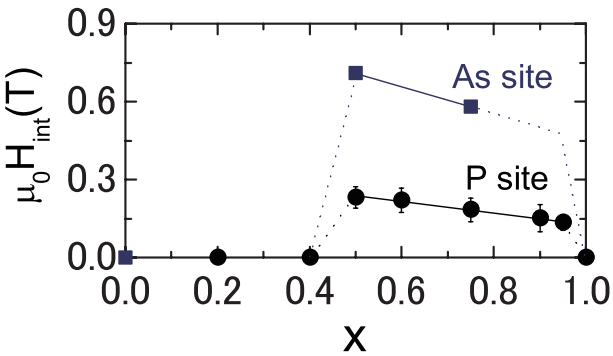

Figure 5.12: x dependence of respective internal fields $^{31}H_{\rm int}$ and $^{75}H_{\rm int}$ at ^{31}P and ^{75}As.

Figure 5.13(a) shows the T dependence of $^{31}(1/T_1T)$ of ^{31}P-NMR for $0.2 \leq x \leq 1$ along with that of $^{75}(1/T_1T)$ of ^{75}As-NQR for x=0. The nuclear spin-lattice relaxation rate $(1/T_1)$ of ^{31}P-NMR was obtained by fitting a recovery curve of ^{31}P nuclear magnetization to a single exponential function $m(t) \equiv (M_0 - M(t))/M_0 = \exp(-t/T_1)$. Here, M_0 and $M(t)$ are the respective nuclear magnetizations for a thermal equilibrium condition and at time t after a saturation pulse. In general, $1/T_1T$ is proportional to $\sum_q |A_q|^2 \chi''(\boldsymbol{q}, \omega_0)/\omega_0$, where A_q is a wave-vector ($\boldsymbol{q}$)-dependent hyperfine-coupling constant, $\chi(\boldsymbol{q}, \omega)$ a dynamical spin susceptibility, and ω_0 an NMR frequency. When a system undergoes an AFM order with a wave vector $\boldsymbol{Q}$, staggered susceptibility $\chi_Q(T)$, following a Curie-Weiss law, diverges towards T_N. As a result, the measurement of $1/T_1T$ enables the determination of a Néel temperature T_N. Actually, as shown by the solid lines in Fig. 5.13(a), the $1/T_1T$s for $0.2 \leq x \leq 1$ can be fitted by assuming $1/T_1T \sim a/(T-\theta) + b$ [92]. Remarkably, the $1/T_1T$s for $0.4 \leq x \leq 0.95$ diverge toward $T = \theta$, that is identified as T_N, because the rectangular-like NMR spectral shape points to the onset of AFM order below $T \sim \theta$, as seen in Fig. 5.10. In Fig. 5.14, the estimated T_N is plotted as the function of x.

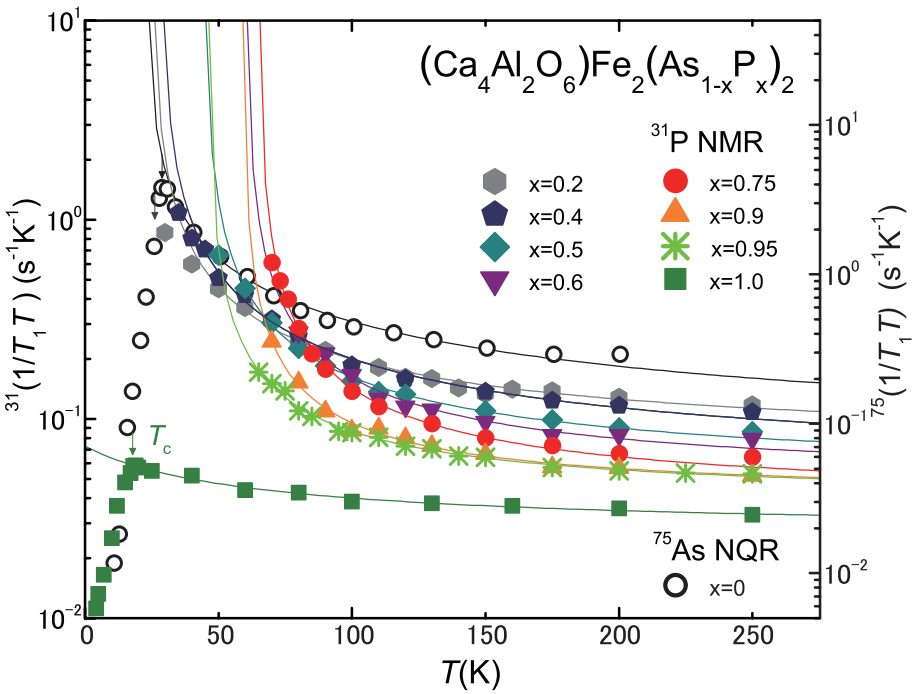

Figure 5.13: T dependence of ^{31}P-NMR $^{31}(1/T_1T)$ in $0.2 \leq x \leq 1$ along with ^{75}As-NQR $^{75}(1/T_1T)$ at x=0 at the normal state. Note that the $^{31}(1/T_1T)$s for $0.5 \leq x \leq 0.95$ diverge toward T_N, below which the ^{31}P-NMR spectrum exhibits a rectangular-like shape in association with the onset of an AFM order (see Fig. 1(b)).

The present NMR studies on CaAl42622(As,P) have revealed that as the P-substitution x increases, the nodeless SC state with T_c=27 ~ 20K in $0 \leq x \leq 0.4$ evolves into the AFM state in $0.5 \leq x \leq 0.95$, and eventually to the nodal SC state with T_c = 17K at $x = 1$ as presented in Fig. 5.14. In another context, the AFM order intervenes between the nodeless SC and the nodal SC. This phase diagram is quite outstanding among numerous Fe-pnictides reported thus far. For example, it was reported that only the nodal SC state emerges in Ba122(As,P) [125, 126, 127]. To shed light on the occurrence of AFM order in the intermediate P-substitution range of $0.5 \leq x \leq 0.95$, the AFM ordered state and the SC one for CaAl42622(As,P) are plotted in the two-dimensional plane of structural parameters of the nearest-neighbour Fe-Fe distance $a_{\mathrm{Fe-Fe}}$ and h_{Pn} by filled and empty symbols in Fig. 5.15, respectively. Here, the results are also presented on this plane with respect to 1111[20, 130, 112], 122[124, 114], 111[118, 120], and 42622-based compounds[115, 116, 117] with the Fe^{2+} state in the $(\mathrm{Fe}Pn)^-$ layer through the isovalent substitution at pnictogen sites. As a result, it is demonstrated that the AFM order in the $(\mathrm{Fe}Pn)^-$ layer takes place universally irrespective of materials when h_{Pn} is in the range of 1.32Å$\leq h_{Pn} \leq$ 1.42Å. It is noteworthy that when $h_{Pn} >$ 1.42Å, the nodeless SC emerges in Fe(Se,Te) [73, 131] and LiFeAs[123, 109] with the Fe^{2+} state in the $(\mathrm{Fe}Pn)^-$ layer as well as the case for CaAl42622(As,P) with $0 \leq x \leq 0.4$. On the other hand, when $h_{Pn} <$ 1.32Å, the nodal SC takes place for *Ae*122(As,P) (*Ae*=Ba,Sr)[124, 125, 126, 127, 128], LiFeP[109], LaFePO[108, 107], and $(Sr_4Sc_2O_6)Fe_2P_2$[110]. In this context, the quite unique and important ingredient found in CaAl42622(As,P) is that the nodeless SC and the nodal SC are separated by the onset of AFM order. According to this empirical rule, it is reasonably understood that in the parent *111* compounds without any chemical doping, LiFeAs, and LiFeP [123, 109] exhibit the nodeless and nodal SC, respectively, whereas NaFeAs exhibits the AFM order [118, 120]. The novel two-dimensional map of the AFM ordered phase and the SC phase of Fig. 5.15 is universal irrespective of a material's details, pointing to the importance of correlation effect for the emergence of SC as well as AFM order

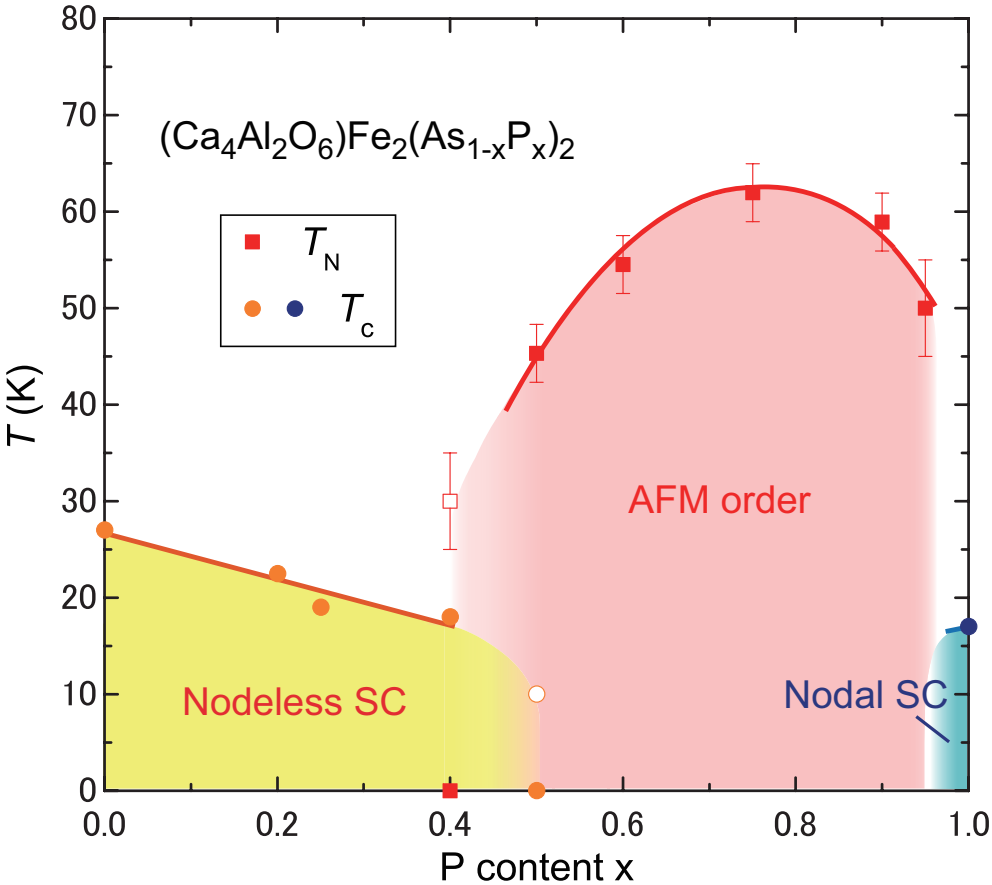

Figure 5.14: (a) Phase diagram against x in $(Ca_4Al_2O_6)Fe_2(As_{1-x}P_x)_2$. The commensurate AFM order occurs in $0.5 \leq x \leq 0.95$, which intervenes between the nodeless SC in $0 \leq x \leq 0.4$ and the nodal SC at x=1. Each empty symbol near the phase boundary between the nodeless SC phase and the AFM ordered phase means that each sample contains a tiny fraction of minority domain exhibiting either AFM order or nodeless SC due to a possible spatial distribution of As/P content.

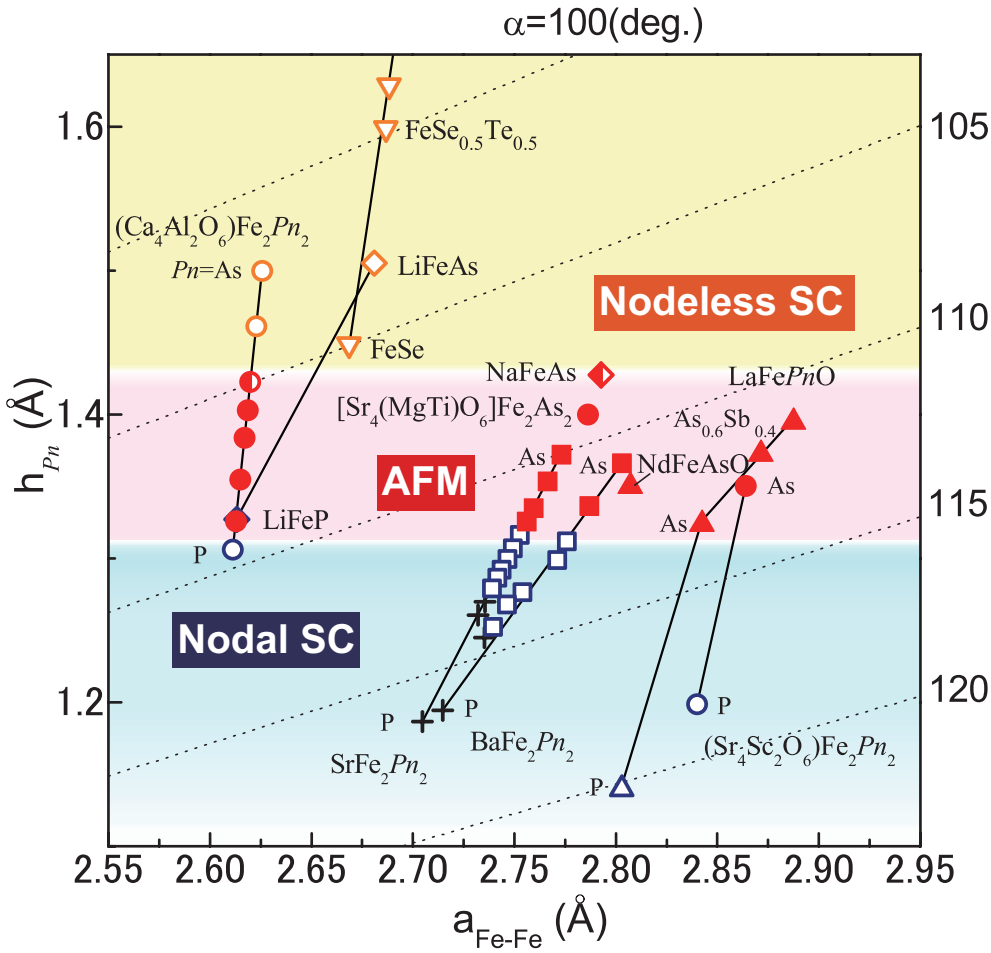

Figure 5.15: Map of the AFM ordered phase (filled symbols) and the SC phase (empty symbols) for $(Ca_4Al_2O_6)Fe_2(As_{1-x}P_x)_2$ plotted in the two-dimensional plane of structural parameters of the Fe-Fe distance $a_{\mathrm{Fe-Fe}}$ and h_{Pn}. Here, the emergent phases for various Fe-based compounds with the Fe^{2+} state in $(FePn)^-$ layer through the isovalent substitution at pnictogen (Pn) sites are presented with respect to Fe(Se,Te)[73, 131], LiFe(As,P)[123, 109], $BaFe_2(As,P)_2$[124, 114, 125, 126, 127], LaFe(Sb,As,P)O[20, 130, 108, 107], NdFeAsO[112], and $(Sr_4M_2O_6)Fe_2(As,P)_2$ (M=$Mg_{0.5}Ti_{0.5}$[115, 116], Sc[117, 110]). The symbol (+) denotes the compounds which are not superconductive. The AFM order taking place universally in the range of 1.32 Å$\leq h_{Pn} \leq$ 1.42Å intervenes between the nodeless SC in $h_{Pn} >$ 1.42Å and the nodal SC in $h_{Pn} <$ 1.32Å. Dotted line is a linear relation of h_{Pn} versus $a_{\mathrm{Fe-Fe}}$ at each value of α.

Finally, the present results on CaAl42622(As,P) are considered in terms of a systematic evolution of Fermi-surface (FS) topology as the function of h_{Pn} according to the band calculations based on the five-orbital model reported previously [93, 94, 63, 132]. In general, the Fe-pnictides have similar FSs composed of disconnected two-dimensional hole pockets around Γ(0,0) and Γ′(π,π), and electron pockets around M[(0,π) and (π,0)] points. For the case of x=0 with a very large h_{Pn}=1.5 Å due to a narrow As-Fe-As bond angle $\alpha \sim$ 102°, a hole FS around Γ′ is quite visible at the Fermi level, whereas one of the two-hole FSs at Γ is missing [93], and hence the FS nesting condition is much better than in others [93, 94]. By contrast, for the case of x=1 with a very small h_{Pn}=1.31 Å due to $\alpha \sim$ 109.5°, the two-hole FSs at Γ and one hole FS at Γ′ appear as well as in Ln1111 with T_c >50 K [63, 132]. Although the FS multiplicity for x=1 is larger than that for x=0, the nesting condition of FSs in x=1 is worse than in x=0, bringing about the reduction in the Stoner factor for AFM correlations more significantly [94] as confirmed from the result in Fig. 5.9 (b). In the intermediate region of x, the band calculation suggests the slight development of χ_Q and the reduction of eigenvalue in Eliashberg equation for $s_{\pm}$-wave pairing around x ~0.7 [132, 133]. As for the nodal SC at x=1, although its h_{Pn} is comparable to those of Ae122(As,P)(Ae=Ba,Sr) [124, 128], the origin of the nodal SC may differ from that in 122 compounds because of a highly two-dimensional electronic structure in the (FePn)$^-$ layer separated by a thick perovskite-type block for CaAl42622(P).

Chapter 6

Summary

To conclude this thesis, we remark the extensive NQR and NMR studies on the new series of iron-pnictide superconductors $Ca_4Al_2O_6Fe_2(As_{1-x}P_x)_2$ with the pervskite-type thick block layer, focusing on the normal and superconducting state properties.

1. Antiferromagnetic Spin Fluctuations and Unconventional Nodeless Superconductivity in $(Ca_4Al_2O_6)Fe_2As_2$

The ^{75}As-NQR studies on $(Ca_4Al_2O_{6-y})(Fe_2As_2)$ with T_c = 27 K have unraveled the development of two-dimensional AFM spin fluctuations and pointed to the unconventional nodeless superconductivity; The dominant interband scattering due to the nesting of hole and electron FSs is responsible for the marked enhancement of 2D AFM spin fluctuations and the sign-nonconserving interband scattering is responsible for the T^7-like reduction behavior in $1/T_1$ without the coherence peak below T_c. The T evolution in $1/T_1$ in the SC state was consistently accounted for by the $s_{\pm}$-wave multiple gaps model. The present result also suggests that the DOS with the small SC gap is totally reduced in association with the disappearance of some part of Fermi surfaces. From the fact that T_c = 27 K in this compound is comparable to T_c = 28 K in the optimally-doped $LaFeAsO_{1-y}$ in which AFM spin fluctuations are not dominant, we remark that AFM spin fluctuations are not a unique factor for enhancing T_c, but a condition for optimizing SC should be addressed from the lattice structure point of view.

2. Nodal Gap Superconductivity in $(Ca_4Al_2O_6)Fe_2P_2$

$(Ca_4Al_2O_6)Fe_2P_2$ exhibits T-linear dependence of $1/T_1$ well below T_c, implying the superconductivity realized with nodal gap. This nodal superconductivity is in contrast with the nodeless superconductivity at the arsenide counterparts $(Ca_4Al_2O_6)Fe_2As_2$. Furthermore, our ^{31}P -NMR experiments on $(Ca_4Al_2O_6)Fe_2P_2$ is first successful in indicating the formation of unconventional superconductivity in the context of AFM spin fluctuations among all FeP-based

superconductors, which include LaFePO and LiFeP, behind the above important result. This fact allows us to treat FeP-based compounds as with FeAs-based ones.

3. Phase Diagtram of $Ca_4Al_2O_6Fe_2(As_{1-x}P_x)_2$

The ^{31}P and ^{75}As-NMR studies on $(Ca_4Al_2O_6)Fe_2(As_{1-x}P_x)_2$ have revealed the novel phase diagram including the nodeless SC ($0 \leq x \leq 0.4$) and the nodal SC (x=1) intimately separated by the onset of commensurate AFM order ($0.5 \leq x \leq 0.95$). It is highlighted that as a result of the fact that the P-substitution for As decreases the pnictogen height from the Fe plane, the AFM order taking place in the range of 1.32 Å$\leq h_{Pn} \leq$ 1.42 Å intervenes between the nodeless SC and the nodal SC and this event is universal irrespective of materials with the Fe^{2+} state in the $(FePn)^-$ layer. In this context, the $s_{\pm}$-wave SC scenario mediated by spin fluctuations is quite promising when noting that this model has consistently accounted for our systematic experiments on series of compounds such as 42622, 1111, 122, and others reported thus far.

The multiorbital nature of the iron-based superconductors makes it difficult to understand the mechanism which leads to superconducty, but I believe that our findings bring a breakthrough.

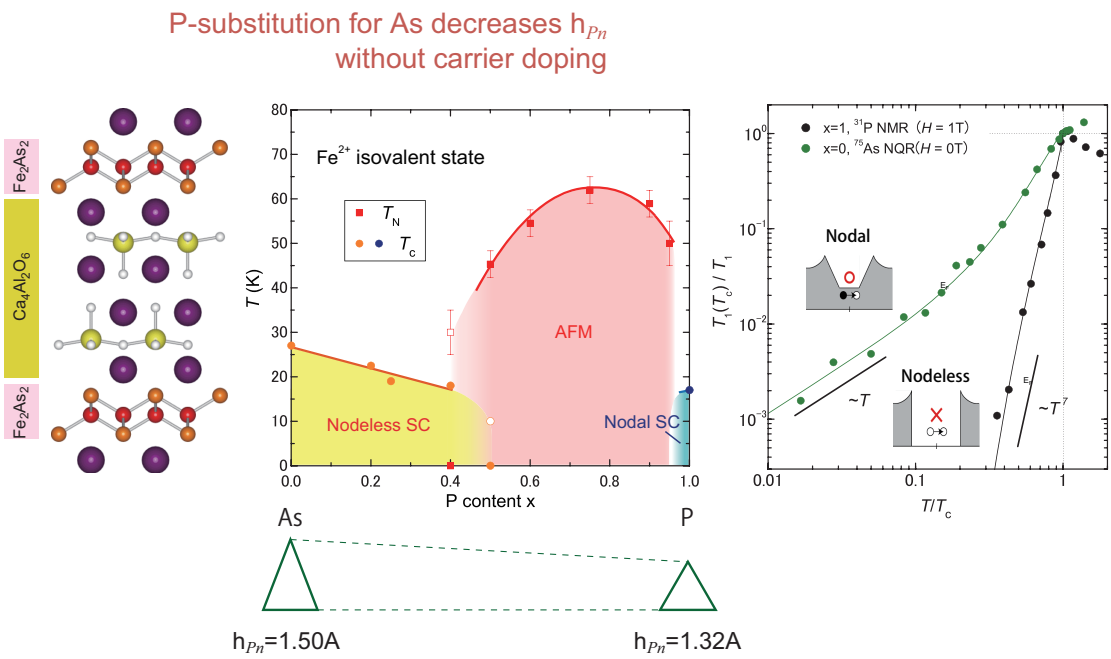

Figure 6.1: Summary of NMR / NQR studies on an isovalent system $(Ca_4Al_2O_6)$ $Fe_2(As_{1-x}P_x)_2$.

Bibliography

[1] H. Kammerlingh Onnes, Akad. V. Wetenschappen (Amsterdam) **14**, 113 (1911).

[2] J. Bardeen, L. N. Cooper, and J. R. Schrieffer, Phys. Rev. **108** 1175 (1957).

[3] A. A. Abrikosov, and L. P. Gor'kov, Sov. Phys. JETP **12**, 1243 (1961).

[4] J. G. Bednorz, and K.A. Müller, Z. Phys. B **64**, 189 (1986).

[5] C. W. Chu, Phys. Rev. Lett. **58**, 908 (1987).

[6] A. Schilling, M. Cantoni, J.D. Guo, and H.R. Ott, Nature (London) **363**, 56 (1993).

[7] M. Nunez-Regueiro, J.-L. Tholence, E.V. Antipov, J.-J. Capponi, and M. Marezio, Science **262**, 97 (1993); Nao Takeshita, Ayako Yamamoto, Akira Iyo, and Hiroshi Eisaki, J. Phys. Soc. Jpn. **82**, 023711 (2013).

[8] Mona Berciu's webpage at http://www.phas.ubc.ca/ berciu/RESEARCH/.

[9] Hidenori Takagi, Nature Mater. **6**, 179 (2007).

[10] Y. Kamihara, H. Hiramatsu, M. Hirabo, R. Kawamura, H. Yanagi, T. Kamiya, and H. Hosono, J. Am. Chem. Soc. **128** 10012-10013 (2006).

[11] Y. Kamihara, T. Watanabe, M. Hirano, and H. Hosono, J. Am. Chem. Soc. **130** 3296-3297 (2008).

[12] H. Takahashi, K. Igawa, K. Arii, Y. Kamihara, M. Hirano, and H. Hosono, Nature (London) **453**, 376-378 (2008).

[13] Z.-A. Ren, W. Lu, J. Yang, W. Yi, X.-L. Shen, Z.-C. Li, G.-C. Che, X.-L. Dong, L.-L. Sun, F. Zhou, and Z.-X. Zhao, Chin. Phys. Lett. **25**, 2215 (2008).

[14] C. Wang, L. Li, S. Chi, Z. Zhu, Z. Ren, Y. Li, Y. Wang, X. Lin, Y. Luo, S. Jiang, X. Xu, G. Cao, and Z. Xu, Europhys. Lett. **83**, 67006 (2008).

[15] H. Kinouchi, H. Mukuda, M. Yashima, Y. Kitaoka, P. M. Shirage, H. Eisaki, and A. Iyo, Phys. Rev. Lett. **107**, 047002 (2011).

[16] H. Kinouchi, H. Mukuda, Y. Kitaoka, P. M. Shirage, H. Fujihisa, Y. Gotoh, H. Eisaki, and A. Iyo, Phys. Rev. B **87**, 121101(R) (2013).

[17] Parasharam M. Shirage, Kunihiro Kihou, Chul-Ho Lee, Hijiri Kito, Hiroshi Eisaki, and Akira Iyo, Appl. Phys. Lett. **97**, 172506 (2010).

[18] Parasharam M. Shirage, Kunihiro Kihou, Chul-Ho Lee, Nao Takeshita, Hiroshi Eisaki, and Akira Iyo, J. Am. Chem. Soc. **134**, 15181 (2012).

[19] Fa Wang, and Dung-Hai Lee, Science **332**, 200 (2011).

[20] Clarina de la Cruz, Q. Huang, J. W. Lynn, Jiying Li, W. Ratcliff II, J. L. Zarestky, H. A. Mook, G. F. Chen, J. L. Luo, N. L. Wang, and Pengcheng Dai, Nature (London) **453**, 899-902 (2008).

[21] A. Jesche, C. Krellner, M. de Souza, M. Lang, and C. Geibel, Phys. Rev. B **81**, 134525 (2010).

[22] Yongkang Luo, Qian Tao, Yuke Li, Xiao Lin, Linjun Li, Guanghan Cao, Zhu-an Xu, Yun Xue, Hiroshi Kaneko, Andrey V. Savinkov, Haruhiko Suzuki, Chen Fang, and Jiangping Hu, Phys. Rev. B **80**, 224511 (2009).

[23] H. Luetkens, H.-H. Klauss, M. Kraken, F. J. Litterst, T. Dellmann, R. Klingeler, C. Hess, R. Khasanov, A. Amato, C. Baines, M. Kosmala, O. J. Schumann, M. Braden, J. Hamann-Borrero, N. Leps, A. Kondrat, G. Behr, J. Werner, and B. Büchner, Nature Mat. **8**, 305 (2009).

[24] Jun Zhao, Q. Huang, Clarina de la Cruz, Shiliang Li, J. W. Lynn, Y. Chen, M. A. Green, G. F. Chen, G. Li, Z. Li, J. L. Luo, N. L. Wang, and Pengcheng Dai, Nature Mat. **7**, 953 (2008).

[25] Stephen D. Wilson, Z. Yamani, C. R. Rotundu, B. Freelon, E. Bourret-Courchesne, and R. J. Birgeneau, Phys. Rev. B **79**, 184519 (2009).

[26] A. Jesche, N. Caroca-Canales, H. Rosner, H. Borrmann, A. Ormeci, D. Kasinathan, H. H. Klauss, H. Luetkens, R. Khasanov, A. Amato, A. Hoser, K. Kaneko, C. Krellner, and C. Geibel, Phys. Rev. B **78**, 180504 (R) (2008).

[27] C. Lester, Jiun-Haw Chu, J. G. Analytis, S. C. Capelli, A. S. Erickson, C. L. Condron, M. F. Toney, I. R. Fisher, and S. M. Hayden, Phys. Rev. B **79**, 144523 (2009).

[28] S. Avci, O. Chmaissem, E. A. Goremychkin, S. Rosenkranz, J.-P. Castellan, D. Y. Chung, I. S. Todorov, J. A. Schlueter, H. Claus, M. G. Kanatzidis, A. Daoud-Aladine, D. Khalyavin, and R. Osborn, Phys. Rev. B **83**, 172503 (2011).

[29] K. Hashimoto, K. Cho, T. Shibauchi, S. Kasahara, Y. Mizukami, R. Katsumate, Y. Tsuruhara, T. Terashima, H. Ikeda, M. A. Tanatar, H. Kitano, N. Salovich, R. W. Giannetta, P. Walmsley, A. Carrington, R. Prozorov, and Y. Matsuda, Science **336**, 1554 (2012).

[30] Dinah R. Parker, Matthew J. P. Smith, Tom Lancaster, Andrew J. Steele, Isabel Franke, Peter J. Baker, Francis L. Pratt, Michael J. Pitcher, Stephen J. Blundell, and Simon J. Clarke, Phys. Rev. Lett. **104**, 057007 (2010).

[31] Michael J. Pitcher, Dinah R. Parker, Paul Adamson, Sebastian J. C. Herkelrath, Andrew T. Boothroyd, Richard M. Ibberson, Michela Brunelli, and Simon J. Clarke, Chem. Commun. (Cambridge), 5918 (2008).

[32] Joshua H. Tapp, Zhongjia Tang, Bing Lv, Kalyan Sasmal, Bernd Lorenz, Paul C. W. Chu, and Arnold M. Guloy, Phys. Rev. B **78**, 060505 (R) (2008).

[33] Z. Deng, X. C. Wang, Q. Q. Liu, S. J. Zhang, Y. X. Lv, J. L. Zhu, R. C. Yu, and C. Q. Jin, Europhys. Lett. **87**, 37004 (2009).

[34] K. Mydeen, E. Lengyel, Z. Deng, X. C. Wang, C. Q. Jin, And M. Nicklas, Phys. Rev. B **82**, 014514 (2010).

[35] Shiliang Li, Clarina de la Cruz, Q. Huang, Y. Chen, J. W. Lynn, Jiangping Hu, Yi-Lin Huang, Fong-Chi Hsu, Kuo-Wei Yeh, Maw-Kuen Wu, and Pengcheng Dai, Phys. Rev. B **79**, 054503 (2009).

[36] Wei Bao, Y. Qiu, Q. Huang, M. A. Green, P. Zajdel, M. R. Fitzsimmons, M. Zhernenkov, S. Chang, Minghu Fang, B. Qian, E. K. Vehstedt, Jinhu Yang, H. M. Pham, L. Spinu, and Z. Q. Mao, Phys. Rev. Lett. **102**, 247001 (2009).

[37] S. Margadonna, Y. Takabayashi, M. T. McDonald, K. Kasperkiewicz, Y. Mizuguchi, Y. Takano, A. N. Fitch, E. Suarde, and K. Prassides, Chem. Commun. (Cambridge), 5607 (2008).

[38] Fong-Chi Hsu, Jiu-Yong Luo, Kuo-Wei Yeh, Ta-Kun Chen, Tzu-Wen Huang, Phillip M. Wu, Yong-Chi Lee, Yi-Lin Huang, Yan-Yi Chu, Der-Chung Yan, and Maw-Kuen Wu, Proc. Natl. Acad. Sci. U.S.A. **105**, 14262 (2008).

[39] Yoshikazu Mizuguchi, Fumiaki Tomioka, Shunsuke Tsuda, Takahide Yamaguchi, and Yoshihiko Takano, Appl. Phys. Lett. **93**, 152505 (2008).

[40] T. J. Liu, J. Hu, B. Qian, D. Fobes, Z. Q. Mao, W. Bao, M. Reehuis, S. A. J. Kimber, K. Prokeš, S. Matas, D. N. Argyriou, A. Hiess, A. Rotaru, H. Pham, L. Spinu, Y. Qiu, V. Thampy, A. T. Savici, J. A. Rodriguez, and C. Broholm, Nature Mat. **9**, 718 (2010).

[41] J. Dong, Europhys. Lett. **83**, 27006 (2008).

[42] T. Yildirim, Phys. Rev. Lett. **101**, 057010 (2008).

[43] Q. M. Si, and E. Abrahams, Phys. Rev. Lett. **101**, 076401 (2008).

[44] H.-J. Grafe, D. Paar, G. Lang, N. J. Curro, G. Behr, J. Werner, J. Hamann-Borrero, C. Hess, N. Leps, R. Klingeler, and B. Büchner, Phys. Rev. Lett. **101**, 047003 (2008).

[45] K. Matano, Z. A. Ren, X. L. Dong, L. L. Sun, Z. X. Zhao, and Guo-qing Zheng, Europhys. Lett. **83**, 57001 (2008).

[46] Fanlong Ning, Kanagasingham Ahilan, Takashi Imai, Athena S. Sefat, Ronying Jin, Michael A. McGuire, Brian C. Sales, and David Mandrus, J. Phys. Soc. Jpn. **77**, 103705 (2008).

[47] Mitsuharu Yashima, Hideaki Nishimura, Hidekazu Mukuda, Yoshio Kitaoka, Kiichi Miyazawa, Parasharam M. Shirage, Kunihiro Kihou, Hijiri Kito, Hiroshi Eisaki, and Akira Iyo, J. Phys. Soc. Jpn. **78**, 103702 (2008).

[48] P. Jeglič, A. Potočnik, M. Klanjšek, M. Bobnar, M. Jagodič, K. Koch, H. Rosner, S. Margadonna, B. Lv, A. M. Guloy, and D. Arčon, Phys. Rev. B **81**, 140511(R) (2010).

[49] Yasuhiro Shimizu, Takato Yamada, Tsuyoshi Takami, Seiji Niitaka, Hidenori Takagi, and Masayuki Itoh, J. Phys. Soc. Jpn. **78**, 123709 (2009).

[50] K. Hashimoto, T. Shibauchi, T. Kato, K. Ikada, R. Okazaki, H. Shishido, M. Ishikado, H. Kito, A. Iyo, H. Eisaki, S. Shamoto, and Y. Matsuda, Phys. Rev. Lett. **102**, 017002 (2009).

[51] K. Hashimoto, T. Shibauchi, S. Kasahara, K. Ikada, S. Tonegawa, T. Kato, R. Okazaki, C. J. van der Beek, M. Konczykowski, H. Takeya, K. Hirata, T. Terashima, and Y. Matsuda, Phys. Rev. Lett. **102**, 207001 (2009).

[52] H. Ding, P. Richard, K. Nakayama, K. Sugawara, T. Arakane, Y. Sekiba, A. Takayama, S. Souma, T. Sato, T. Takahashi, Z. Wang, X. Dai, Z. Fang, G. F. Chen, J. L. Luo, and N. L. Wang, Europhys. Lett. **83**, 47001 (2008).

[53] Lin Zhao, Hai-Yun Liu, Wen-Tao Zhang, Jian-Qiao Meng, Xiao-Wen Jia, Guo-Dong Liu, Xiao-Li Dong, Gen-Fu Chen, Jian-Lin Luo, Nan-Lin Wang, Wei Lu, Gui-Ling Wang, Yong Zhou, Yong Zhu, Xiao-Yang Wang, Zu-Yan Xu, Chuang-Tian Chen, and Xing-Jiang Zhou, Chin. Phys. Lett. **25**, 4402 (2008).

[54] L. Wray, D. Qian, D. Hsieh, Y. Xia, L. Li, J. G. Checkelsky, A. Pasupathy, K. K. Gomes, C. V. Parker, A. V. Fedorov, G. F. Chen, J. L. Luo, A. Yazdani, N. P. Ong, N. L. Wang, and M. Z. Hasan, Phys. Rev. B **78**, 184508 (2008).

[55] K. Nakayama, T. Sato, P. Richard, Y.-M. Xu, Y. Sekiba, S. Souma, G. F. Chen, J. L. Luo, N. L. Wang, H. Ding, and T. Takahashi, Europhys. Lett. **85**, 67002 (2009).

[56] K. Terashima, Y. Sekiba, J. H. Bowen, K. Nakayama, T. Kawahara, T. Sato, P. Richard, Y.-M. Xu, L. J. Li, G. H. Cao, Z.-A. Xu, H. Ding, and T. Takahashi, Proc. Natl. Acad. Sci. U.S.A. **106**, 7330 (2009).

[57] K. Umezawa, Y. Li, H. Miao, K. Nakayama, Z.-H. Liu, P. Richard, T. Sato, J. B. He, D.-M. Wang, G. F. Chen, H. Ding, T. Takahashi, and S.-C. Wang, Phys. Rev. Lett. **108**, 037002 (2012).

[58] Z.-H. Liu, P. Richard, K. Nakayama, G.-F. Chen, S. Dong, J.-B. He, D.-M. Wang, T.-L. Xia, K. Umezawa, T. Kawahara, S. Souma, T. Sato, T. Takahashi, T. Qian, Yaobo Huang, Nan Xu, Yingbo Shi, H. Ding, and S.-C. Wang, Phys. Rev. B **84**, 064519 (2011).

[59] K. Nakayama, T. Sato, P. Richard, T. Kawahara, Y. Sekiba, T. Qian, G. F. Chen, J. L. Luo, N. L. Wang, H. Ding, and T. Takahashi, Phys. Rev. Lett. **105**, 197001 (2010).

[60] H. Miao, P. Richard, Y. Tanaka, K. Nakayama, T. Qian, K. Umezawa, T. Sato, Y.-M. Xu, Y. B. Shi, N. Xu, X.-P. Wang, P. Zhang, H.-B. Yang, Z.-J. Xu, J. S. Wen, G.-D. Gu, X. Dai, J.-P. Hu, T. Takahashi, and H. Ding, Phys. Rev. B **85**, 094506 (2012).

[61] I. I. Mazin, M. D. Johannes, L. Boeri, K. Koepernik, and D. J. Singh, Phys. Rev. B **78**, 085104 (2008).

[62] Hiroki Nakamura, and Masahiko Machida, J. Phys. Soc. Jpn. **79**, 013705 (2010).

[63] K. Kuroki, H. Usui, S. Onari, R. Arita, and H. Aoki, Phys. Rev. B **79**, 224511 (2009).

[64] F. L. Ning, K. Ahilan, T. Imai, A. S. Sefat, M. A. McGuire, B. C. Sales, D. Mandrus, P. Cheng, B. Shen, and H.-H. Wen, Phys. Rev. Lett. **104**, 037001 (2010).

[65] Y. Nakai, T. Iye, S. Kitagawa, K. Ishida, H. Ikeda, S. Kasahara, H. Shishido, T. Shibauchi, Y. Matsuda, and T. Terashima, Phys. Rev. Lett. **105**, 107003 (2010).

[66] Y. Nakai, T. Iye, S. Kitagawa, K. Ishida, S. Kasahara, T. Shibauchi, Y. Matsuda, H. Ikeda, and T. Terashima, Phys. Rev. B **87**, 174507 (2013).

[67] C.-H. Lee, A. Iyo, H. Eisaki, H. Kito, M. T. Fernandez-Diaz, T. Ito, K. Kihou, H. Matsuhata, M. Braden, and K. Yamada, J. Phys. Soc. Jpn. **77**, 083704 (2008).

[68] J. Zhao, Q. Huang, C. de la Cruz, S. Li, J. W. Lynn, Y. Chen, M. A. Green, G. F. Chen, G. Li, Z. Li, J. L. Luo, N. L. Wang, and P. Dai, Nature Mater. **7**, 953 (2008).

[69] Y. Mizuguchi, Y. Hara, K. Deguchi, S. Tsuda, T. Yamaguchi, K. Takeda, H. Kotegawa, H. Tou, and Y. Takano, Supercond. Sci. Technol. **23**, 054013(2010).

[70] I. I. Mazin, D. J. Singh, M. D. Johannes, and M. H. Du, Phys. Rev. Lett. **101**, 057003 (2008).

[71] K. Kuroki, S. Onari, R. Arita, H. Usui, Y. Tanaka, H. Kontani, and H. Aoki, Phys. Rev. Lett. **101**, 087004 (2008).

[72] Kangjun Seo, B. Andrei Bernevig, and Jiangping Hu, Phys. Rev. Lett. **101**, 206404 (2008).

[73] T. Hanaguri, S. Niitaka, K. Kuroki, and H. Takagi, Science **328**, 474 (2010).

[74] A. D. Christianson, E. A. Goremychkin, R. Osborn, S. Rosenkranz, M. D. Lumsden, C. D. Malliakas, I. S. Todorov, H. Claus, D. Y. Chung, M. G. Kanatzidis, R. I. Bewley, and T. Guidi, Nature (London) **456**, 930 (2008).

[75] D. Parker, O. V. Dolgov, M. M. Korshunov, A. A. Golubov, and I. I. Mazin, Phys. Rev. B **78**, 134524 (2008).

[76] A. V. Chubukov, D. V. Efremov, and I. Eremin, Phys. Rev. B **78**, 134512 (2008).

[77] Yunkyu Bang, and Han-Yong Choi, Phys. Rev. B **78**, 134523 (2008).

[78] Hiroshi Kontani, and Seiichiro Onari, Phys. Rev. Lett. **104**, 157001 (2010).

[79] Ming Yi, Donghui Lu, Jiun-Haw Chu, James G. Analytis, Adam P. Sorini, Alexander F. Kemper, Brian Moritz, Sung-Kwan Mo, Rob G. Moore, Makoto Hashimoto, Wei-Sheng Lee, Zahid Hussain, Thomas P. Devereaux, Ian R. Fisher, and Zhi-Xun Shen, Proc. Natl. Acad. Sci. U.S.A. **108**, 6878 (2011).

[80] Terutaka Goto, Ryosuke Kurihara, Koji Araki, Keisuke Mitsumoto, Mitsuhiro Akatsu, Yuichi Nemoto, Shunichi Tatematsu, and Masatoshi Sato, J. Phys. Soc. Jpn. **80**, 073702 (2011).

[81] T. Shimojima, F. Sakaguchi, K. Ishizaka, Y. Ishida, T. Kiss, M. Okawa, T. Togashi, C.-T. Chen, S. Watanabe, M. Arita, K. Shimada, H. Namatame, M. Taniguchi, K. Ohgushi, S. Kasahara, T. Terashima, T. Shibauchi, Y. Matsuda, A. Chainani, and S. Shin, Science **332**, 564 (2011)

[82] A. Carrington and F. Manzano: Physica C **385**, 205 (2003).

[83] R. Prozorov and R.W. Giannetta: Supercond. Sci. Technol. **19**, 41(R) (2006).

[84] L. C. Hebel and C. P. Slichter: Phys. Rev. **113**, 1504 (1958).

[85] S. J. Clark, M. D. Segall, C. J. Pickard, P. J. Hasnip, M. I. J. Probert, K. Refson, and M. C. Payne, Z. Kristallogr. 220, 567 (2005).

[86] H. Ogino, Y. Katsura, S. Horii, K. Kishio, and J. Shimoyama, Supercond. Sci. Technol. **22**, 085001 (2009).

[87] H. Ogino Y. Shimizu, K. Ushiyama, N. Kawaguchi, K. Kishio, and J. Shimoyama, Appl. Phys. Express. **3** 063103 (2010).

[88] X. Zhu F. Han, G. Mu, P. Cheng, B. Shen, B. Zeng, and H.-H. Wen, Phys. Rev. B **79**, 220512(R) (2009).

[89] H. Kotegawa, T. Kawazoe, H. Tou, K. Murata, H. Ogino, K. Kishio, and J. Shimoyama, J. Phys. Soc. Jpn. **78**, 123707 (2009).

[90] H. Mukuda, N. Terasaki, H. Kinouchi, M. Yashima, Y. Kitaoka, S. Suzuki, S. Miyasaka, S. Tajima, K. Miyazawa, Parasharam Shirage, H. Kito, H. Eisaki, and A. Iyo, J. Phys. Soc. Jpn. **77**, 093704 (2008).

[91] H. Mukuda, N. Terasaki, M. Yashima, H. Nishimura, Y. Kitaoka, A. Iyo, Physica C **469**, 559 (2009).

[92] T. Moriya and K. Ueda, Adv. Phys. **49**, 555 (2000).

[93] T. Miyake, T. Kosugi, S. Ishibashi, and K. Terakura, J. Phys. Soc. Jpn. **79**, 123713 (2010).

[94] H. Usui and K. Kuroki, Phys. Rev. B, **84**, 024505 (2011).

[95] Y. Nakai, K. Ishida, Y. Kamihara, M. Hirano, and H. Hosono, J. Phys. Soc. Jpn. **77**, 073701 (2008).

[96] H. Yamashita, H. Mukuda, M. Yashima, S. Furukawa, Y. Kitaoka, K. Miyazawa, Parasharam M. Shirage, H. Eisaki, and A. Iyo, J. Phys. Soc. Jpn. **79**, 103703 (2010).

[97] D. Parker, O. V. Dolgov, M. M. Korshunov, A. A. Golubov, and I. I. Mazin, Phys. Rev. B **78**, 134524 (2008).

[98] A. V. Chubukov, D. V. Efremov, and I. Eremin, Phys. Rev. B **78**, 134512 (2008).

[99] Y. Bang and H. Y. Choi, Phys. Rev. B **78**, 134523 (2008).

[100] M. M. Parish, J. Hu, and B. A. Bernevig, Phys. Rev. B **78**, 144514 (2008).

[101] Y. Nagai, N. Hayashi, N. Nakai, H. Nakamura, M. Okumura, and M. Machida, New J. Phys. **10**, 103026 (2008).

[102] H. Mukuda, M. Nitta, M. Yashima, Y. Kitaoka, Parasharam M. Shirage, H. Eisaki, and A. Iyo, J. Phys. Soc. Jpn. **79**, 113701 (2010).

[103] S. Ohsugi, Y. Kitaoka, M. Kyogaku, K. Ishida, K. Asayama and T. Ohtani, J. Phys. Soc. Jpn. **61**, 3054 (1992).

[104] H. Kotegawa, K. Ishida, Y. Kitaoka, T. Muranaka, N. Nakagawa, H. Takagiwa, and J. Akimitsu, Phys. Rev. B **66**, 064516 (2002).

[105] Y. F. Guo, Y. G. Shi, S. Yu, A. A. Belik, Y. Matsushita, M. Tanaka, Y. Katsuya, K. Kobayashi, I. Nowik, I. Felner, V. P. S. Awana, K. Yamaura, and E. Takayama-Muromachi, Phys. Rev. B **82**, 054506 (2010).

[106] S. Kitagawa, Y. Nakai, T. Iye, K. Ishida, Y. F. Guo, Y. G. Shi, K. Yamaura, and E. Takayama-Muromachi, Phys. Rev. B **83**, 180501 (R) (2011).

[107] C. W. Hicks, T. M. Lippman, M. E. Huber, J. G. Analytis, J. -H. Chu, A. S. Erickson, I. R. Fisher, and K. A. Moler, Phys. Rev. Lett. **103**, 127003 (2009).

[108] J. D. Fletcher, A. Serafin, L. Malone, J. G. Analytis, J.-H. Chu, A. S. Erickson, I. R. Fisher, and A. Carrington, Phys. Rev. Lett. **102**, 147001 (2009).

[109] K. Hashimoto, S. Kasahara, R. Katsumata, Y. Mizukami, M. Yamashita, H. Ikeda, T. Terashima, A. Carrington, Y. Matsuda, and T. Shibauchi, Phys. Rev. Lett. **108**, 047003 (2012).

[110] K. A. Yates, I. T. M. Usman, K. Morrison, J. D. Moore, A. M. Gilbertson, A. D. Caplin, L. F. Cohen, H. Ogino, and J. Shimoyama, Supercond. Sci. Technol. **23**, 022001 (2010).

[111] Y. Nakai, K. Ishida, Y. Kamihara, M. Hirano, and H. Hosono, Phys. Rev. Lett. **101**, 077006 (2008).

[112] Y. Qiu, W. Bao, Q. Huang, T. Yildirim, J. M. Simmons, M. A. Green, J. W. Lynn, Y. C. Gasparovic, J. Li, T. Wu, G. Wu, and X. H. Chen, Phys. Rev. Lett. **101**, 257002 (2008).

[113] M. Rotter, M. Tegel, D. Johrendt, I. Schellenberg, W. Hermes, and R. Pöttgen, Phys. Rev. B **78**, 020503(R) (2008).

[114] Q. Huang,Y. Qiu, W. Bao, M. A. Green, J. W. Lynn, Y. C. Gasparovic, T. Wu, G. Wu, and X. H. Chen, Phys. Rev. Lett **101**, 257003 (2008).

[115] S. Sato, H. Ogino, N. Kawaguchi, Y. Katsura, K. Kishio, J. Shimoyama, H. Kotegawa, and H. Tou, Supercond. Sci. Technol. **23**, 045001 (2010).

[116] K. Yamamoto, H. Mukuda, H. Kinouchi, M. Yashima, Y. Kitaoka, M. Yogi, S. Sato, H. Ogino, and J. Shimoyama, J. Phys. Soc. Jpn. **81**, 053702 (2012).

[117] J. Munevar, D. R. Sánchez, M. Alzamora, E. Baggio-Saitovitch, J. P. Carlo, T. Goko, A. A. Aczel, T. J. Williams, G. M. Luke, H. -H. Wen, X. Zhu, F. Han, and Y. J. Uemura, Phys. Rev. B **84**, 024527 (2011).

[118] G. F. Chen, W. Z. Hu, J. L. Luo, and N. L. Wang, Phys. Rev. Lett. **102**, 227004 (2009).

[119] L. Ma, G. F. Chen, D.-X. Yao, J. Zhang, S. Zhang, T. -L. Xia, and W. Yu, Phys. Rev. B **83**, 132501(R) (2011).

[120] K. Kitagawa, Y. Mezaki, K. Matsubayashi, Y. Uwatoko, and M. Takigawa, J. Phys. Soc. Jpn. **80**, 033705 (2011).

[121] X. C. Wang, Q. Q. Liu, Y. X. Lv, W. B. Gao, L. X. Yang, R. C. Yu, F. Y. Li, and C. Q. Jin, Solid State Commun. **148**, 538 (2008).

[122] J. H. Tapp, Z. Tang, B. Lv, K. Sasmal, B. Lorenz, P. C. W. Chu, and A. M. Guloy, Phys. Rev. B **78**, 060505(R) (2008).

[123] H. Kim, M. A. Tanatar, Y. J. Song, Y. S. Kwon, and R. Prozorov, Phys. Rev. B **83**, 100502 (2011).

[124] S. Kasahara, T. Shibauchi, K. Hashimoto, K. Ikada, S. Tonegawa, R. Okazaki, H. Shishido, H. Ikeda, H. Takeya, K. Hirata, T. Terashima, and Y. Matsuda, Phys. Rev. B **81**, 184519 (2010).

[125] Y. Nakai, T. Iye, S. Kitagawa, K. Ishida, S. Kasahara, T. Shibauchi, Y. Matsuda, and T. Terashima, Phys. Rev. B **81**, 020503(R) (2010).

[126] M. Yamashita, Y. Senshu, T. Shibauchi, S. Kasahara, K. Hashimoto, D. Watanabe, H. Ikeda, T. Terashima, I. Vekhter, A. B. Vorontsov, and Y. Matsuda, Phys. Rev. B **84**, 060507 (2011).

[127] Y. Zhang, Z. R. Ye, Q. Q. Ge, F. Chen, J. Jiang, M. Xu, B. P. Xie, and D. L. Feng, Nat. Phys. **8**, 371 (2012).

[128] T. Dulguun, H. Mukuda, T. Kobayashi, F. Engetsu, H. Kinouchi, M. Yashima, Y. Kitaoka, S. Miyasaka, and S. Tajima, Phys. Rev. B **85**, 144515 (2012).

[129] K. Kitagawa, N. Katayama, K. Ohgushi, M. Yoshida, and M. Takigawa, J. Phys. Soc. Jpn. **77**, 114709 (2008).

[130] S. J. E. Carlsson, F. Levy-Bertrand, C. Marcenat, A. Sulpice, J. Marcus, S. Pairis, T. Klein, M. Núñez-Regueiro, G. Garbarino, T. Hansen, V. Nassif, and P. Toulemonde, Phys. Rev. B **84**, 104523 (2011).

[131] H. Kotegawa, S. Masaki, Y. Awai, H. Tou, Y. Mizuguchi, and Y. Takano, J. Phys. Soc. Jpn. **77**, 113703 (2008).

[132] T. Kosugi, T. Miyake, S. Ishibashi, and K. Terakura, J. Phys. Soc. Jpn. **81**, 014701 (2012).

[133] Hidetomo Usui, Katsuhiro Suzuki, Kazuhiro Kuroki, Nao Takeshita, Parasharam Maruti Shirage, Hiroshi Eisaki, and Akira Iyo, Phys. Rev. B **87**, 174528 (2013).

List of Publications

○ Articles in Refereed Journals

1. H. Kinouchi, H. Mukuda, M. Yashima, Y. Kitaoka, P. M. Shirage, H. Eisaki, and A. Iyo, "Antiferromagnetic Spin Fluctuations and Unconventional Nodeless Superconductivity in an Iron-Based New Superconductor $(Ca_4Al_2O_{6-y})(Fe_2As_2)$: ^{75}As Nuclear Quadrupole Study", Physical Review Letters **107**, 047002 (2011).
   (Highlighted in NPG Asia Materials: "Iron-based superconductors: Critical relationships", doi:10.1038/asiamat.2011.155)

2. K. Yamamoto, H. Mukuda, H. Kinouchi, M. Yashima, Y. Kitaoka, M. Yogi, S. Sato, H. Ogino, and J. Shimoyama,"Antiferromagnetic Order and Superconductivity in $Sr_4(Mg_{0.5-x}Ti_{0.5+x})_2O_6Fe_2As_2$ with Electron Doping: ^{75}As-NMR Study", Journal of the Physical Society of Japan **81**, 053702 (2012).

3. T. Dulguun, H. Mukuda, T. Kobayashi, F. Engetsu, H. Kinouchi, M. Ya shima, Y. Kitaoka, S. Miyasaka, and S. Tajima, "Unconventional multiband superconductivity with nodes in single-crystalline $SrFe_2(As_{0.65}P_{0.35})_2$ as seen via ^{31}P NMR and specific heat", Physical Review B **85**, 144515 (2012).

4. H. Mukuda, S. Furukawa, H. Kinouchi, M. Yashima, Y. Kitaoka, P. M. Shirage, H. Eisaki, and A. Iyo, "High-Tc Nodeless $s_{\pm}$-wave Superconductivity in (Y,La)$FeAsO_{1-y}$ with T_c=50K: ^{75}As-NMR Study", Physical Review Letters **109**, 157001 (2012).

5. H. Kinouchi, H. Mukuda, Y. Kitaoka, P. M. Shirage, H. Fujihisa, Y. Gotoh, H. Eisaki, and A. Iyo, "Emergent phases of nodeless and nodal superconductivity separated by antiferromagnetic order in iron-based superconductor $(Ca_4Al_2O_6)Fe_2(As_{1-x}P_x)_2$: ^{75}As- and ^{31}P-NMR studies", Physical Review B **87**, 121101 (R) (2013).

○ Conference Presentations

1. H. Kinouchi, H. Mukuda, M. Yashima, Y. Kitaoka, P-M. Shirage, H. Eisaki and A. Iyo, "Antiferromagnetic spin fluctuations and $s_{\pm}$-wave Superconductivity $(Ca_4Al_2O_{6-y})(Fe_2As_2)$ probed by As NQR", 26th International Conference on Low Temperature Physics (LT26), 16P-B086, Beijing, China, August 2011.

2. 木内宏彰, 椋田秀和, 八島光晴, 北岡良雄, P. M. Shirage, 永崎洋, 伊豫彰, "$(Ca_4Al_2O_{6-y})(Fe_2Pn_2)$ [Pn =As and P] の NMR/NQR ", 日本物理学会 2011 年秋季大会, 21aGM-12, 富山大学, 富山, 2011 年 9 月.

3. H. Kinouchi, H. Mukuda, K. Kitaoka, P. M. Shirage, H. Fujihisa, Y. Gotoh, H. Eisaki, and A. Iyo, "Contrasting Superconducting Property in Fe-based superconductors $(Ca_4Al_2O_{6-y})(Fe_2Pn_2)$[$Pn$ =As and P] ", The 19th International Conference on Magnetism with Strongly Correlated Electron System (ICM2012), AF1328, Busan, Korea, July 2012.

4. H. Kinouchi, H. Mukuda, M. Yashima, K. Kitaoka, P. M. Shirage, H. Fujihisa, Y. Gotoh, H. Eisaki, and A. Iyo, "Contrasting Superconducting Property in Fe-based superconductors $(Ca_4Al_2O_{6-y})(Fe_2Pn_2)$ [Pn =As and P] ", The International Conference on Materials and Mechanisms of Superconductivity (M2S 2012), P2-67, Washington D. C., USA, July 2012.

5. 木内宏彰, 椋田秀和, 北岡良雄, P. M. Shirage, 永崎洋, 伊豫彰, "^{31}P-NMR による等価数置換系 $(Ca_4Al_2O_6)Fe_2(As_{1-x}P_x)_2$ の電子相図 ", 日本物理学会 2012 年秋季大会, 21aGA-12, 横浜国立大学, 神奈川, 2012 年 9 月.

6. 木内宏彰, 椋田秀和, 北岡良雄, P. M. Shirage, 永崎洋, 伊豫彰, "^{31}P-NMR による等価数置換系 $(Ca_4Al_2O_6)Fe_2(As_{1-x}P_x)_2$ の電子相図（２）", 日本物理学会第６８回年次大会, 29pXG-1, 広島大学, 広島, 2013 年 3 月.

7. 木内宏彰, 椋田秀和, 北岡良雄, P. M. Shirage, 永崎洋, 伊豫彰, "鉄系超伝導体 $(Ca_4Al_2O_6)Fe_2(As_{1-x}P_x)_2$ の NMR ", 日本物理学会 2013 年秋季大会, 27aEC-8, 徳島大学, 徳島, 2013 年 9 月.

Acknowledgments

The work described in this thesis would never have been possible without supports from a great number of people.

First I would like to thank my adviser, Prof. Yoshio Kitaoka, for his contribution to my graduate education and research. I was lucky to have the opportunity to be a part of his research group. From him I learned how to approach the problem and fun in every aspect of research. I will always appreciate his exceptional kindness and sincerity.

I would also like to thank all my collaborators in Kitaoka group. In particular, Assoc. Prof. Hidekazu Mukuda has spent a lot of time and effort to guide me, encourage me, do experiments and discuss with me. I received a lot of experimental helps from Dr. Sunao Shimizu and Dr. Mitsuharu Yashima. Ms. Takako Fukuroya assisted me in transacting my business. I am glad to have spent six years with colorful colleagues, Dr. Fumiya Kanetake, Nobuyuki Terasaki, Takashi Ohara, Shoichi Taniguchi, Tomonori Sakaguchi, Nobukatsu Tamura, Hiroki Yamashita, Keita Itohara, Hirofumi Naruwa, Tatsuya Unemori, Hideaki Nishimura, Shin-ichiro Tabata, Yuichiro Yasui, Katsuyoshi Uematsu, Shiho Iwai, Mariko Nitta, Satoshi Furukawa, Dulguun Tsendsuren, Keisuke Yamamoto, Kazuhiro Nishimoto, Takuya Kaneda, Shota Ueki, Fuko Engetsu, Yuko Tanaka, Naoki Kimoto, Kyohei Tani, Shouta Maki, Masashi Miyamoto, Ryuji Yusuke Yanai, Takayoshi Shiota, Nozomu Shiki, Naoto Kawaguchi and Takashi Matsumura. I am grateful for the friendship and support of Ayato Iyama, Takashi Honda, Shinya Okamoto and Akio Sakai.

I must also thank Dr. Parasharam M. Shirage at Indian Institute of Technology Indore, Dr. Hiroshi Fujihisa, Dr. Yoshito Gotoh, Dr. Hiroshi Eisaki and Dr. Akira Iyo at National Institute of Advanced Industrial Science and Technology, who provided me with high-quality samples and shared their wonderful experiments; Dr. Hidekazu Usui and Prof. Kazuhiko Kuroki for valuable comments and suggestions from a theoretical point of view.

I would also like to thank my thesis defense committee members, Prof. Hiroshi Miyasaka, Prof. Masaaki Ashida and Assoc. Prof. Koichi Kusakabe, for many helpful comments and insightful questions.

Finally and most importantly, I would like to express my gratitude to my family. They constantly supported me in all my pursuits, encouraged me and believed in me.